Coulomb Drag in Vertically-Integrated One-Dimensional Quantum Wires

Dominique Laroche

Department of Physics
McGill University
Montréal, Québec, Canada

December 2013

Under the supervision of Professor Guillaume Gervais and Doctor Michael Lilly

---

A thesis submitted to McGill University in partial fulfillment of the requirements for the degree of Doctor of Philosophy.

ACKNOWLEDGEMENT

First and foremost, I would like to thank my thesis advisor Guillaume Gervais for giving the opportunity to a green and brand new graduate student to go to Sandia National Laboratories in New-Mexico and tackle the challenging project of measuring Coulomb drag in vertically-coupled quantum wires. Guillaume has been constantly supportive throughout this journey, helping nurture my scientific strong suits and correcting my flaws, shaping me into the scientist I am today. “Do it once, but do it right”, one of his favorite motto, is perhaps the most important lesson he has imparted me.

I would like to express my gratitude to Mike Lilly, my co-supervisor at Sandia National Laboratories, for taking a chance with a literal stranger, for giving me the opportunity to carry out this work, for keeping faith in the long resultless months at the beginning of the project and for teaching me the basics of low-temperature lab work. Mike’s calm patience, cool head and expert advices have been instrumental to the success of this endeavor.

I could not go without mentioning Christian Morath, my lab co-worker, roommate, landlord and first New-Mexican friend. Meeting such a friendly face moving in this foreign and frankly quite intimidating new environment is one of the best things that could have happened to me. Chris’ help familiarizing myself with Sandia labs, along with his willingness to listen and help throughout my struggles and success, has been invaluable.

The intense cleanroom processing required in this project would not have been possible without the expertise of Denise Tibbets. From carrying out most of the processing at the beginning of the project to teaching me pretty much all there is to know about the cleanroom processing required for this project, Denise help has been invaluable. Likewise, the expertise in GaAs/AlGaAs growth of John Reno has been instrumental to the success of this endeavor.

I would like to extend my thanks to my other lab co-workers at Sandia National Laboratories, John Seamons, Eric Nordberg and Lisa Tracy, for their willingness to help, whether for some technical advice or simply to escort me on the week-ends to transfer liquid helium. I would also like to acknowledge the help of the technical staff of Sandia National Laboratories, most specifically John Nogan and Catherine Mombourquette in the cleanroom, Manny Gonzales and David Lang for the helium delivery and general building operation and Cory Parsons for the administrative aspect of things.

I would also like to thank the people I interacted with briefly while being at McGill; Cory Dean, Guillaume Lambert and Andrew Mack for the help in the lab and Richard Talbot for his help with the designing and the technical drawing of equipment parts. I also thank James Hedberg for his artistic sense and expertise with drawing softwares that saved me many fruitless hours when he took over some of the figure making and “beautification” for this thesis.

Finally, I would like to thank my parents and family for their support when I decided to move away to purse this thesis and for their constant encouragement and love throughout this work. I would also like to thank Erin for her love, support and understanding throughout this thesis, especially throughout the long nights and week-ends at work.

In conclusion, I acknowledge this work was performed, in part, at the Center for Integrated Nanotechnologies, a U.S. DOE, Office of Basic Energy Sciences user facility. Sandia National Laboratories is a multi-program laboratory managed and operated by Sandia Corporation, a wholly owned subsidiary of Lockheed Martin Corporation, for the U.S. Department of Energy's National Nuclear Security Administration under contract DE-AC04-94AL85000. I also acknowledge the financial support from the Natural Sciences and Engineering Research Council of Canada (NSERC), and from the FQNRT (Québec).

ABSTRACT

Understanding the physics taking place in coupled one-dimensional systems is one of the many challenges of modern day condensed matter physics and nanoelectronics. While experimental studies in coupled quantum wires have recently confirmed some of the most striking predictions of Luttinger liquid theory such as spin-charge separation and charge partitioning, much remains to be done prior a complete understanding of one-dimensional physical phenomenons is achieved, especially in the field of one-dimensional Coulomb drag.

In this thesis, I report our experimental study of one-dimensional Coulomb drag between quantum wires coupled at the nanoscale. The quantum wires are coupled in a vertical geometry, allowing the wires to be separated by a hard barrier only 15 nm wide and providing us with the possibility to study Coulomb drag in a regime never achieved previously. Our study of the 1D subband dependency of Coulomb drag shows an oscillation of the drag resistance (R_D) with 1D subband occupancy. Peaks in the drag signal are observed concomitant with the opening of 1D subbands in either wire, regardless of 1D subband alignment between the wires, and a novel high electronic density re-entrant negative regime for R_D is observed. These findings are not fully understood within the current theoretical momentum-transfer models for Coulomb drag between quantum wires. However, some of the predictions of a charge-fluctuation induced model for 1D Coulomb drag in mesoscopic circuits are consistent with our observations and raise questions as to whether mesoscopic physics play an important role in one-dimensional Coulomb drag.

The temperature dependence of the drag resistance is also presented in the one-dimensional regime where both wires have no more than a single 1D subband occupied. As the temperature is reduced below the Fermi temperature T_F, a decrease in R_D and a subsequent upturn is observed in three different devices at $T^* \simeq 1.6$ K, flagging a regime where R_D increases with decreasing T (verified down to ~ 75 mK). This upturn in the drag resistance and the diverging drag resistance at the lowest temperatures is consistent with expectations from Tomonaga-Luttinger liquid models of 1D quantum wires. It also potentially validates models including forward scattering corrections and it is a strong indication that interaction effects and momentum-transfer play an important role in one-dimensional Coulomb drag.

A crucial step for the future of electronic nano-devices is the development of doped shallow two-dimensional electron gases (2DEGs). In an effort towards this goal, we have also studied scattering mechanisms in shallow 2DEGs in parallel to our Coulomb drag experiment. In this endeavor, we achieved the fabrication of 2DEGs as shallow as 60 nm deep with a mobility in excess of 1×10^5 cm^2/ V $\cdot$ s and determined that scattering of intentional remote charged impurities is the dominant scattering mechanism in samples 130 nm deep and shallower.

ABRÉGÉ

La compréhension de la physique prenant place dans les systèmes unidimensionels couplés est un des nombreux défis auxquels la physique de la matière condensée moderne et la nano-électronique sont confrontées. En dépit du fait que certaines études portant sur des fils quantiques couplés aient confirmé certaines des prédictions les plus fascinantes de la théorie des liquides de Luttinger tels que la séparation des spins et des charges ainsi que la partition des charges, beaucoup reste à faire avant qu'une compréhension complète des phénomènes prenant naissance dans les systèmes unidimensionels ne soit atteinte, surtout en ce qui a trait à la traînée de Coulomb unidimensionnelle.

Dans cette thèse, nous rapportons l'étude expérimentale de la traînée de Coulomb unidimensionnelle entre des fils quantiques couplés à l'échelle nano-métrique. Les fils quantiques sont couplés dans une géométrie verticale permettant aux fils d'être séparés par une barrière large de seulement 15 nm, nous donnant ainsi l'occasion d'étudier la traînée de Coulomb dans un régime jamais exploré auparavant. Les résultats de notre étude de la dépendance de la traînée de Coulomb avec le niveau d'occupation des sous-bandes unidimensionnelles des fils quantiques montrent une oscillation de la résistance de la traînée de Coulomb (R_D) en fonction du nombre de sous-couches occupées dans les fils quantiques. Des maximums dans R_D sont observés simultanément à l'ouverture de sous-bandes unidimensionnelles dans l'un ou l'autre des fils et un nouveau régime de R_D négatif et résurgent est observé à haute densité. Ces observations ne sont pas complètement expliquées par les modèles actuels expliquant la traînée de Coulomb par un transfer de quantité de mouvement. Toute-

fois, certaines prédictions des modèles expliquant l'émergence de la traînée de Coulomb unidimensionnelle par un échange de fluctuations sont en accord avec nos résultats et soulèvent des doutes à savoir si la physique mésoscopique joue un role dans l'émergence de la traînée de Coulomb unidimensionnelle.

La dépendence en température de la résistance de la traînée de Coulomb est également présentée dans le régime unidimentionel où les fils ont au plus une seule sous-bande de populée. Alors que la température est abaissée sous la température de Fermi, une diminution de R_D est observée, suivie d'un renversement de cette tendence. Ce renversement est observé dans trois dispositifs distincts à une température $T^* \sim 1.6$ K et marque une transition vers un régime où R_D augmente alors que la température diminue (mesuré jusqu'à $\sim$ 75 mK). La présence de ce renversement et d'une divergence de R_D à basse température est en accord avec les prédictions de la théorie des liquides de Tomonoga-Luttinger pour des fils quantiques unidimentionels, confirment potentiellement les modèles incluant des corrections pour des faibles valeurs de transfer de quantité de mouvement et suggèrent fortement que les interactions et le transfer de quantité de mouvement sont importants dans l'émergence de la traînée de Coulomb unidimensionnelle.

Une étape cruciale pour le futur développement de nano-dispositifs électroniques est la création de puits quantiques peu profonds et dopés. Dans l'espoir d'atteindre cet objectif, nous avons étudié les mécanismes de diffusion dans des puits quantiques peu profonds en parallèle à notre étude de la traînée de Coulomb unidimensionnelle. Au cours de cet effort, nous sommes parvenus à fabriquer des puits quantiques situés seulement 60 nm sous la surface avec une mobilité supérieure à 1×10^5 cm^2/ V $\cdot$ s et nous avons déterminé que la diffusion par les impuretés ionisées volontairement insérées dans la structure est le mode de diffusion dominant dans les puits quantiques profonds de moins de 130 nm.

STATEMENT OF ORIGINALITY

The work described in this thesis represents original and genuine scholarship by the author to the field of experimental physics. The results presented in this thesis were not published elsewhere, except when otherwise specified. Here is a detailed list of the author's contributions to the thesis :

- *Apparatus* : Most of the low-temperature setup was in place prior to DL's, the author, arrival. Minor modifications to these systems where performed by DL. This setup is described in chapters 6 and 7.

- *Shallow 2DEGs experiment* : DL participated in the discussions concerning the growth details of the heterostructures used in this project. All the devices fabrication and characterization was performed by DL. Results of this work are presented in chapter 3 of this thesis, and were published as original work with DL appearing as the first author (D. Laroche, *et al.*, Appl. Phys. Lett. **96** 162112 (2010).).

- *Vertically-coupled quantum wires design and fabrication* : Preliminary aspects of the vertically-coupled double quantum wires were designed prior to DL arrival. DL contributed to the final design of the devices and fully fabricated the devices using the expertise of Mike Lilly's group in clean-room processing. Details of the design and of the fabrication process can be found in chapter 5 of this thesis and have been published as part of original work with DL appearing as the first author. (D. Laroche, *et al.*, Physica **E** 40 1569 (2008). and D. Laroche, *et al.*, Nature Nanotechnol. **6**, 793 (2011).)

- *Coulomb drag experiments* : DL performed all the low-temperature Coulomb drag measurements and their analysis. These results are presented in chapter 6 and 7 of this thesis. Significant contribution to the field of one-dimensional Coulomb drag from this work include :

    - First measurement of one-dimensional Coulomb drag between wires separated by less than 15 nm.
    - Discovery of negative one-dimensional Coulomb drag occurring at high electronic density in the wires.
    - Characterization of the temperature dependence of one-dimensional Coulomb drag, mostly in the true one-dimensional regime.

  Results concerning the negative Coulomb drag were published as original work with DL appearing as the first author (D. Laroche, *et al.*, Nature Nanotechnol. **6**, 793 (2011).). Another article describing the temperature dependence of the one-dimensional Coulomb drag signal with DL appearing as the first author is pending review.

Contents

List of Tables

List of Figures

List of Abbreviations and Symbols

Table 1: List of abbreviations and symbols

Symbol	Definition
1, 2 and 3D	One-, two- and three-dimensions (dimensional)
2DEG	Two-Dimensional Electron Gas
AC / DC	Alternative Current / Direct Current
BOE	Buffered Oxide Etch
CEO	Cleaved-Edge Overgrowth
CINT	Center for Integrated Nanotechnologies
CVD	Chemical Vapor Deposition
DUT	Device Under Test
DVM	Digital Volt-Meter
EBASE	Epoxy-Bond-and-Stop-Etch
E-beam	Electron-Beam
FQHE	Fractional Quantum Hall Effect

HF	Hydrofluoric Acid
IPA	Iso-Propyl Alcohol
IV	Current-Voltage as in an IV curve
LED	Light-Emitting Diode
LI	Lock-In as in Lock-In amplifier
LL (or TLL)	Luttinger Liquid (or Tomonaga-Luttinger Liquid)
LO	Longitudinal Optical as in Longitudinal optical phonons
LPL	Lower Plunger as in lower plunger gate
LPO	Lower Pinch-Off as in lower pinch-off gate
MBE	Molecular Beam Epitaxy
MIBK	Methyl Iso-Buthyl Ketone
MOSFET	Metal-Oxide-Semiconductor Field Electron Transistor
NPGS	Nanometer Pattern Generation Systems
PMMA	Poly-Methyl Methacrylate
QHE	Quantum Hall Effect
RPM	Rotations per Minute
SdH	Shubnikov de-Hass as in Shubnikov de-Hass oscillations
SEM	Scanning Electron Microscope
UPL	Upper Plunger as in upper plunger gate
UPO	Upper Pinch-Off as in upper pinch-off gate
$a(T)$	Undefined polynomial function
a_B, a_B^*	Bohr radius
A	Area
A_i	Imaginary part of the retarded density correlation function

$b(T)$	Undefined polynomial function
b_k	Annihilation operator for a boson with wave vector k
$b_k^\dagger$	Creation operator for a boson with wave vector k
B	Magnetic field
B_ν	Magnetic field value at an even filling fraction
c_i	Constant
c_k	Annihilation operator for a fermion with wave vector k
$c_k^\dagger$	Creation operator for a fermion with wave vector k
C_v	Specific heat
d	Interlayer (or interwire) separation
d_i	Dopants separation to the closest 2DEG
D	System dimensions
e	Electron's charge
$\boldsymbol{E}$	Electric field
E_f	Fermi energy
E_s	Soliton energy
f	Frequency
f_F	Fermi-Dirac distribution
$\mathbf{F}$	Force
$g(\mathbf{k})$	Semi-classical electron distribution function
G	Conductance
h	Planck's constant ($2\pi \times \hbar$)
$\hbar$	Planck's constant
H	Hamiltonian

H_b	Backscattering Hamiltonian
H_ρ	Hamiltonian for the charge sector
H_σ	Hamiltonian for the spin sector
H_+	Symmetric Hamiltonian
H_-	Anti-symmetric Hamiltonian
I_{CD}	Current flowing from contacts C to D
I_D	Drag current
I_{drive}	Drive current
I_J	Fluctuation current
$I_{R\to L}$	Current from right to left
J	Spin-exchange energy
$\mathbf{k}$	Wave-vector
k_B	Boltzmann's constant
k_F	Fermi wave-vector
K	Luttinger liquid interaction parameter
$K_0(x)$	Modified Bessel function of order 0
K_ρ	Luttinger liquid charge interaction parameter
K_ρ^-	Relative Luttinger liquid charge interaction parameter
K_σ	Luttinger liquid spin interaction parameter
l_0	Forward scattering length
l_{2k_F}	Backscattering length
L	Wire's length
L^*	Critical length
m	Mass

m^*	Effective mass
n	Charge density
n_c	Critical density for percolation transition to occur
n_e	Electron density
n_h	Hole density
n_δ	Dopants concentration
n_{1D}	1D density
n_{2D}	2D density
N	Subband occupancy of a quantum wire
N_{drag}	Number of 1D subband occupied in the drag wire
N_{drive}	Number of 1D subband occupied in the drive wire
N_i	Impurity per unit of volume
N_R, N_L	Bosons number operators
p	Momentum
p_0	Initial momentum
q	Wave vector difference
q_{TF}	Thomas-Fermi screening length
Q	Translational wave vector or measure of the density imbalence
r	Position
$r_\perp$	Perpendicular separation
R	Resistance
$R_{AB,CD}$	Four-point resistance using $V_{A,B}$ and I_{CD}
R_D	Drag Resistance
R_{Hall}	Hall resistance

R_s	Sense resistance
R_{tunnel}	Tunneling resistance
R_{xx}	Longitudinal resistance
t	Time
T	Temperature
$T_{crossover}$	Crossover temperature
T_F	Fermi temperature
T_0	Energy scale where the the density is comparable to the interwire separation
T_1	Measure of the density imbalance between the quantum wires
T^*	Crossover or upturn temperature
T_λ, T_N	Transmission probability across the λ^{th} or the N^{th} channel
u	Luttinger liquid velocity or relative strength of the voltage with respect to the length
u_ρ	Luttinger liquid charge velocity
u_σ	Luttinger liquid spin velocity
u^β	2D Fourier transformation of the screened scattering potential
$U_{1,2}$	Interwire interaction potential
U_ρ^-	Interwire charge interaction potential
v	Velocity
$\boldsymbol{v_d}$	Drift velocity
v_e	Electron velocity
v_F	Fermi velocity
v_h	Hole velocity

V	Voltage
$V_{A,B}$	Voltage difference between contacts B and A
V_{drag}	Drag voltage
V_{drive}	Drive voltage
V_{Hall}	Hall voltage
V_{Tunnel}	Tunneling voltage
V_{xx}	Longitudinal voltage
W	Chemical potential difference
$W_{k,k'}$	Scattering probability per unit of time
$Y(r,q)$	Step function
$Z_{i,j}$	Elements of the trans-impedance matrix
α	Power-law exponent relating the mobility to the density
α_{2k_F}	Power-law exponent of the temperature dependence
α_{4k_F}	Power-law exponent of the temperature dependence
α^+	Interaction kernel
β	Arbitrary cut-off
$\delta(x-y)$	Delta-function
δV	Voltage noise
$\delta V_{Johnson}$	Johnson (or thermal) noise
Δ	Gradiant or difference between two quantities
$\epsilon(\boldsymbol{k})$	Energy distribution function
ϵ_+	Energy of electrons
ϵ_-	Energy of holes
Γ_1	Rectification coefficient

κ	Dielectric constant
λ	Transverse quantum number
$\lambda(T)$	Temperature dependent coupling constant
λ_0	Constant coupling constant
$\bar{\lambda}(T)$	Temperature dependent coupling constant
Λ	Collision integral
μ	Mobility or chemical potential
ω_c	Cyclotron frequency
ω_L	Frequency of the collective plasmonic excitations
$\phi(x), \theta(x)$	Bosonic fields
$\phi^+_\rho, \theta^+_\rho$	Symmetric bosonic fields for the charge sector
$\phi^+_\sigma, \theta^+_\sigma$	Symmetric bosonic fields for the spin sector
$\phi^-_\rho, \theta^-_\rho$	Anti-symmetric bosonic fields for the charge sector
$\phi^-_\sigma, \theta^-_\sigma$	Anti-symmetric bosonic fields for the spin sector
ϕ_N	Wavefunction of the N^{th} 1D subband
Φ_J	Fluctuation voltage
$\Pi(x)$	Conjugate field to $\phi(x)$
ρ	Resistivity
ρ_0	Resistivity's constant
$\rho^\dagger(q)$	Density fluctuation creation operator for fluctuations with momentum q
ρ_{drag}	Drag resistivity
ρ_{xx}	Longitudinal resistivity
σ	Conductivity

τ	Transport relaxation time
θ	Relative strength of the temperature with respect to length
$\theta_{\boldsymbol{k},\boldsymbol{k}'}$	Angle between wave vectors $\boldsymbol{k}$ and $\boldsymbol{k}'$
χ	Susceptibility of an electron gas
ζ	Riemann-zeta function

1

Introduction and Context

1.1 Context

Understanding the collective behavior of closely packed and interacting matter is one of the main goals of condensed matter physics. While it is relatively straightforward to determine the behavior of a small number of particles using the well known laws of physics, the exceedingly large number of atoms and electrons contained in a typical liquid or solid is beyond the computing ability of even the strongest computer. It is therefore impossible by any practical means to exactly calculate in a brute force way the behavior of large systems by considering the motion and interactions of every individual particles.

Instead, collective models have been brought forth to explain and understand the properties of large systems with much success, effectively circumventing the brute-force method. For example, the thermal conductivity, electrical conductivity and heat capacity of metals were first understood in terms of the Drude-Sommerfeld model, superconductivity can be explained by the BCS theory, many properties of two-dimensional systems are well understood within the Fermi-liquid framework and exotic properties of the fractional quantum Hall effect are mostly understood in terms of the composite fermion model.

In addition to the obvious interest in understanding nature at a fundamental level, condensed matter physics has also led to many technological breakthroughs. One only has to think about the Silicon MOSFETs used to fabricate modern day computers, the high-electron-mobility transistors used in cellular phones, as well as the semiconductor and solid-state lasers used in a great variety of industrial and medical applications.

The subject of this thesis, that is measuring and understanding the Coulomb drag effect between two one-dimensional quantum wires, is a textbook example of modern day research in condensed matter physics where a model system is built and then its data are compared with predictions from theory. However, with the ever increasing miniaturization of the transistor to increase the power of modern day computers, studying one-dimensional electronic systems coupled at the nano-scale might become more than a strictly academic study since it might become crucial in the future development of modern computers.

Despite the conceptual simplicity of one-dimensional system, understanding the physics taking place in these systems is no small feat since, as the dimensionality of a system is reduced to such an extreme, the restricted phase-space induces stronger particle-particle correlations and interactions, rendering the simpler models describing high-dimensional systems inadequate to describe one-dimensional ones. From an experimental standpoint, creating systems small enough to be truly one-dimensional and having the experimental capabilities to measure the small signals created by such systems have been a challenge for a long time. Indeed, while theoretical work on one-dimensional systems has been performed since the 1950's, it was not until the 1980's that the first true one dimensional quantum systems, systems where the confinement in the transverse direction is strong enough to quantize their energy levels, were created by Kouwenhoven's [1] and Pepper's group [2]. These one-dimensional systems were low-temperature quantum point contacts fabricated from a AlGaAs/GaAs heterostructure. Part of the confinement required to realize such devices was already achieved by the specific arrangement of the crystalline heterostructure used as a substrate for the quantum point contacts, effectively confining the electrons in the vertical direction in what is called a two-dimensional electron gas, or 2DEG. Using metal gates deposited on the surface of the heterostructure separated by $\sim$ 250 nm and negatively biased, the two-dimensional electrons were then further confined using a clever geometrical arrangement, effectively creating a one-dimensional channel. Since then, one-dimensional systems have been realized in numerous systems, such as organic superconductors [3], carbon nanotubes [4, 5], nanowires [6, 7], edge states in the quantum Hall regime [8, 9], Josephson junctions array [10], cold gas traps [11] and graphene nanoribbons [12].

While the transport properties of these single one-dimensional systems are relatively well understood, they do not offer much insight into the intrinsic properties of interacting electrons in one-dimensional systems. Indeed, the low-temperature and low-frequency transport measurements usually performed in single 1D systems probe physical processes taking place solely in the higher dimensionality Fermi liquid leads [13, 14], or processes that have been washed out by the physics taking place in the leads [15]. Nevertheless, the properties of strongly interacting one-dimensional electrons can be measured in low-frequency transport measurements given that the measurement is *only* sensitive to processes taking place inside one-dimensional systems, and not in the leads. This is possible in *coupled* 1D systems where experiments such as 1D tunneling and 1D Coulomb drag effectively probe the section of the device where only one-dimensional electronic systems are interacting. Since quantum point contacts and quantum wires can be fabricated in extremely pure crystalline GaAs/AlGaAs heterostructures and are defined inside a 2DEG buried inside the heterostructure, effectively shielding them from most surface effects, coupled quantum wires are the system of choice to study the interactions between one-dimensional electrons with a minimal amount of external interference.

Experiments such as 1D-1D tunneling [16, 17] and Coulomb drag between laterally coupled quantum wires [18] have confirmed some of the predictions of the Luttinger liquid theory, such as a spin-charge separation, and have deepened our understanding of one-dimensional systems. However, recent observation of an unpredicted low-density negative one-dimensional Coulomb drag signal [19] shows that our understanding of one-dimensional systems, and especially of Coulomb drag between one-dimensional systems, is far from complete.

In the following thesis, I describe our efforts in fabricating vertically-coupled quantum wires designed for measuring one-dimensional Coulomb drag between quantum wires. The vertical coupling of the quantum wires allows us to measure Coulomb drag in a new regime, not achievable in laterally-coupled quantum wires, where the wires are truly coupled at the nanoscale, being separated by only a 15 nm wide barrier. Achieving such a small interwire separation should also ease the measurement of Coulomb drag as the strength of the drag signal is expected to decrease exponentially with increasing interwire separation within standard momentum-transfer theories for Coulomb drag. In addition to these Coulomb drag measurements, I present our effort in developing and characterizing doped shallow 2DEGs, which might prove crucial to the future development of patterned nanostructures by enabling the fabrication of smaller and more sharply defined structures.

The 1D subband occupancy and the temperature dependence of Coulomb drag have yielded surprising results. First, we have discovered a novel high-density negative Coulomb drag signal at a specific 1D subband occupancy in the wires, in addition to the already reported low-density negative Coulomb drag signal. Also, the drag signal is maximal for wires with different 1D subband occupancies. Both these observations appear to go against the most common theoretical models describing 1D Coulomb drag and clearly shows that our current understanding of 1D Coulomb drag is far from complete. The temperature dependence of 1D Coulomb drag also shows a rich non-monotonic behavior that is heavily dependent on the 1D subband occupancy of both wires and hints at the fact that more than a single physical mechanism appears to play a role in one-dimensional Coulomb drag.

1.2 Outline of the Thesis

I first begin this thesis with an introduction to two-dimensional electronic systems formed in semiconductors. Here, I briefly review the two-dimensional GaAs/AlGaAs quantum well and the dominant scattering mechanisms taking place in such two-dimensional systems. Then, after a brief description of the Fermi liquid model, the main theoretical model describing the physics taking place in 2DEGs, a review of the main experimental results achieved in coupled 2D systems is presented, with an emphasis on 2D-2D tunneling and Coulomb drag. In addition to providing the necessary theoretical background to our study of scattering mechanisms in shallow 2DEGs, this chapter outlines many important experimental techniques that form the basis of our work on one-dimensional Coulomb drag.

In Chapter 3, I present our study of the various scattering mechanisms taking place in doped shallow 2DEGs. After a brief description of the molecular-beam epitaxy (MBE) growth process used to fabricate these heterostructures, the main results of this study are presented, along with the experimental technique used to obtain them. During this experiment, we achieved the fabrication of doped shallow 2DEGs that have a 4 K mobility in excess of 1×10^5 cm^2/ V $\cdot$ s while being located only 60 nm from the surface. In addition, we determined the dominant scattering mechanism in samples 130 nm deep and shallower to be scattering off intentional remote impurities.

Chapter 4 marks the beginning of the one-dimensional section of this thesis where the theoretical background and the historical development of 1D physics is presented. The Luttinger liquid model, the model believed to describe the physics taking place in one-dimensional systems, is first presented. Then, a description of the main theoretical models brought forth to describe and explain one-dimensional Coulomb drag are presented, with a clear distinction between Coulomb drag arising from momentum-transfer and Coulomb drag arising from energy exchange through fluctuations. This chapter concludes with a brief experimental review of the main achievements realized in single and coupled quantum wires, with an emphasis on 1D Coulomb drag between wires coupled in a lateral geometry and the shortcomings of this design.

The remainder of this thesis (chapters 5, 6 and 7) describes our efforts in fabricating vertically-coupled quantum wires and measuring Coulomb drag between them. Chapter 5 outlines the fabrication process and design used to fabricate the vertically-coupled quantum wires. In Chapter 6, the basic characterization of the quantum wires is presented, along with the study of the 1D subband dependence of Coulomb drag where a novel high density negative Coulomb drag regime is observed. These results contrast with previous experimental findings observed in laterally coupled quantum wires and are not readily explained by current Coulomb drag theories based on momentum-transfer models in single channel quantum wires. Possible explanations with alternative theories describing the Coulomb drag as emerging from energy fluctuations of electron and holes in mesoscopic circuits are considered. I also present in chapter 7 our current efforts in measuring the temperature dependence of 1D Coulomb drag. In the true 1D regime where a single 1D subband is occupied in both quantum wires, an upturn in the temperature dependence of the Coulomb drag signal is observed, in qualitative agreement with Luttinger liquid models and potentially validating models including forward scattering corrections to 1D Coulomb drag. This observation is a strong sign that interaction effects and momentum-transfer play an important role in one-dimensional Coulomb drag. In the final chapter of this thesis, I conclude by summarizing our main findings and by highlighting the new avenues of research that this work will open.

References

[1] van Wees, B. J., van Houten, H., Beenakker, C. W. J., Williamson, J. G., Kouwenhoven, L. P., van der Marel, D., and Foxon, C. T. *Phys. Rev. Lett.* **60**, 848 (1988).

[2] Wharam, D. A., Thornton, T. J., Newbury, R., Pepper, M., Ahmed, H., Frost, J. E. F., Hasko, D. G., Peacock, D. C., Ritchie, D. A., and Jones, G. A. C. *J. Phys. C: Solid State Phys.* **21**, L209 (1988).

[3] Jérôme, D., Mazaud, A., Ribault, M., and Bechgaard, K. *J. Physique Lett.* **41**, L–95 (1980).

[4] Iijima, S. *Nature* **354**, 56 (1991).

[5] Tans, S. J., Devoret, M. H., Dai, H., Thess, A., Smalley, R. E., Geerligs, L. J., and Dekker, C. *Nature* **386**, 474 (1997).

[6] Heath, J. R. and LeGoues, F. K. *Chem. Phys. Lett.* **208**, 263 (1993).

[7] Huber, C. A., Huber, T. E., Sadoqi, M., Lubin, J. A., Manalis, S., and Prater, C. B. *Science* **263**, 800 (1994).

[8] Milliken, F. P., Umbach, C. P., and Webb, R. A. *Solid. State. Comm.* **97**, 309 (1995).

[9] Chang, A. M., Pfeiffer, L. N., and West, K. W. *Phys. Rev. Lett.* **77**, 2538 (1996).

[10] Anderson, B. P. and Kasevich, M. A. *Science* **282**, 1686 (1998).

[11] Greiner, M., Bloch, I., Mandel, O., Hänsch, T. W., and Esslinger, T. *Phys. Rev. Lett.* **87**, 160405 (2001).

[12] Lin, Y. M., Perebeinos, V., Chen, Z., and Avouris, P. *Phys. Rev. B* **78**, 161409 (2008).

[13] Maslov, D. L. and Stone, M. *Phys. Rev. B* **52**, 5539 (1995).

[14] Ponomarenko, V. V. *Phys. Rev. B* **52**, 8666 (1995).

[15] Steinberg, H., Barak, G., Yacoby, A., Pfeiffer, L. N., West, K. W., Halperin, B. I., and Le Hur, K. *Nature Physics* **4**, 116 (2008).

[16] Tserkovnyak, Y., Halperin, B. I., Auslaender, O. M., and Yacoby, A. *Phys. Rev. B* **68**, 125312 (2003).

[17] Auslaender, O. M., Steinberg, H., Yacoby, A., Tserkovnyak, Y., Halperin, B. I., Baldwin, K. W., Pfeiffer, L. N., and West, K. W. *Science* **308**, 88 (2005).

[18] Debray, P., Zverev, V., Raichev, O., Klesse, R., Vasilopoulos, P., and Newrock, R. S. *J. Phys.: Condens. Matter* **13**, 3389 (2001).

[19] Yamamoto, M., Stopa, M., Tokura, Y., Hirayama, Y., and Tarucha, S. *Science* **313**, 204 (2006).

2

Review of Quantum Transport and Coulomb Drag in Two-Dimensional Systems

In the following chapter, I present a review of the theoretical framework to two-dimensional quantum transport, along with a selection of some of the key experimental discoveries realized in this sub-field of condensed matter physics. The overarching goal of this chapter is to provide a broad overview of the main aspects of low dimensional quantum transport and, more specifically, to provide an understanding of the origin, the historical context and the current state of affairs for two-dimensional Coulomb drag. Towards this goal, I first present an overview regarding the development of the material science and the growth of semiconductor quantum wells 2DEGs. Then, I describe the various scattering mechanisms present in two-dimensional systems, with an emphasis on scattering arising from charged impurities. Finally, I present the main theoretical model used to describe two-dimensional systems, Fermi liquid theory, along with an overview of the main experimental results obtained in coupled 2D systems such as 2D-2D tunneling and Coulomb drag.

2.1 Two-Dimensional Electron Gas

Despite living in a three-dimensional world, two-dimensional systems are not foreign by any means. Table games such as billiards, sports such as curling, 8-bit platform video games and simple drawings on a sheet of paper are just a few examples of common systems that are limited to two-dimensions. One simply needs a surface, or an interface, and a potential restraining matter to this surface. Classically, a reduced dimensionality system is not expected to behave much differently than a three-dimensional system. For a quantum mechanical system however, the situation cannot be more different. As depicted in figure 2.1, the available space for electrons (or particles more generally) to scatter becomes greatly reduced as the dimensionality of the system is reduced, leading to stronger electron-electron interactions. These stronger interactions lead to profound differences between the physics observed in three- and two-dimensional systems. For instance, no stable super-conductors have been observed in true two-dimensional systems [1]. Furthermore, in 2D, magnetic fields can strongly couple to electrons, leading to the emergence of the fractional quantum Hall effect [2–4].

Therefore, fabricating two-dimensional electron systems and studying the physics arising in them has been an active sub-field of physics for more than half a century since, in 1960, Attala and Kahng at Bell Labs [5] fabricated and measured the first two-dimensional electron gas (2DEG) at the Si/SiO$_2$ interface of a silicon MOSFET. Ever since, the field of 2D physics has been booming and 2DEGs have been realized in a large variety of materials such as electrons on the surface of liquid helium [6], III-V semiconductor interfaces

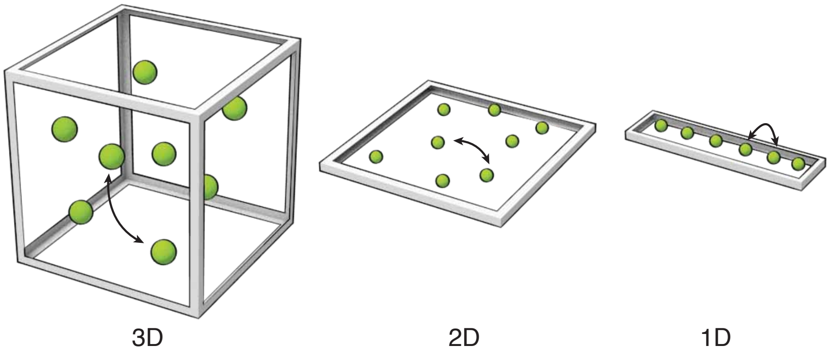

Fig. 2.1: Schematics of particles confined in 3D, 2D and 1D.

such as GaAs-AlGaAs [7], and graphene [8, 9], amongst many others. This has led in part to the development of CMOS, the backbone of modern transistor-based electronics, as well as being instrumental in three Nobel prizes, namely the discovery of the quantum Hall effect (QHE) [10], the fractional quantum Hall effect (FQHE) [11] and graphene [8]. For the remainder of this section, I will focus on the 2DEGs present at GaAs/AlGaAs interfaces, in large part because they are the substrate of choice for a 1D-1D Coulomb drag experiment, the subject of this thesis, owing to their unmatched cleanliness, *i.e.* ultra-high electronic mobility.

2.1.1 Doped AlGaAs/GaAs/AlGaAs Quantum Wells

Owing to the near identical crystalline lattice constant of its components, GaAs/AlGaAs heterostructures are the material of choice to create low-disordered interfaces and are unmatched for creating ultra-high mobility 2DEGs. The large electron affinity difference between the two heterostructure's components

($\sim$ 300 meV) creates a strong confining potential at the GaAs/AlGaAs interface whose energy levels can be estimated using basic quantum mechanics. For typical heterostructures,[1] the second 2D subband of this potential becomes populated at a temperature $T \sim 70$ K, while the first subband is populated even at the lowest temperatures. Therefore, when the temperature of a 2DEG is lowered below the second energy level threshold, the electrons are effectively trapped in the lowest energy level of this potential and form a near-ideal 2DEG, *i.e.* a 2DEG with near-zero thickness in the $\hat{z}$ direction that is only limited by the sample size in the $\hat{x}$ and $\hat{y}$ directions.

---

[1] For this thesis, a typical heterostructure is a delta-doped quantum well with a 30 nm width, a 2DEG buried 198 nm below the surface and a 2D density of $\sim 2 \times 10^{11}$ cm^{-2}.

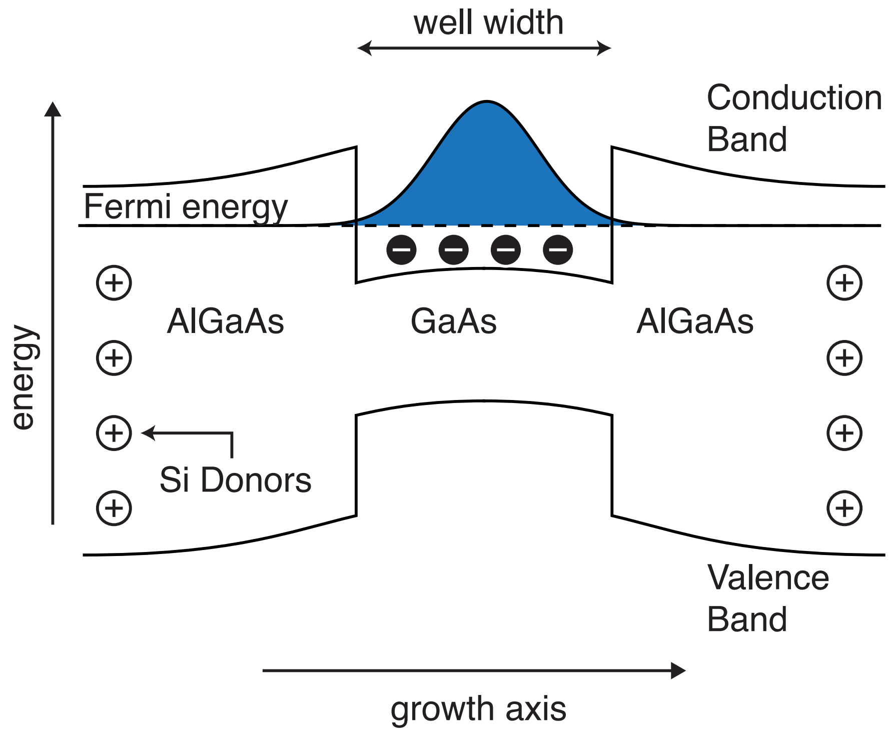

Fig. 2.2: Schematic of a modulation-doped AlGaAs/GaAs/AlGaAs quantum well heterostructure showing the resulting valence and conduction band energy profiles, along with the wave-function confinement.

Since GaAs and AlGaAs are both semiconductors, a single wafer using only these two materials would have only a small number of intrinsic electrons populating the 2DEG at low temperature, making low-temperature experimental measurements on the 2DEG extremely difficult. To circumvent this, one has to intentionally introduce donors, atoms with loosely bounded electrons that can "donate" electrons to the 2DEG and populate it with charge carriers, via external means.[2] However, in order to limit the disorder in the 2DEG, it is

---

[2] An alternative to doping is to deposit an overall gate on the heterostructure that will populate the 2DEG with electrons or holes when biased positively or negatively. This method can also be used in combination with doping to adjust *in situ* the carrier concentration of

also highly desirable to spatially separate the 2DEG and the donors using a technique called modulation doping, originally invented by Horst Störmer at Bell Labs [12]. Such modulation-doped heterostructures are grown using molecular-beam epitaxy (MBE), an ultra-high vacuum evaporation technique where extremely pure materials are deposited one atomic layer at the time. This technique, developed at Bell Labs by Alfred Cho in the late 1960's, allows to precisely grow heterostructures optimally designed for custom structures. In a sense, MBE allows some form of "wave function engineering" by tuning the interface depth, dopants and other parameters so as to shape the 2DEG confinement potential.

In our work, the 2DEG is confined within a symmetrically-doped square well consisting of two AlGaAs layers surrounding a single GaAs layer. A schematic of such a quantum well is shown in figure 2.2. Using the techniques described here, the low-temperature mobility of GaAs/AlGaAs 2DEGs has grown from roughly 2×10^4 cm^2/ V $\cdot$ s in 1978 [12] to 3.2×10^7 cm^2/ V $\cdot$ s in 2010 [13] for wells 30 nm wide, as depicted in figure 2.3. This has allowed the scientific community to achieve several breakthroughs in the understanding of the physics taking place in two-dimensional systems.

2.2 Scattering Mechanisms in GaAs/AlGaAs 2DEGs

The tremendous increase in GaAs/AlGaAs 2DEGs mobility has been achieved by minimizing the different scattering mechanisms that two-dimensional elec-

---

the 2DEG.

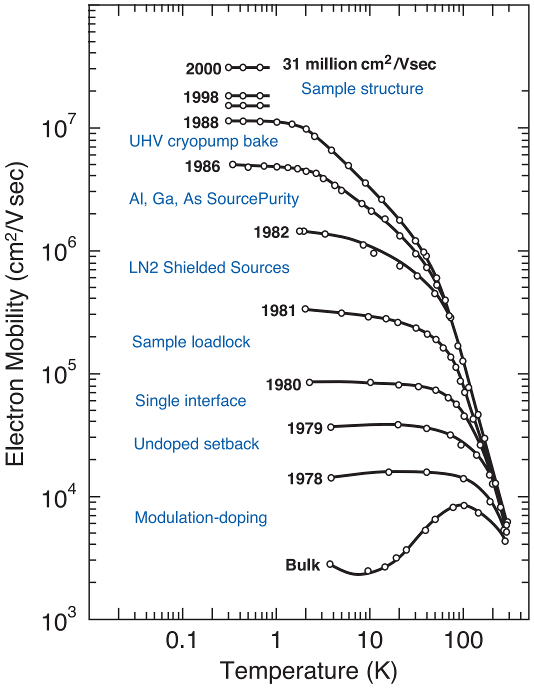

Fig. 2.3: Experimental data showing the historical increase of the 2DEGs low temperature mobility, along with the key material science improvements leading to this mobility increase. Figure taken from Pfeiffer and West [14].

trons are subjected to. In the following section, I describe the main scattering mechanisms arising in GaAs/AlGaAs heterostructures that unavoidably limit the 2DEG electron's mobility.

2.2.1 Description of the Main Scattering Mechanisms

As an electron is moving across a 2DEG, it is subjected to many scattering sources, thus hindering its progress and effectively reducing the conductivity of the material, *i.e.* its mobility. These quantities are effectively linked together by the Drude model of conductivity,

$$\sigma = n_e e \mu = n_e e^2 \tau / m^* \tag{2.1}$$

where σ is the electrical conductivity, n_e is the electron density, μ is the electron mobility, e is the electron charge, τ is the transport relaxation time, and m^* is the effective mass. The total scattering rate τ^{-1} is a combination of many different scattering mechanisms such as : (1) bulk phonon scattering in both the GaAs and the AlGaAs layers, including acoustic and optical phonons, (2) interface phonons, (3) alloy scattering in the AlGaAs layer, (4) interface roughness at the GaAs/AlGaAs interfaces, (5) charged impurity scattering by the intentional dopants in the modulation-doped layer, (6) charged impurity scattering by unintentional background charged impurities, (7) short-range scattering by unintentional neutral impurities and defects, and finally (8) inter-subband scattering. A schematic of these main scattering mechanisms is shown in figure 2.4.

In the vicinity of $T = 0$, these independent scattering sources can be combined using the Matthiessen rule,

$$\tau^{-1} = \sum_i \tau_i^{-1}. \tag{2.2}$$

Here, τ_i is the scattering rate of each individual scattering mechanism. Although the scattering rate is typically calculated at finite temperature, the Matthiessen rule nevertheless remains an useful approximation [15, 16]. In-

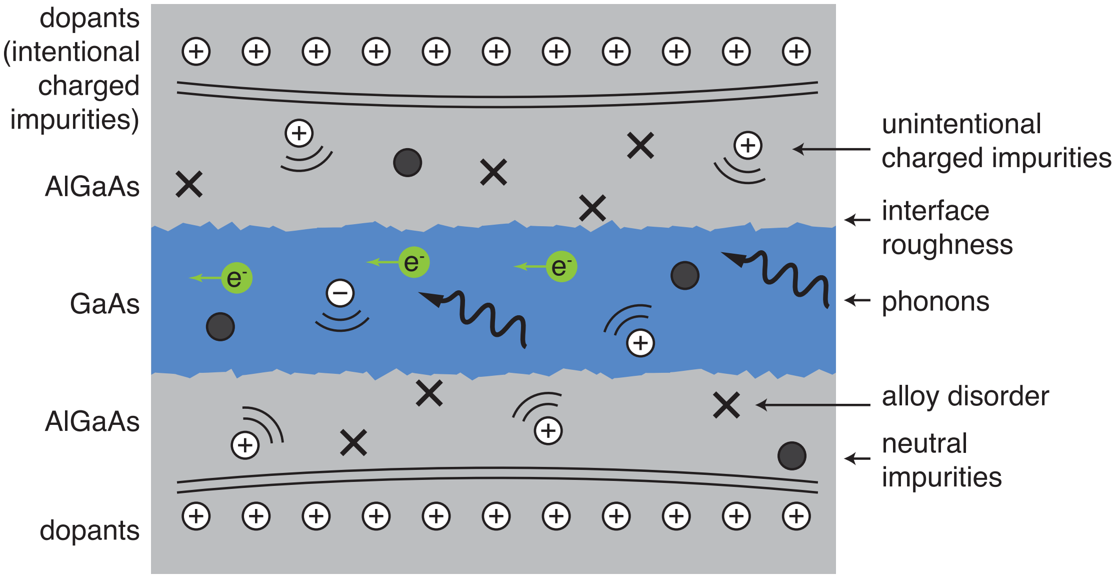

Fig. 2.4: Schematic of the main scattering mechanisms present in a modulation-doped AlGaAs/GaAs/AlGaAs quantum well heterostructure.

deed, the Matthiessen rule is valid as long as all the different scattering mechanisms are independent of one another. In GaAs/AlGaAs structures, deviations from the Matthiessen rule are typically smaller than 14%, and so it is a good approximation [16]. Before moving into the theoretical and experimental calculations and measurements of the scattering rate in 2DEGs, a qualitative description of the different scattering mechanisms and of their relative strength in low temperature GaAs/AlGaAs 2DEGs is provided.

(1) Bulk Phonons Scattering

The scattering by bulk phonons is intrinsic to the material and cannot be avoided at finite temperature. Scattering by optical phonons (LO phonons) is the dominant scattering mechanism at room temperature due to their dipolar nature and short-wavelength (high energy). However, this contribution falls off rapidly with temperature and is completely suppressed in the low temperature regime ($T \lesssim 10$ K) [17]. On the other hand, scattering caused by acoustic phonons, both via deformation coupling and piezoelectric coupling, does not decay as strongly with temperature due to their long wavelength nature (lower energy), remaining a non-negligible disorder source[3] down to $T \simeq 1$ K [15].

(2) Interface Phonons Scattering

Owing to the fact that GaAs and AlGaAs have a very similar lattice constant, density and dielectric constant, scattering arising from the interface phonons between these two materials should be weak and should not contribute strongly to the total 2D scattering rate [12].

(3) Alloy Scattering

As mentioned previously, the band-gap between GaAs and AlGaAs is $\sim$ 300 meV, therefore electrons in the quantum well can tunnel in the AlGaAs and then be scattered by the alloy disorder. Although this mechanism can be important in certain materials, such as in $\mathrm{Si}_x\mathrm{Ge}_{1-x}$ quantum wells [18], the penetration depth of the electrons in the AlGaAs section of an GaAs/AlGaAs heterostructure is small [19], consequently the scattering arising from this mechanism is negligible compared to other scattering mechanism such as interface roughness and charged impurities scattering [20].

---

[3] For example, at 4.2 K, acoustic phonon scattering alone would limit the mobility of a 2DEG to $\sim 20 \times 10^6$ cm^2/ V $\cdot$ s [15].

(4) Interface Roughness Scattering

Scattering can also arise due to the roughness of the AlGaAs/GaAs interface that is induced during the MBE growth process of GaAs/AlGaAs heterostructures. This mechanism can be quite important in GaAs/AlGaAs heterojunctions [20, 21] and in narrow (width $\leq$ 16 nm) or asymmetric quantum wells [22, 23] where the 2DEG wavefunction is located near the GaAs/AlGaAs interface. This contribution is also stronger in high electronic density 2DEGs as the electrons wavefunction is more pressed against the interface. However, for wider quantum well with a relatively small electronic density such as in this work, the wave function probability is strongly reduced near the interfaces and interface roughness is predicted to be a negligible scattering mechanism [15, 22].

(5) Intentional Charged Impurity Scattering

As mentioned previously, if one wants to have electrons populating the 2DEG of the semiconducting GaAs/AlGaAs quantum well without resorting to the use of electric fields (with a front or a back split-gate), one has to introduce donors, or dopants, in the system. In addition to populating the 2DEG with electrons, however, these dopants also induce disorder by creating a layer of positively charged atoms. This additional disorder can be mitigated by spatially separating the charged dopants and the 2DEG using modulation doping, thereby reducing the effect of the charged dopants through screening. If one is to move the dopants sufficiently far away from the 2DEG, their influence would be negligible; however as the dopants are moved farther from the 2DEG, it also becomes increasingly hard to populate it with electrons. Therefore, a compromise must be reached where the dopants have to be as far away as possible from the 2DEG while still being close enough to populate the 2DEG with electrons.

(6) Unintentional Charged Impurities Scattering

While the quality of MBE growth and the general purity of the materials used in GaAs/AlGaAs heterostructures have improved considerably over the last few decades, charged impurities in the base materials make their way in quantum well heterostructures and are generally the strongest source of disorder in high-mobility GaAs/AlGaAs wide quantum wells [15].

(7) Unintentional Neutral Impurities Scattering

Generally speaking, one would expect a comparable level of charged and neutral impurities to be present in GaAs/AlGaAs heterostructures. Under this assumption, charged impurities should always create more disorder than neutral impurities due to the strength of Coulomb interactions. Therefore, unintentional neutral impurities and defect scattering is negligible compared to the scattering generated by unintentional charged impuriries.

(8) Inter-Subband Scattering

Electrons in a 2DEG can also be subjected to inter-subband scattering if the density of the 2DEG is sufficiently large so that a second energy level begins to be populated in the quantum well. This scattering effect can be significant, reducing the 2DEG mobility by as much as ~ 30 %. However, this effect can be easily avoided by simply keeping the 2DEG's electron density low enough to prevent the population of additional energy levels (typically below 3.5×10^{11} cm^{-2} in our structures, but this density varies from sample to sample).

2.2.2 Theoretical Description of Charged Impurities Scattering Rate

There has been an extensive amount of work on scattering mechanisms in GaAs 2DEGs, both theoretically and experimentally [15, 17, 18, 20–34]. From a theoretical standpoint, the strength of the different scattering mechanisms is usually calculated using the Boltzmann theory, which is used to describe transport in a non-equilibrium thermodynamic system. This formalism has been used to calculate scattering rates in many materials for the majority of the scattering mechanisms discussed previously, namely alloy disorder [18, 25], phonon scattering [17], inter-subband scattering [24] and charged impurity scattering [15, 24].

For the remainder of this section, I will derive the general equation for the rate of charged impurity scattering within the relaxation-time approximation following the formalism described in Ashcroft and Mermin [35]. Only scattering by charged impurities will be formally considered since it is the dominant scattering mechanism in wide high-mobility GaAs/AlGaAs quantum wells [15]. We begin by introducing a quantity $W_{\mathbf{k},\mathbf{k}'}$, which is defined as : "The probability in an infinitesimal time dt that an electron with a wave vector $\mathbf{k}$ is scattered into any one of the group levels (with the same spin) contained in the infinitesimal k-space volume element $d\boldsymbol{k'}$ about $\boldsymbol{k}'$, assuming that these levels are all unoccupied (and therefore not forbidden by the exclusion principle) is,

$$\frac{W_{\boldsymbol{k},\boldsymbol{k'}} dt d\boldsymbol{k'}}{(2\pi)^3} \tag{2.3}$$

[35]." Thus, using $W_{\boldsymbol{k},\boldsymbol{k'}}$ and $g(\boldsymbol{r}, \boldsymbol{k}, t)$, the semi-classical electron distribution function, the total probability per unit of time of electrons scattering in an open state with wave vectors $\boldsymbol{k}'$, which is simply $\tau(\boldsymbol{k})^{-1}$, is given by

$$\int d\boldsymbol{k'} W_{\boldsymbol{k},\boldsymbol{k'}}[1 - g(\boldsymbol{k'})] = \tau(\boldsymbol{k})^{-1}. \tag{2.4}$$

Using equation 2.4 and considering the contribution from electrons suffering a collision and scattering both into and out of the level $\boldsymbol{k}$, the change to the number of electrons per unit of volume caused by all collisions, $\left(\frac{\partial g}{\partial t}\right)_{coll}$, is

$$\left(\frac{\partial g(\boldsymbol{k})}{\partial t}\right)_{coll} = -\int \frac{d\boldsymbol{k'}}{(2\pi)^3}\Big(W_{\boldsymbol{k},\boldsymbol{k'}} g(\boldsymbol{k})[1 - g(\boldsymbol{k'})] - W_{\boldsymbol{k'},\boldsymbol{k}} g(\boldsymbol{k'})[1 - g(\boldsymbol{k})]\Big). \tag{2.5}$$

If the impurity potential is real and spatially invariant (which we assume to be the case), the scattering potential is Hermitian and $W_{\mathbf{k},\mathbf{k}'} = W_{\mathbf{k}',\mathbf{k}}$. Using this property, equation 2.5 simplifies to

$$\Big(\frac{\partial g(\boldsymbol{k})}{\partial t}\Big)_{coll} = -\int \frac{d\boldsymbol{k'}}{(2\pi)^3} W_{\mathbf{k},\mathbf{k}'}[g(\boldsymbol{k}) - g(\boldsymbol{k'})]. \tag{2.6}$$

Alternatively, this change to the electron's distribution caused by collision can also be obtained using the relaxation-time approximation. The approximation is valid as long as two assumptions hold. First, one must consider that the distribution of electrons emerging from collisions at any given time does not depend on the non-equilibrium distribution function $g(\boldsymbol{r}, \boldsymbol{k}, t)$ prior to the collision. At equilibrium, the system must also satisfy the equality $g(\boldsymbol{r}, \boldsymbol{k}, t) = g^0(\boldsymbol{r}, \boldsymbol{k}) = \frac{1}{e^{(\epsilon(k)-\mu(\boldsymbol{r}))/k_B T(\boldsymbol{r})}+1}$ where $\mu(\boldsymbol{r})$ is the chemical potential, $g^0(\boldsymbol{r}, \boldsymbol{k})$ is the local distribution function and

$$\frac{1}{e^{(\epsilon(k)-\mu(\boldsymbol{r}))/k_B T(\boldsymbol{r})} + 1} = f_F(\epsilon(\boldsymbol{k})) \tag{2.7}$$

is the Fermi distribution function. When these assumptions are satisfied, the collision term is completely determined and is defined by

$$\Big(\frac{\partial g(\boldsymbol{k})}{\partial t}\Big)_{coll} = -\frac{[g(\boldsymbol{k}) - g^0(\boldsymbol{k})]}{\tau(\boldsymbol{k})}. \tag{2.8}$$

Using the equality between equation 2.6 and equation 2.8 while assuming that the impurities are isotropic, that the energy $\epsilon(\mathbf{k})$ depends only on the magnitude of $\mathbf{k}$ and that the scattering is elastic, we find that, in the relaxation-time approximation,

$$\frac{1}{\tau(\boldsymbol{k})} = \int \frac{d\boldsymbol{k'}}{(2\pi)^3} W_{\boldsymbol{k},\boldsymbol{k'}}(1 - \hat{\boldsymbol{k}} \cdot \hat{\boldsymbol{k'}}). \tag{2.9}$$

It can be shown that this relaxation-time approximation solution provides the same description of scattering as the full Boltzmann equation does,

$$\frac{\partial g}{\partial t} + \mathbf{v} \bullet \frac{\partial}{\partial \boldsymbol{r}} g + \boldsymbol{F} \bullet \frac{\partial}{\partial \boldsymbol{k}} g = \left(\frac{\partial g}{\partial t}\right)_{coll}, \tag{2.10}$$

where $\mathbf{v}$ is the electron's velocity and $\mathbf{F}$ is a force caused by an externally applied electric field.

Since we are considering impurities in a crystal that are static and would produce elastic scattering, we can use Fermi-Golden rule so that

$$W_{\boldsymbol{k},\boldsymbol{k'}} = \sum_{\beta} \frac{2\pi}{\hbar} N_i^{\beta} \delta(\epsilon(k) - \epsilon(k')) | < k|U|k' > |^2, \tag{2.11}$$

where δ is the usual delta-function, N is the number of impurities per unit of volume, β is the type of impurity (dopants and unintentional background impurities for our purpose) and U is the impurity potential.

Finally, considering Coulomb interactions alone, the charged impurity scattering rate can be written as

$$\frac{1}{\tau(\boldsymbol{k})} = \frac{2\pi}{\hbar}\sum_{\beta}\int\frac{d^2k'}{(2\pi)^2}\int_{-\infty}^{\infty}dzN_i^{\beta}(z)\times|u^{\beta}(\boldsymbol{k}-\boldsymbol{k'};z)|^2(1-cos\theta_{\boldsymbol{kk'}})\delta(\epsilon(k)-\epsilon(k')), \tag{2.12}$$

where u^{β} is the 2D fourier transform of the screened scattering potential of the impurities of the β^{th} type and $\theta_{\boldsymbol{kk'}}$ is the angle between $\boldsymbol{k}$ and $\boldsymbol{k'}$. In GaAs/AlGaAs materials, there are usually two kind of charged impurities : the unintentional background charged impurities and the 2D layer of delta dopants introduced by the modulation doping technique. Using equation 2.12 and the specific scattering potential for each impurity type, along with the appropriate screening technique, many authors have theoretically calculated the charged impurity scattering rate and compared it with experimental data. The main results from these calculations are presented in the next subsection.

2.2.3 Previous Experimental Measurements and Simulations of Scattering in 2DEGs

To experimentally determine the dominant scattering mechanisms in heterostructures, one usually varies the electronic density of the 2DEG, generally using red LED illumination or via an overall gate that can be biased at different voltages, and measures the resulting mobility at each electronic density. To compare these experimental results with the theoretical data obtained using equation 2.12, it is common for both the experimental and the theoretical literature to express their findings concerning the electron's scattering rate as

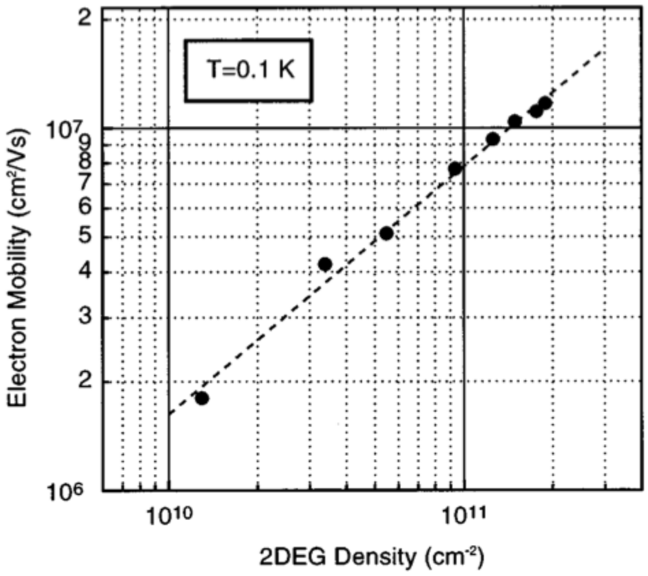

Fig. 2.5: Data showing a typical mobility versus 2D density plot, along with a power-law fit to the data. In this case, the density was varied using different levels of red LED illumination and the exponent best fitting the curve is $\alpha = 0.68$. Figure taken from Umansky *et al.* [21].

an electronic density dependence of the mobility, namely

$$\mu \propto n^{\alpha}, \tag{2.13}$$

where the value of the power-law exponent α provides information on the nature of the dominant scattering mechanism. An example of such a measurement from Umansky *et al.* [21] is presented in figure 2.5. A general consensus amongst theoretical and experimental studies in wide ($\gtrsim$ 30nm) GaAs/AlGaAs quantum wells at low temperature (T $\leq$ 4.2 K) is that the two main scattering mechanisms are *i)* scattering by the intentional dopants, which is characterized by an exponent α between 1.2 and 1.5 [15, 34], and *ii)* scattering by the unintentional background charged impurities, which is characterized by an exponent $\alpha \lesssim 1$ [15, 21, 27, 33]. The variation in exponent α between scattering by intentional and unintentional charged impurities arises from the overall difference in distance between the charged impurities and the electrons gas. The intentional charged impurities are distant from the 2DEG and are ineffectively screened while the unintentional charged impurities are present everywhere, including in the 2DEG itself, and so are more effectively screened. Interface roughness has mostly been ruled out as a dominant scattering mechanism in these quantum wells since it would be characterized by an exponent $\alpha \sim 0$ [15], which is inconsistent with the vast majority of the experimental data from the literature. In chapter 3 of this thesis, I will present new experimental data regarding the scattering mechanisms taking place in doped shallow 2DEGs.

2.3 Theoretical Approach to Transport in 2DEGs

2.3.1 Fermi-Liquid Theory

Since there are usually $\sim 2{\times}10^{11}$ electrons per cm^2 in a typical GaAs/AlGaAs 2DEG, calculating the interactions between all these particles and the surrounding crystalline lattice would be an overwhelming task. To address the physics of interacting fermionic systems, Landau developed in 1957 a theoretical model called the Fermi-liquid theory [36]. This cornerstone of condensed matter physics is often used to describe the physics taking place in low-temperature fermionic systems such as 2DEGs and degenerate liquid helium-3, as originally envisioned by Landau.

The main assumption behind Fermi liquid theory is that there exists a one to one correspondence between the low energy excitations of an interacting system and those of a free electron gas. Thus, the low-energy excitations of an interacting system can be approximated by fermionic quasi-particles behaving like free electrons, albeit with a different mass. In general, this “effective mass”, labeled m^*, depends on both the energy and the direction of the electrons, and is therefore described by an effective mass tensor that accounts for most of the interaction effects of the original system. In the simple case where the effective mass is isotropic and is calculated near an energy minimum (assuming a quadratic energy dispersion relation), it can be approximated by a scalar defined as

$$m^* = \hbar^2 \frac{d^2\epsilon(\boldsymbol{k})}{d\boldsymbol{k}^2}, \tag{2.14}$$

where $\hbar$ is the Planck’s constant, $\epsilon(\boldsymbol{k})$ is the energy distribution function and $\boldsymbol{k}$ is the wave vector. This effective mass is however notoriously hard to calculate and is usually experimentally determined. For instance, in GaAs, $m^* = 0.067$ m_e, or 0.067 times the free electron mass. This model holds as long as the excitations have low energy (*i. e.* $T \ll E_F \sim 70$ K for a typical GaAs/AlGaAs heterostructure). In addition, it also requires that the interactions do not induce symmetry-breaking ground-states or phase transitions (as in the case of superconductivity for instance). Under these conditions, transport is described by the Boltzmann equation and the Fermi energy E_F can be linked to the two-dimensional electron density following the free electron formalism,

$$n_e = \frac{k_F^2}{2\pi} \tag{2.15}$$

$$E_F = \frac{\hbar^2 k_F^2}{2m^*}, \tag{2.16}$$

where k_F is the Fermi wave vector. Fermi liquid theory has been extremely successful in describing many qualitative properties of low temperature systems such as the linear temperature dependence of the specific heat of metals, along with the quadratic temperature dependence of the resistivity of metals, to only name a few.

2.3.2 Landau Levels in Magnetic Fields

A specific feature of 2DEGs is that, when subjected to an external perpendicular magnetic field, their available energy levels become quantized in what is known as Laudau levels. The energy E_N of these Landau levels is defined as

$$E_N = \hbar\omega_c(N + 1/2); N \geq 1, \tag{2.17}$$

where N is an integer and ω_c is the cyclotron frequency defined as

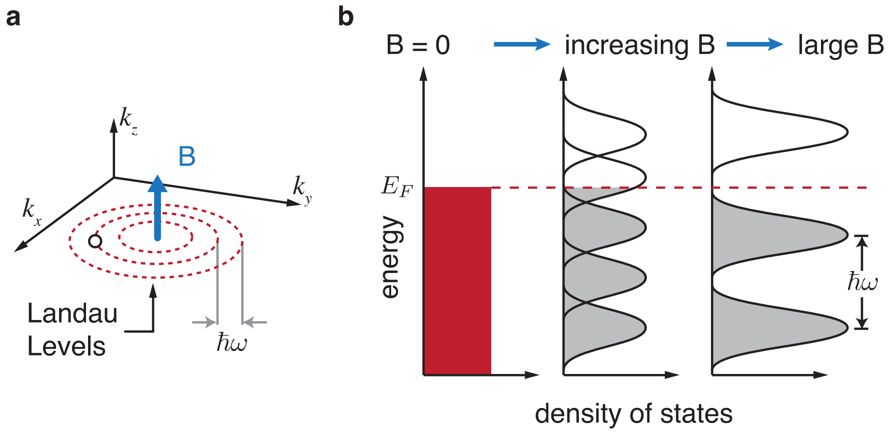

Fig. 2.6: **(a)** Schematic showing how electrons become confined in concentric orbits in the presence of a magnetic field. **(b)** Schematics showing how Landau levels become separated with increasing magnetic field, causing fewer Landau levels to be populated at larger magnetic fields for a fixed 2D electronic density. The Landau levels are shown as disorder broadened, rather than as ideal δ-functions in the density of states. Figure taken from C. R. Dean [37].

$$\omega_c = \frac{eB}{m^*}. \tag{2.18}$$

Here, e is the electron charge and B is the magnetic field strength. Consequently, the continuous density of state in the absence of magnetic field collapses into a degenerate set of δ-functions corresponding to the Landau levels when a magnetic field is applied. This idealized picture of Landau levels is slightly modified in real devices where disorder scattering broadens the width (in energy space) of the Landau levels. As the magnetic field increases, the degeneracy of Landau levels increases, effectively reducing the number of Landau levels populated, until all the electrons in the 2DEG are located in a single Landau level. At specific magnetic field values B_ν, an integer number of Landau levels are completely filled, defining the filling factor ν

$$\nu = \frac{1}{B_\nu}\frac{n_e h}{e}. \tag{2.19}$$

Schematics of this behavior are depicted in figure 2.6. The existence of Landau levels has been observed experimentally through Shubnikov-De Haas (SdH) oscillations [38] and the discovery of the quantum Hall effect [39]. An example of such measurements is shown in figure 2.7.

2.4 Transport in Coupled 2D-2D Systems

In this section, some of the most important experimental findings regarding coupled two-dimensional systems will be discussed. These coupled 2D-2D systems form the basis from which 1D-1D vertically-integrated quantum wires are fabricated. These experiments are realized in MBE-grown double quantum well heterostructures where two quantum wells are separated by a thin $Al_x(GaAs)_{1-x}$ layer grown *in situ* and acting as a barrier. The width of this barrier can be tuned and is typically between 3 nm and 50 nm wide.

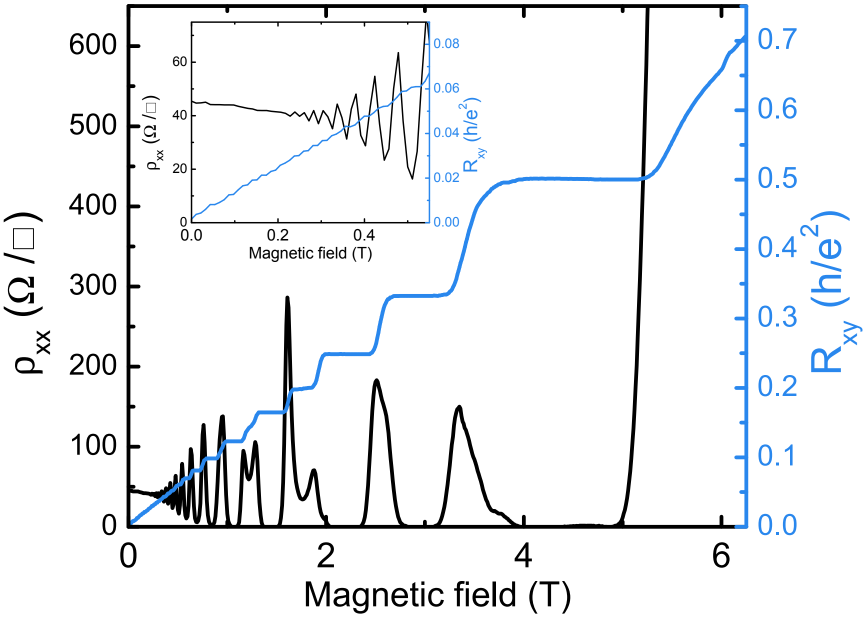

Fig. 2.7: Experimental data from wafer VA0142 showing typical SdH oscillations (black curve, left axis) and the quantum Hall effect (blue curve, right axis). The data was taken in a helium-3 refrigerator at 330 mK and the inset zooms on the data in the low magnetic field regime.

2.4.1 Selective Depletion Technique

One of the simplest experiments one can imagine between coupled two-dimensional systems is to measure the rate of quantum tunneling for electrons passing from one layer to the next. While basic quantum mechanics is sufficient to predict such a phenomenon, it was not until the early 90's, through selective depletion of the 2DEGs using electrostatic split gates [40], that true 2D-2D tunneling between quantum wells was realized [41].

Figure 2.8 sketches the layout of the selective depletion technique. Through the use of both front and back gates, it is possible to selectively deplete part

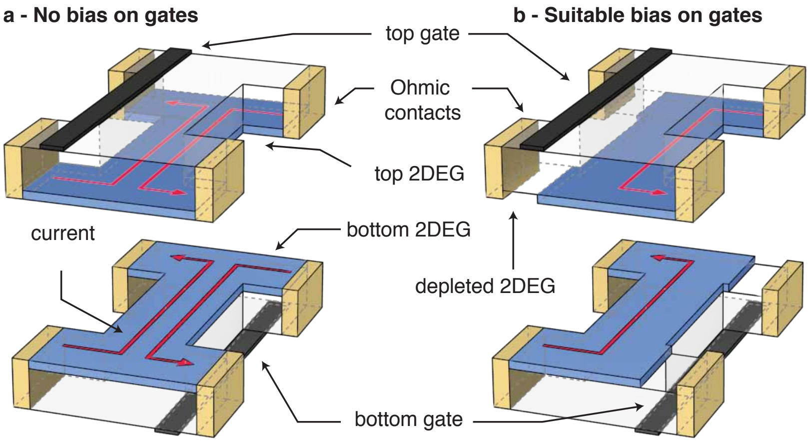

Fig. 2.8: **(a)** Schematic of a double quantum well heterostructure with gates designed to independently contact each 2DEG. The top and bottom parts of the heterostructure are separated for clarity purposes. With no bias on the gates, current (in red) sourced through one set of contacts flows through both layers. **(b)** Independent contacts to each layer are achieved when a suitable bias is applied to both gates. In this schematic, the right ohmic contacts only probe the top 2DEG and the left ohmic contacts only probe the bottom 2DEG.

of the 2DEGs such that the conduction in the top (bottom) layer is prevented on the left (right) side of the device (as depicted in figure 2.8 **b**), given that a suitable voltage is applied on each gate. For this reason, although ohmic contacts unavoidably electrically connect both layers, they can still be used as source-drain for a single 2DEG.

2.4.2 2D-2D Tunneling

Using this selective depletion technique, Eisenstein *et al.* [41] performed the first 2D-2D tunneling experiments in 1991 at Bell labs. In the absence of magnetic field, a resonant tunneling peak, shown in figure 2.9, is observed whenever the energy and momentum of both 2D subbands align, being consistent with an interactionless single particle description of the tunneling process. Experimentally, introducing a source-drain bias between the two layers or changing the density of either 2DEG via an overall top or back gate will allow one to match the 2D subbands in the 2DEGs and produce the resonant tunneling peak. The width of this peak is usually attributed to inelastic scattering caused by impurities or density inhomogeneities causing a continuum of momentum values to induce resonant tunneling.

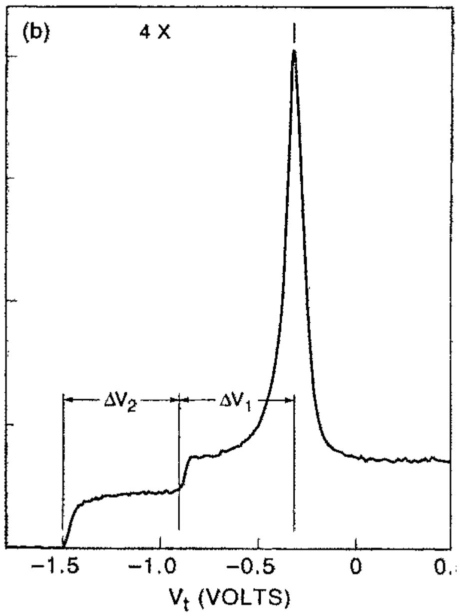

Fig. 2.9: Tunneling resonant peak observed in a 2D-2D tunneling experiment. The figure shows the tunneling conductance as a function of top gate voltage (V_t) where a change in the top gate voltage effectively changes the density of the top 2DEG. Figure taken from Eisenstein *et al.* [41].

However, this picture changes significantly in the presence of a perpendicular magnetic field. In this case, the electrons become magnetically localized, and so the interactionless electrons picture is not suitable anymore to describe the system. In the lowest Landau level (that is, for $B \gtrsim 6.6$ T for the sample used by Eisenstein *et al.* [42]), and for 2DEGs with matching density (hence energy), the resonant peak that is observed at zero source-drain bias disappears, leading instead to a pair of peaks shifted to higher energy (or higher source-drain bias). This can be explained by localization since it takes a significant amount of energy to extract an electron from the initial 2DEG and then relocate it to the other layer. This tunneling gap is thus the experimental observation of the extra energy cost for tunneling. In addition, inter Landau level tunneling can also be observed, but only at a much higher energy (*i.e.* at higher source-drain bias) [42].

2.4.3 2D-2D Coulomb Drag

Another type of experiment that can be performed in coupled 2D systems is the so-called *Coulomb drag* experiment. As shown in figure 2.10, a Coulomb drag experiment consists of sourcing a drive current I_{drive} through one of the layers while measuring the resulting drag voltage V_{drag} arising in the other layer under the condition of no current flow in this drag layer. When tunneling and phonon-induced drag are negligible, this Coulomb drag signal results solely from inter-layer electron-electron scattering and is therefore a direct probe of electron-electron interactions [43, 44].

The drag voltage arises primarily from momentum transfer between the electrons of the drive layer and those in the drag layer. In a sense, this can be interpreted as “mutual friction” between the two 2DEGs. In general, electrons

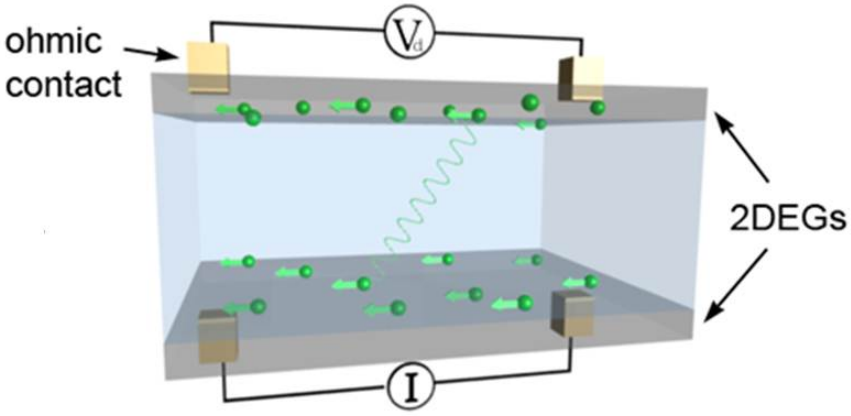

Fig. 2.10: Schematic of two-dimensional Coulomb drag showing the electron's motion in both the drive and the drag layers.

in the drag layer will push against the current direction (*i.e.* in the same direction as the electrons flow in the drive layer) and will accumulate until the electrostatic force balances the opposite force coming from momentum transfer. This mechanism relies on electron-hole asymmetry ensuring that the contribution to Coulomb drag from electrons and virtual holes do not cancel each other out.

Using a formalism analogous to the Drude model for transport, the rate at which momentum is transferred is

$$\frac{m^* \boldsymbol{v_d}}{\tau}, \tag{2.20}$$

where $\boldsymbol{v_d}$ is the drift velocity and τ is the scattering time. Since the electrostatic force must cancel the momentum transfer rate, we have

$$e\boldsymbol{E} = \frac{m^* \boldsymbol{v_d}}{\tau}, \tag{2.21}$$

where **E** is the generated electric field. Coulomb drag measurements are usually reported in terms of drag resistance, or transresistance, defined as

$$R_D = \frac{-V_{drag}}{I_{drive}}, \tag{2.22}$$

where the negative sign is introduced here such that, under normal conditions, the drag resistance is defined as a positive quantity. Rewriting equation 2.22 using equation 2.21, one obtains

$$R_D = \frac{A\boldsymbol{E}}{n_e \boldsymbol{v_d}} = \frac{Am^*}{n_e e^2 \tau}, \tag{2.23}$$

where A is the area over which both 2DEGs are interacting. The scattering rate can be evaluated analytically using the Boltzmann transport theory (equation 2.10) for weak coupling (*i.e.* low temperature and large interlayer separation, $T \ll T_F \sim 70$ K and $1 \ll k_F d \sim 2$) within the Born approximation and neglecting the finite width of the 2DEGs [45, 46]. Under these assumptions, and using Thomas-Fermi screening, this scattering rate is given by

$$\tau^{-1} = \frac{\pi\zeta(3)(k_B T)^2 m^*}{16\hbar(2\pi\hbar)^2 n_{e_1} n_{e_2} q_{TF}^2 d^4} \tag{2.24}$$

and the drag resistance by

$$R_D = \frac{A\pi\zeta(3)(k_B T)^2 (m^*)^2}{16\hbar e^2 (2\pi\hbar)^2 (n_{e_1} n_{e_2})^{3/2} q_{TF}^2 d^4}. \tag{2.25}$$

Here, $\zeta(3) \sim 1.202$ is the Riemann-zeta function, n_{e_1}, n_{e_2} are the densities in the first and second layers respectively and q_{TF} is the Thomas-Fermi screening wave vector for two-dimensional systems.

Key features of this theoretical result are the fourth power dependence on the interlayer separation, the third power dependence on the layers density and the quadratic dependence on temperature. The quadratic dependence on temperature can be qualitatively understood in term of the available phase-space for scattering : at finite temperature, electrons can only scatter in empty states within a range $k_B T$ around the Fermi-energy. Since two electrons are required for momentum exchange to take place, the scattering rate is proportional to $(k_B T)^2$. This simple picture is however not entirely exact as the phase-space for backscattering diverges in two dimensions, creating logarithmic corrections to this expected T^2 behavior of 2D-2D Coulomb drag [47].

Early Coulomb drag experiments in electron-electron bilayers were consistent with equation 2.25, with only minor deviations from the quadratic temperature dependence. This is shown in figure 2.11, taken from a seminal experiment performed by Eisenstein *et al.* at Bell Labs [45] in bilayers separated by a barrier 17.5 nm wide. The expected logarithmic deviations from the T^2 temperature dependence of Coulomb drag have been observed in subsequent studies performed in bilayer structures with a much smaller interlayer separation [48]. These measurements are consistent with drag occurring from electron-electron scattering and not scattering from the lattice vibrations. Drag arising from electrons scattering off lattice vibrations, or phonon drag, has been found to be significant only for bilayers with an interlayer separation of ~ 50 nm and larger [49].

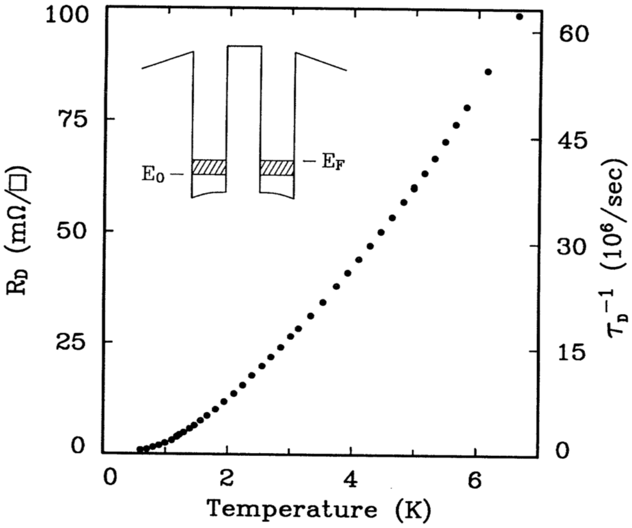

Fig. 2.11: Experimental data showing the typical quadratic temperature dependence of 2D-2D Coulomb drag. Figure taken from Gramila *et al.* [45].

In a perpendicular magnetic field, this picture of Coulomb drag changes dramatically. For layers with identical densities, the magnetic field has the effect of increasing the strength of the drag signal by a factor up to ~ 1000 for $\nu = 1/2$ in each layer (B ~ 11T) and to modulate the drag signal as a function of the Landau level filling factor [50, 51]. In the case of layers with unmatched densities, or equivalently unmatched filling factors, the situation is even more complex. In the presence of magnetic fields larger than ~ 0.5 T, the drag signal oscillates between positive and negative values, with the negative values of Coulomb drag occurring when the filling factor of both 2DEGs differs by an odd number [51, 52].

These observations can be understood when one considers the role of electron-hole asymmetry in the drag measurement. When the 2D layers have matching electronic densities, the positive Coulomb drag signal arises from an electron-hole asymmetry in the curvature of the momentum distribution of electrons and holes. Therefore, the positive electron-electron drag is stronger than the electron-hole negative drag because the electrons have a larger momentum. If electrons and holes had an identical momentum, there would be no drag signal. However, when the two 2D layers have a significantly different filling factor, an additional negative contribution to Coulomb drag arises from an electron-hole asymmetry in the density of states of the electrons and the holes [53, 54], increasing the effective number of holes in the system and thus generating additional negative electron-hole drag. When the difference between the filling factor of both layers is odd, this contribution is maximal and an overall negative drag is observed. A schematic of this behavior is presented in figure 2.12.

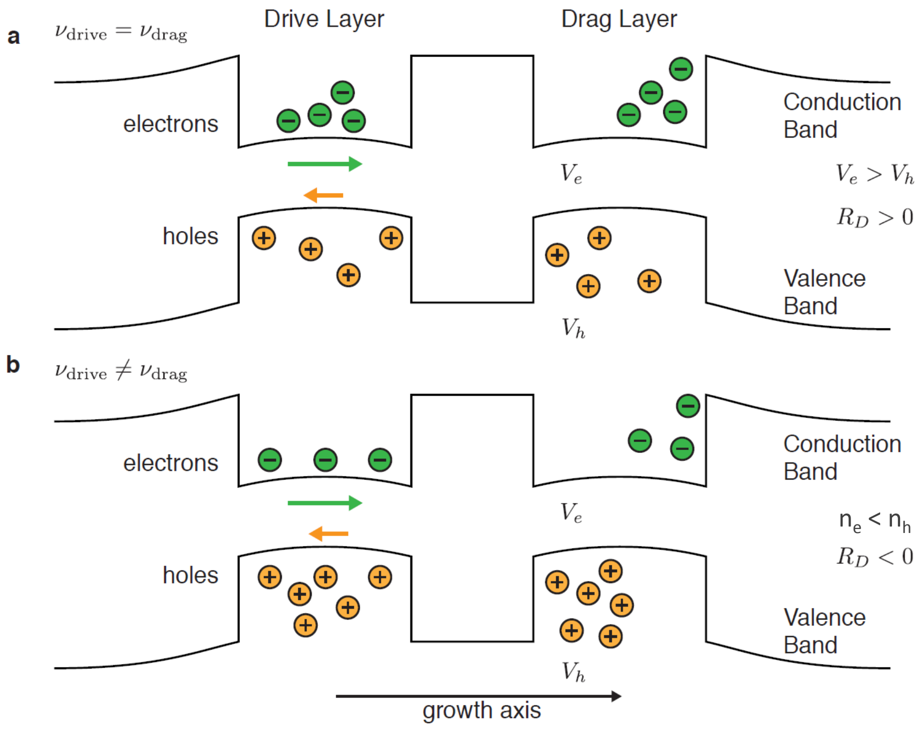

Fig. 2.12: Schematics of the model used by Gornyi *et al.* [53] to describe the emergence of a negative two-dimensional Coulomb drag between 2DEGs with an odd difference between their filling factor. **(a)** Identical filling factor between the layers. The electron-hole asymmetry arises through a different curvature (and hence different velocities, $v_e > v_h$) for electrons and holes, yielding an effective positive Coulomb drag. This is depicted by the green and orange arrows having a different length. **(b)** Odd difference between the filling factor of both 2DEGs. An additional contribution to Coulomb drag arises from an electron-hole asymmetry in the density of state (and hence a different number of electrons and holes), yielding to a negative Coulomb drag signal.

References

[1] Qin, S., Kim, J., Niu, Q., and Shih, C. K. *Science* **324**, 1314 (2009).

[2] Tsui, D. C., Störmer, H. L., and Gossard, A. C. *Phys. Rev. Lett.* **48**, 1559 (1982).

[3] Jain, J. K. *Phys. Rev. Lett.* **63**, 199 (1989).

[4] Halperin, B. I., Lee, P. A., and Read, N. *Phys. Rev. B* **47**, 7312 (1993).

[5] Kahng, D. *Electric Field Controlled Semiconductor Device.* U. S. Patent No. 3102230. Filed May 31, 1960, issued August 27, 1963.

[6] Sommer, W. T. *Phys. Rev. Lett.* **12**, 271 (1964).

[7] Störmer, H. L., Dingle, R., Gossard, A. C., Wiegmann, W., and Sturge, M. D. *Solid State Commun.* **29**, 705 (1979).

[8] Novoselov, K. S., Geim, A. K., Morozov, S. V., Jiang, D., Zhang, Y., Dubonos, S. V., Grigorieva, I. V., and Firsov, A. A. *Science* **306**, 666 (2004).

[9] Novoselov, K. S., Jiang, D., Schedin, F., Booth, T. J., Khotkevich, V. V., Morozov, S. V., and Geim, A. K. *Proc. Natl Acad. Sci. USA* **102**, 10451 (2005).

[10] von Klitzing, K., Dorda, G., and Pepper, M. *Phys. Rev. Lett.* **45**, 494 (1980).

[11] Tsui, D. C., Störmer, H. L., and Gossard, A. C. *Phys. Rev. Lett.* **48**, 1559 (1982).

[12] Störmer, H. L. *Surf. Sci.* **132**, 519 (1983).

[13] Kumar, A., Csáthy, G. A., Manfra, M. J., Pfeiffer, L. N., and West, K. W. *Phys. Rev. Lett.* **105**, 246808 (2010).

[14] Pfeiffer, L. and West, K. W. *Physica E* **20**, 57 (2003).

[15] Hwang, E. H. and Das Sarma, S. *Phys. Rev. B* **77**, 235437 (2008).

[16] Saxena, A. K. and Mudares, M. A. L. *J. Appl. Phys.* **58**, 2795 (1985).

[17] Kawamura, T. and Das Sarma, S. *Phys. Rev. B* **45**, 3612 (1992).

[18] Venkataraman, V., Liu, C. W., and Sturm, J. C. *Appl. Phys. Lett.* **63**, 2795 (1993).

[19] Price, P. J. and Stern, F. *Surface Sci.* **132**, 577 (1983).

[20] Yang, B., Cheng, Y. H., Wang, Z. G., Liang, J. B., Liao, Q. W., Lin, L. Y., Zhu, Z. P., Xu, B., and Li, W. *Appl. Phys. Lett.* **65**, 3329 (1994).

[21] Umansky, V., Picciotto, R., and Heiblum, M. *Appl. Phys. Lett.* **71**, 683 (1997).

[22] Luhman, D. R., Tsui, D. C., Pfeiffer, L. N., and West, K. W. *Appl. Phys. Lett.* **91**, 072104 (2007).

[23] Lima, F. M. S., Fonseca, A. L. A., Nunes, O. A. C., Qu, F., Freire, V. N., and da Silva Jr., E. F. *Physica E* **17**, 322 (2003).

[24] Ando, T., Fowler, A. B., and Stern, F. *Rev. Mod. Phys.* **54**, 437 (1982).

[25] Bockelmann, U., Abstreiter, G., Weimann, G., and Schlapp, W. *Phys. Rev. B* **41**, 7864 (1990).

[26] Shayegan, M., Goldman, V. J., Jiang, C., Sajoto, T., and Santos, M. *Appl. Phys. Lett.* **52**, 1086 (1988).

[27] Jiang, C., Tsui, D. C., and Weimann, G. *Appl. Phys. Lett.* **53**, 1533 (1988).

[28] Kurobe, A., Frost, J. E. F., Grimshaw, M. P., Ritchie, D. A., Jones, G. A. C., and Pepper, M. *Appl. Phys. Lett.* **62**, 2522 (1993).

[29] Grimshaw, M. P., Ritchie, D. A., Burroughs, J. H., and Jones, G. A. C. *J. Vac. Sci. Technol.* **B 12**, 1290 (1994).

[30] Kane, B. E., Pfeiffer, L. N., and West, K. W. *Appl. Phys. Lett.* **67**, 1262 (1995).

[31] Kawaharazuka, A., Saku, T., Hirayama, Y., and Horikoshi, Y. *J. Appl. Phys.* **87**, 952 (2000).

[32] Kawaharazuka, A., Saku, T., Kikuchi, C. A., Horikoshi, Y., and Hirayama, Y. *Physica E* **13**, 663 (2002).

[33] Manfra, M. J., Hwang, E. H., Das Sarma, S., Pfeiffer, L. N., West, K. W., and Sergent, A. M. *Phys. Rev. Lett.* **99**, 236402 (2007).

[34] Laroche, D., Das Sarma, S., Gervais, G., Lilly, M. P., and Reno, J. L. *Appl. Phys. Lett.* **96**, 162112 (2010).

[35] Ashcroft, N. W. and Mermin, N. D. *Solid State Physics.* Thompson Learning INC., (1976).

[36] Landau, L. D. *Sov. Phys. JETP.* **3**, 920 (1957).

[37] Dean, C. R. *A Study of the Fractional Quantum Hall Energy Gap at Half Filling.* Ph. D. dissertation, McGill University, (2008).

[38] Stern, F. and Howard, W. E. *Phys. Rev.* **163**, 816 (1967).

[39] von Klitzing, K., Dorda, G., and Pepper, M. *Phys. Rev. Lett.* **45**, 494 (1980).

[40] Eisenstein, J. P., Pfeiffer, L. N., and West, K. W. *Appl. Phys. Lett.* **57**, 2324 (1990).

[41] Eisenstein, J. P., Pfeiffer, L. N., and West, K. W. *Appl. Phys. Lett.* **58**, 1497 (1991).

[42] Eisenstein, J. P., Pfeiffer, L. N., and West, K. W. *Phys. Rev. Lett.* **69**, 3804 (1992).

[43] Pogrebinskii, M. B. *Sov. Phys. Semicond.* **11**, 372 (1977).

[44] Price, P. J. *Physica B* **117**, 750 (1983).

[45] Gramila, T. J., Eisenstein, J. P., MacDonald, A. H., Pfeiffer, L. N., and West, K. W. *Phys. Rev. Lett.* **66**, 1216 (1991).

[46] Jauho, A. P. and Smith, H. *Phys. Rev. B.* **47**, 4420 (1993).

[47] Rojo, A. G. *J. Phys. Condens. Matter* **11**, R31 (1999).

[48] Kellogg, M., Eisenstein, J. P., Pfeiffer, L. N., and West, K. W. *Solid State Comm.* **123**, 515 (2002).

[49] Bønsager, M. C., Flensberg, K., Hu, B. Y. K., and MacDonald, A. H. *Phys. Rev. B* **57**, 7085 (1998).

[50] Lilly, M. P., Eisenstein, J. P., Pfeiffer, L. N., and West, K. W. *Phys. Rev. Lett.* **80**, 1714 (1998).

[51] Feng, X. G., Zelakiewicz, S., Noh, H., Ragucci, T. J., Gramila, T. J., Pfeiffer, L. N., and West, K. W. *Phys. Rev. Lett.* **81**, 3219 (1998).

[52] Lok, J. G. S., Kraus, S., Pohlt, M., Dietsche, W., von Klitzing, K., Wegscheider, W., and Bichler, M. *Phys. Rev. B* **63**, 041305 (2001).

[53] Gornyi, I. V., Mirlin, A. D., and von Oppen, F. *Phys. Rev. B* **70**, 245302 (2004).

[54] Bistritzer, R. and Stern, A. *Phys. Rev. Lett.* **96**, 226801 (2006).

3

Semiconductor Growth by MBE and Scattering in Shallow 2DEGs

In the following chapter, I present our efforts towards the fabrication and the characterization of doped shallow 2DEGs. The development of shallow 2DEGs is linked to the development of nanostructures and of imaging tools such as AFMs and STMs. From an imaging point of view, shallower structures are desirable as they allow easier access to the 2DEG, make it easier to sense what is going on in the 2DEG and yield a stronger signal-to-noise ratio. From a nanostructure point of view, having remote split gates (typically ~ 200 nm away from the 2DEG in high mobility modulation-doped GaAs/AlGaAs heterostructures) induces an unavoidable shadowing effect, as depicted in figure 3.1. This shadowing effect causes the confinement potential to be less abrupt and limits the effective size of the nanostructures patterned on 2DEGs.

A first step towards this goal is to remove the doping layer and grow undoped heterostructures. Such structures can be shallower than doped structures while retaining a high mobility since there is no need to spatially separate the 2DEG from the dopants, as previously demonstrated experimentally [1–9].

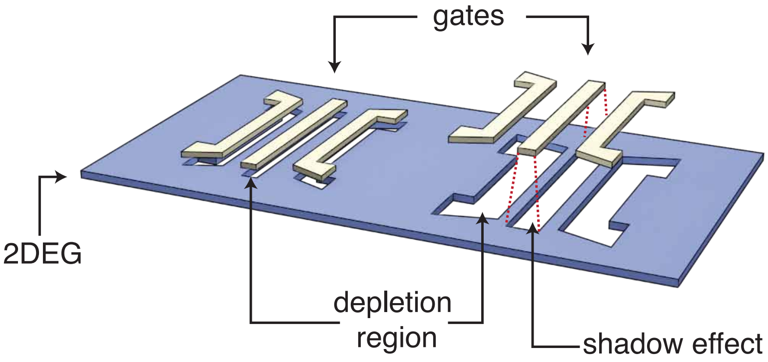

Fig. 3.1: Schematic of the shadowing effect occurring in gated 2DEGs. The actual size of the depleted region is always larger than the lithographic size of the gates, and ultimately limits the size and the sharpness of gated nanostructures. The shadowing effect is larger for gates farther away from the 2DEG.

The drawback of this approach, however, is that undoped structures usually require more complicated processing, often needing an additional accumulation gate (to populate the 2DEG with charge carriers) and the use of overlap or self-aligned contacts [2]. These additional processing steps make the fabrication of undoped nanostructures significantly harder to realize. Therefore, it would be desirable to fabricate *doped* shallow 2DEGs that can still retain a relatively high mobility despite the presence of dopants. Towards this goal, over a hundred GaAs/AlGaAs heterostructures were grown by Dr. John Reno through MBE, and electrically characterized to optimize the mobility of doped shallow 2DEGs. Throughout this optimization process, devices as shallow as 60 nm with a mobility in excess of $\sim 1 \times 10^5$ cm^2/ V $\cdot$ s were produced. It was also determined that, for devices that are 160 nm deep or shallower, scattering off the dopants is significantly limiting the 2DEG mobility and is indeed the dominant scattering mechanism for devices 130 nm deep and shallower.

3.1 MBE Growth of 2DEGs and Initial Characterization

3.1.1 MBE Growth

Molecular Beam Epitaxy (MBE) is the technique of choice to grow the shallow 2DEGs used in this experiment owing to the great level of control it provides over most of the heterostructure parameters. These include the dopant layers number, their position and their concentration. The MBE process involves a slow and careful growth of crystalline heterostructures, one atomically thin epitaxial layer at the time. The growth occurs in the evaporation chamber of the MBE system. This chamber is surrounded by several Knudsen effusion cells where ultra pure materials (Gallium, Arsenite, Aluminium and Silicon are required for the growth of the modulation-doped GaAs/AlGaAs heterostructures) are stored inside heat resistant crucibles to prevent contamination by partial evaporation when the materials are heated and evaporated onto the substrate.

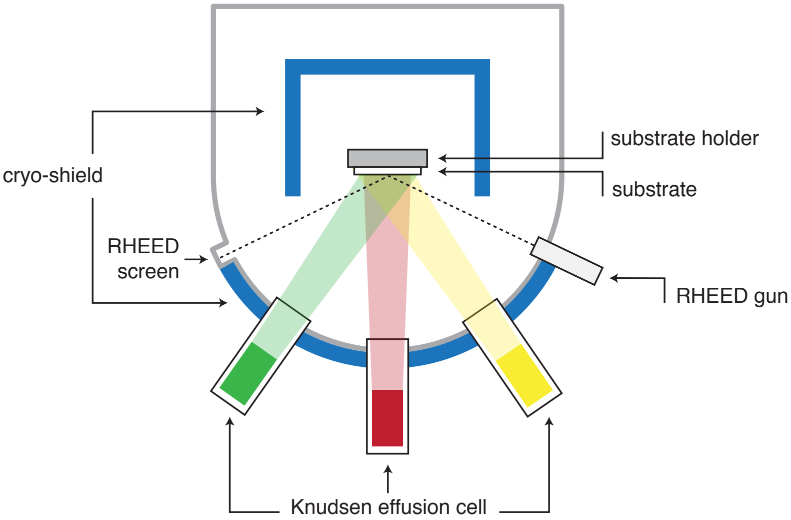

Fig. 3.2: Schematic of the deposition chamber of a MBE system [10].

The material growth is extremely slow, with a growth rate of about 1 μm per hour, ensuring an epitaxial and non-amorphous growth. The growth is carefully monitored using reflection high-energy electron diffraction so that the thickness of each section of the heterostructure can be adjusted through the use of computer-controlled shutters in front of each effusion cell. Owing to the slow growth rate, the process must occur in ultra-high vacuum (at a pressure typically lower than 10^{-11} torr) and on carefully prepared substrate in order to optimize the purity and the crystalline form of the final product. To ensure that the reaction and the material growth primarily occur on the substrate, and not on the chamber walls, the growth chamber is surrounded by shrouds maintained at liquid nitrogen temperature, 77 K. A schematic of such an MBE growth chamber is shown in figure 3.2.

3.1.2 Optimization and Characterization

The growth process for deep samples (*i.e.* samples with a 198 nm separation between the surface of the heterostructure and the middle of the quantum well) had previously been optimized for high 2DEG mobilities. A typical growth sheet for such a structure is shown in figure 3.3, and a schematic of a generic 2DEG heterostructure is also shown in figure 3.4.

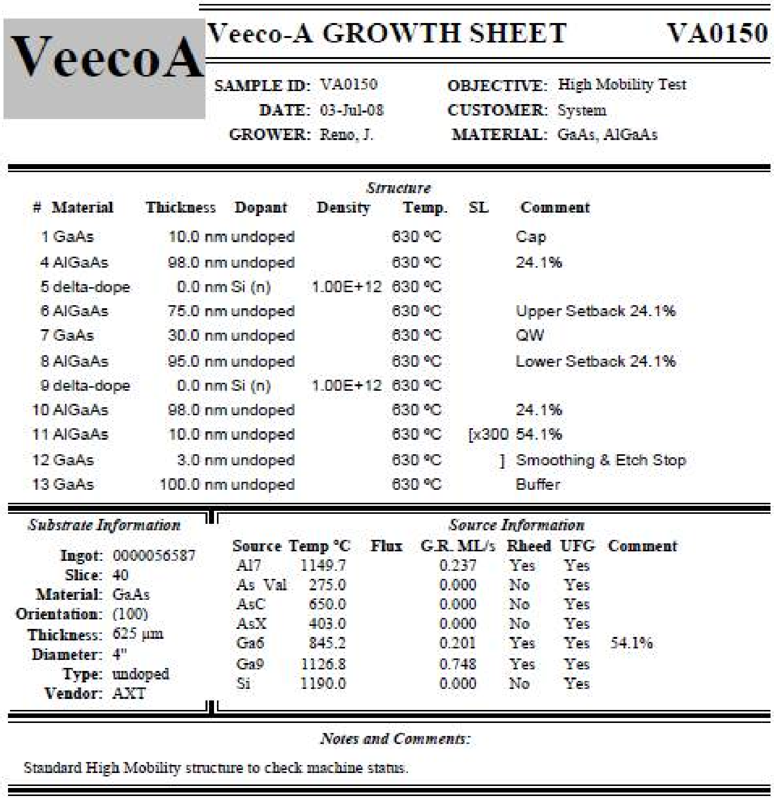

VeecoA

Veeco-A GROWTH SHEET **VA0150**

SAMPLE ID: VA0150
DATE: 03-Jul-08
GROWER: Reno, J.

OBJECTIVE: High Mobility Test
CUSTOMER: System
MATERIAL: GaAs, AlGaAs

Structure

#	Material	Thickness	Dopant	Density	Temp.	SL	Comment
1	GaAs	10.0 nm	undoped		630 °C		Cap
4	AlGaAs	98.0 nm	undoped		630 °C		24.1%
5	delta-dope	0.0 nm	Si (n)	1.00E+12	630 °C		
6	AlGaAs	75.0 nm	undoped		630 °C		Upper Setback 24.1%
7	GaAs	30.0 nm	undoped		630 °C		QW
8	AlGaAs	95.0 nm	undoped		630 °C		Lower Setback 24.1%
9	delta-dope	0.0 nm	Si (n)	1.00E+12	630 °C		
10	AlGaAs	98.0 nm	undoped		630 °C		24.1%
11	AlGaAs	10.0 nm	undoped		630 °C	[x300	54.1%
12	GaAs	3.0 nm	undoped		630 °C	]	Smoothing & Etch Stop
13	GaAs	100.0 nm	undoped		630 °C		Buffer

Substrate Information

Ingot: 0000056587
Slice: 40
Material: GaAs
Orientation: (100)
Thickness: 625 μm
Diameter: 4"
Type: undoped
Vendor: AXT

Source Information

Source	Temp °C	Flux	G.R. ML/s	Rheed	UFG	Comment
Al7	1149.7		0.237	Yes	Yes	
As Val	275.0		0.000	No	Yes	
AsC	650.0		0.000	No	Yes	
AsX	403.0		0.000	No	Yes	
Ga6	845.2		0.201	Yes	Yes	54.1%
Ga9	1126.8		0.748	Yes	Yes	
Si	1190.0		0.000	No	Yes	

Notes and Comments:

Standard High Mobility structure to check machine status.

Fig. 3.3: Typical growth sheet of a GaAs/AlGaAs heterostructure; wafer VA0150 in this case. The heterostructure was grown by Dr. John Reno from the Center for Integrated Nanotechnologies (CINT) at Sandia National Laboratories.

Using this structure as a starting point, over a hundred wafers were grown while varying the depth, the number of doping layers, the dopants concentration n_δ (which is not necessarily the same for each layer), as well as their distance from the quantum well d_i in order to fabricate increasingly shallower 2DEGs with an optimized mobility for a (roughly) constant mobility (see figure 3.4). However, due to the difficulty to populate the 2DEG with electrons in shallow devices (as a large portion of the dopant's electrons get trapped in surface states), the doping level had to be strongly enhanced for shallower 2DEGs and 4 doping layers were used. This resulted in ungated electronic densities varying between 1.5×10^{11} cm^{-2} and 3.5×10^{11} cm^{-2} for the wafers used in this work.

For each MBE wafer grown, a $\sim$ 6 mm × 6 mm square piece was cleaved and cleaned with solvents. Following this, eight small pieces of an $\mathrm{I}_{0.49}\mathrm{Sn}_{0.51}$ alloy were deposited on the samples in a van der Pauw geometry, as shown in figure 3.5. The sample was then annealed in a rapid thermal annealer (RTA) at 420 degree Celsius for 60 seconds.[1] The sample was then mounted in a Janis supertran cryostat and cooled down to 4.0 K[2] inside a GMW model 3474 electromagnet with a maximum field of 0.172 T. The goal at this point was to efficiently determine the density and the mobility of the structures in order to optimize the growth parameters of the shallow 2DEGs. The Hall effect was used to determine the sample's electronic density. This is because the Hall effect occurs in conductors in the presence of a magnetic field as a consequence of the Lorentz force pushing the electrons in a direction perpendicular to the

---

[1] For more details on the annealing process, please consult appendix A.

[2] This is the boiling temperature of liquid helium at saturated vapor pressure at an altitude of $\sim$ 1600 m over sea level.

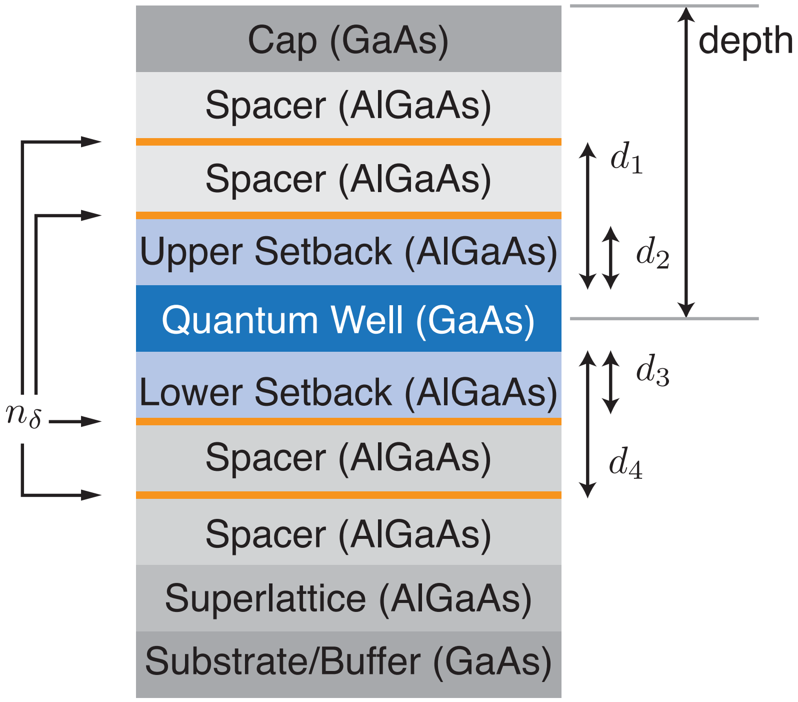

Fig. 3.4: Schematic of a generic modulation-doped GaAs/AlGaAs heterostructure, with the doping layers shown as orange lines. The depth of the 2DEG is measured from the top of the heterostructure to the middle of the quantum well. The density of the dopants is n_δ, and d_i denotes the distance between the i^{th} doping layer and the closest interface of the quantum well.

current. When this happens, an electrostatic force develops across the device to balance this Lorentz force,

$$V_{Hall} = \frac{IB}{n_e}, \tag{3.1}$$

where B is the magnetic field, I is the current and V_{Hall} is the Hall voltage developing across the device. Thus, when measuring the slope of the Hall voltage versus the magnetic field, it is possible to extract the electronic density. The Hall measurements were performed between 0 and 0.172 T with a SR 830 lock-in amplifier set at a frequency of 13 Hz. The current was sourced from the lock-in attached in series with a 10 MΩ resistor and the voltage was measured according to the schematic presented in figure 3.5.

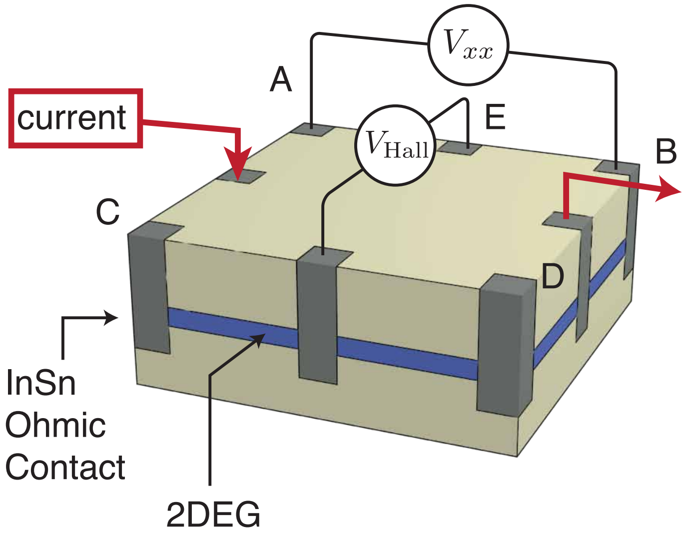

Fig. 3.5: Schematic of a typical 2DEG in the van der Pauw geometry showing the required current and voltage configurations for both Hall and R_{xx} measurements. In a Hall measurement, the voltage is measured perpendicularly to the current flow while it is in a parallel configuration in a R_{xx} measurement.

The resistivity of the sample was determined using the van der Pauw method [11]. This technique offers the advantage that it can be used on samples of any shape for as long as the ohmic contacts are small and located on the edge of the sample. It also requires the sample thickness to be homogeneous, and the sample to be simply connected; that is that there is no hole in the sample. Under these conditions, the resistivity of a two-dimensional system can be calculated by solving the equation

$$e^{-\frac{\pi R_{AB,CD}}{\rho}} + e^{-\frac{\pi R_{BC,AD}}{\rho}} = 1. \tag{3.2}$$

Here, ρ is the 2DEG resistivity in $\Omega/\Box$ and $R_{AB,CD}$ is defined as

$$R_{AB,CD} = \frac{V_B - V_A}{I_{CD}}, \tag{3.3}$$

where $(V_B - V_A)$ is the voltage difference between contacts A and B as depicted in figure 3.5 and I_{CD} is the current sourced between contacts C and D. Solving this equation numerically, the resistivity can be written as

$$\rho = \frac{\pi}{ln(2)} \frac{R_{AB,CD} + R_{BC,AD}}{2} \times f(\frac{R_{AB,CD}}{R_{BC,AD}}), \tag{3.4}$$

where $f(\frac{R_{AB,CD}}{R_{BC,AD}})$ is a function ranging between 0 and 1 (being 1 if $R_{AB,CD} = R_{BC,AD}$) that is determined numerically, as shown in figure 3.6. Using these two measurements, it is possible to determine the sample mobility using equation 2.1, and hence characterize the various wafers to optimize the growth parameters for shallow 2DEGs.

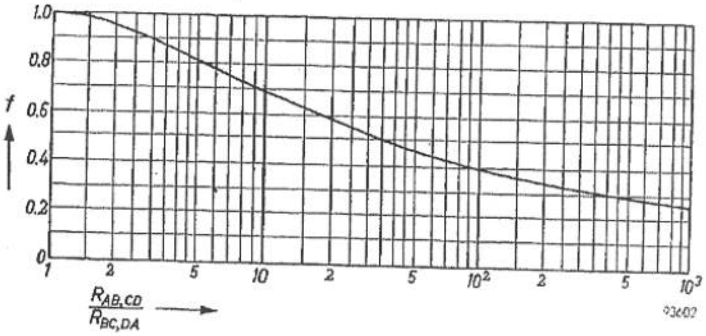

Fig. 3.6: Numerical value of the function f in the van der Pauw equation (equation 3.4). The function has a value of 1 for $R_{AB,CD} = R_{BC,AD}$ and goes towards 0 for large difference between $R_{AB,CD}$ and $R_{BC,AD}$. Figure taken from L. J. van der Pauw [11].

3.2 Device Fabrication and Measurement Technique

Following the optimization process, the highest mobility heterostructures of various depth were selected to perform a scattering mechanism analysis. The selected heterostructures are presented in table 3.1, along with their mobility, as measured in the van der Pawn geometry.

Table 3.1 Heterostructures Used in the Scattering Mechanism Analysis

Sample	Depth	n_δ	d_1	d_2	d_3	d_4	mobility
VA0150	198 nm	1×10^{12} cm^{-2}	—	75 nm	95 nm	—	2.1×10^6 cm$^2/V \cdot s$
VA0123	160 nm	8×10^{11} cm^{-2}	—	75 nm	75 nm	—	5.9×10^5 cm$^2/V \cdot s$
VA0135	130 nm	1×10^{12} cm^{-2}	85 nm	65 nm	65 nm	—	8.6×10^5 cm$^2/V \cdot s$
VA0142	100 nm	2×10^{12} cm^{-2}	65 nm	55 nm	55 nm	65 nm	1.0×10^6 cm$^2/V \cdot s$
VA0153	100 nm	2×10^{12} cm^{-2}	65 nm	55 nm	75 nm	85 nm	1.0×10^6 cm$^2/V \cdot s$
VA0161	80 nm	2×10^{12} cm^{-2}	52 nm	45 nm	45 nm	55 nm	5.9×10^4 cm$^2/V \cdot s$
VA0164	80 nm	2×10^{12} cm^{-2}	50 nm	42 nm	62 nm	72 nm	2.1×10^5 cm$^2/V \cdot s$
VA0222	60 nm	3×10^{12} cm^{-2}	34 nm	28 nm	48 nm	58 nm	2.8×10^5 cm$^2/V \cdot s$

To measure the mobility as a function of density in these structures, a Hall bar pattern with a top gate was defined on the heterostructures. The Hall bar was fabricated using photolithography and a phosphoric etch (see appendix A for more details). After this, Ge/Au/Ni/Au ohmic contacts (260 Å/ 540 Å/ 140 Å/ 1500 Å) were deposited on the Hall bar using e-beam evaporation and annealed using the procedure previously presented. Finally, a thin Ti/Au (50 Å/ 100 Å) top gate was deposited over the Hall bar, once again through e-beam evaporation. The patterns for the ohmic contacts and the e-beam evaporation were achieved using photolithography, as described in appendix A. The top gate was made as thin as possible to allow the possibility to let through red LED light, although this option was not used in the end. The final result of this processing is presented in figure 3.7.

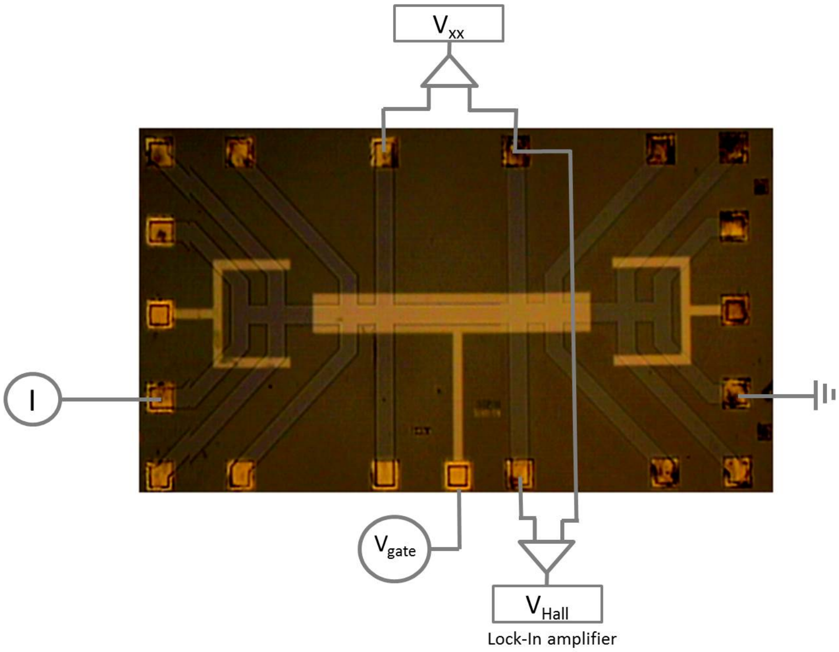

Fig. 3.7: Picture showing a typical gated Hall bar used in the scattering mechanism analysis. In addition, the electrical diagram for both a R_{xx} and a Hall measurement is shown. The separation between the two contacts used for the R_{xx} measurement corresponds to eight squares.

To perform the scattering mechanism analysis, the device's electronic density was varied by sweeping the voltage applied to the top gate. Both positive and negative voltages were applied so as to lower and raise the 2DEG density, respectively. The same technique as presented in section 3.1.2 was used to determine the gated electronic densities. The resistivity of the Hall bar devices was simply measured by dividing the longitudinal resistance $R_{xx} = V_{xx}/I$ by the number of squares (8).

3.3 Experimental Results and Discussion

3.3.1 Consistency Tests

Before measuring the scattering mechanism in shallow 2DEGs, the first step is to verify that the structures have no parallel conduction, *i.e.* there is no accidental secondary 2DEG formed inside the heterostructures. This was first verified numerically by performing an iterative self-consistent Schrödinger-Poisson simulation.

This simulation starts with an initial estimate of the band structure and the electric fields inside the structure. From this estimate, the electron density inside the structure is determined by solving the Schrödinger equation. Then, using the Poisson equation, the new electric fields and band structure are determined. This process is iterated until the electronic density varies less than a threshold value, in our case set to 1×10^{-5} m^{-2}. The boundary conditions are the Fermi energy pinned at mid-gap at the surface (cap) and the electric field being zero at the bottom of the heterostructure (superlattice). From this simulation, it is found that electrons solely collect in the quantum well and not in any of the doping layers, nor at any other location, for all the selected heterostructures.

The absence of parallel conduction was also verified experimentally by measuring the longitudinal (R_{xx}) and the Hall resistances for all our heterostructures at T = 330 mK in a helium-3 refrigerator. If parallel conduction was to be present, multiple 2DEGs would exist in the structures, each having a different electronic density. One would then expect the minima in the Shubnikov de-Haas oscillations to not reach zero resistance, but rather saturate at a positive value of resistance. This is because the zero-resistance occurs at a different magnetic field in the quantum well than in the parasitic layer. In addition, parallel conduction would make it impossible to linearly extract a single density from the value of the magnetic field at which the filling fractions occur. Finally, the low-magnetic field Hall resistance would not be linear in a structure with parallel conduction.

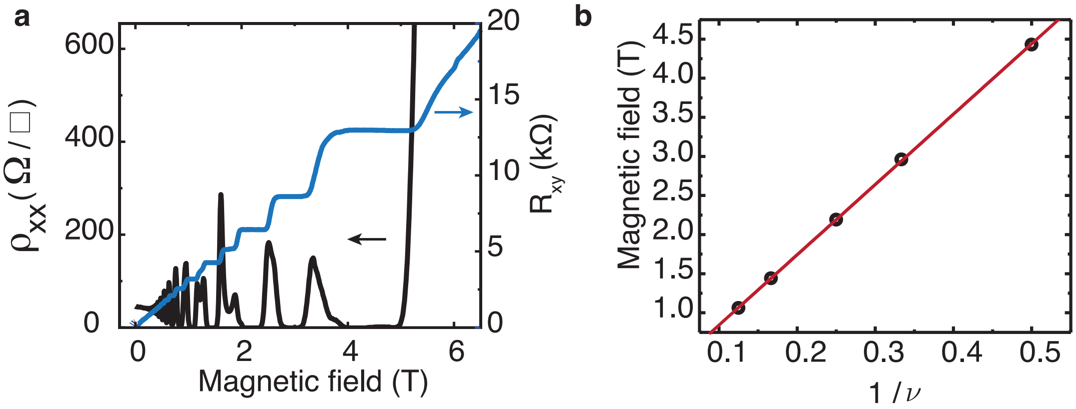

Fig. 3.8: **(a)** ρ_{xx} (black curve, left axis) and R_{Hall} (blue curve, right axis) for a typical device (from wafer VA0142 in this case) showing no evidence of parallel conduction. This can be seen from the linearity of the low magnetic field Hall trace and from the ρ_{xx} minima reaching a zero resistance (within 0.2 % of the lock-in amplifier full scale). These data were taken at a temperature of $\sim$ 330 mK. **(b)** Linear fit of the inverse filling fraction as a function of the magnetic field. The linearity of the data shows that only one density is present in the device. Using this fit and equation 2.19, an electronic density of 2.2×10^{11} cm^{-2} is determined.

Figure 3.8 shows the results of such measurements for a device made from wafer VA0142. Importantly, every device used in this analysis showed the same qualitative features. The measurements are fully consistent with our structures being free of parallel conduction since the Hall resistance is linear with magnetic field until the quantum Hall effect develops. When this is the case, the longitudinal resistance minima reach zero resistance and the dependence of the inverse filling fraction on the magnetic field is linear, as described by equation 2.19. These measurements, combined with the results from the Schrödinger-Poisson simulation, bring us confidence that the heterostructures studied here are entirely free of parallel conduction.

Another telltale sign for the proper working of the device is the electronic density varying linearly with gate voltage. This is true as long as the gate voltage is not sufficiently negative such that the 2DEG reaches the insulating regime at low density as well as not sufficiently positive such that the electrons have enough energy to escape the first energy subband of the 2DEG. All the measurements presented here are realized in the regime where the electronic density varies linearly with gate voltage. This behavior was observed in all heterostructures, and an example measured in device VA0135 is shown in figure 3.9.

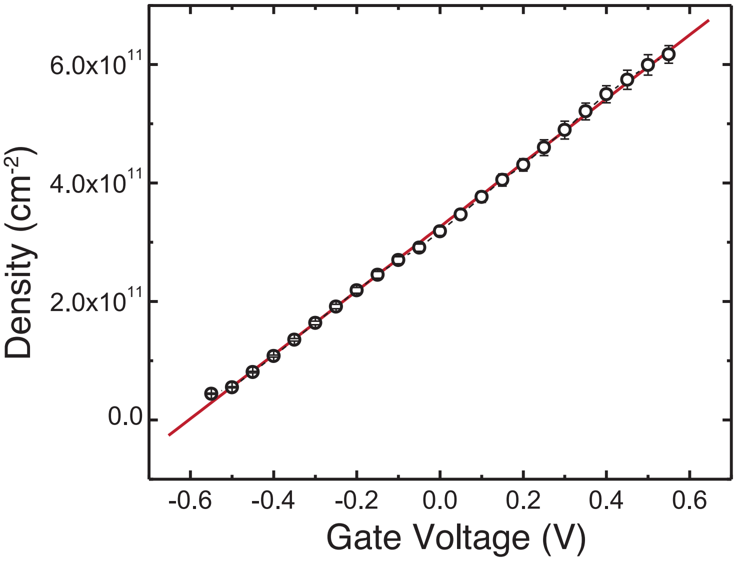

Fig. 3.9: Plot showing the typical dependence of the electronic density as a function of gate voltage (device VA0135 in this case). The red line is a linear fit to the data.

3.3.2 Mobility Versus Density Analysis

From these devices, it is possible to determine the electronic density dependence of the mobility and to extract the power-law exponent α for this dependence, as defined in equation 2.13. This data is presented in figure 3.10 for selected heterostructures. It is worth noting that, as the structures are made shallower and hence the dopants are located closer to the 2DEG, the overall mobility of the heterostructures decreases for a fixed density, suggesting that the dopants have indeed a strong influence on the mobility of the 2DEG in shallow structures.

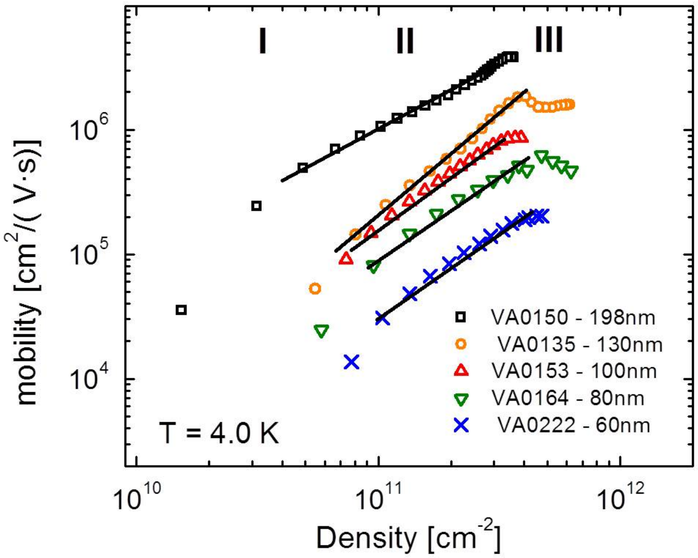

Fig. 3.10: Log-log plot of the mobility versus the electronic density for selected heterostructures. The intermediate density regime is denoted by region II, where the devices are neither in the insulating regime (region I) nor in the regime where the 2DEG second subband is populated (region III). The black lines are guide-to-the-eyes in the region where the mobility dependence on the density is a power-law.

From this figure, three density regimes are identified and labeled I through III. The regime of interest here is the intermediate density regime located in region II where, as observed previously, the mobility varies with the electron density in a power-law fashion. At the lowest electronic density, in region I, the mobility decreases more rapidly with decreasing density than in region II. This low density regime is dominated by fluctuation-induced density inhomogeneities eventually leading to a percolation localization transition to an insulating phase [12] at a critical density $n_c \lesssim 5 \times 10^{10}$ cm^{-2} (for our devices). Region III, the highest electronic density regime, is characterized by a mobility drop with increasing density. This is a consequence of inter-subband scattering due to the population of the second energy subband of the quantum well, as described in section 2.2.1. Another experimental hint of a second subband population is the onset of an oscillation in the minima's resistance of R_{xx} [13]. Such a measurement was performed in device VA0135, as shown in figure 3.11.

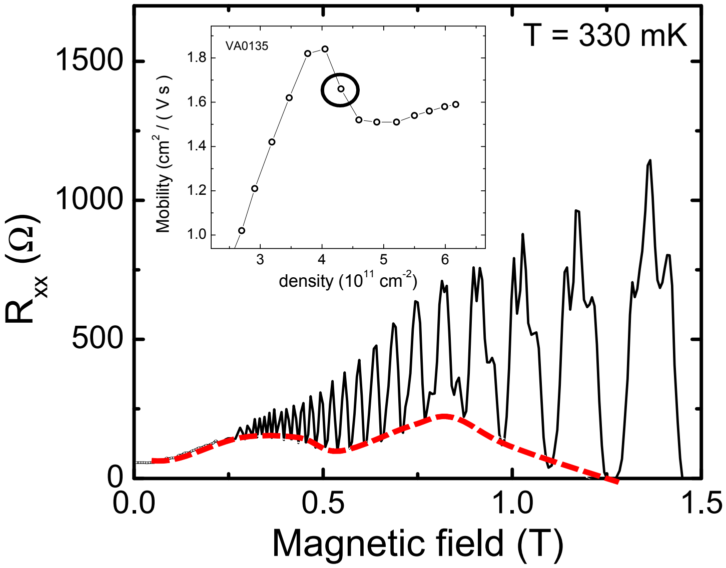

Fig. 3.11: R_{xx} as a function of magnetic field for device VA0135. The oscillation in the minima of the resistance, outlined in red, is consistent with the second energy subband of the quantum well being populated. The inset shows the mobility versus density curve of this device, and the region where the Shubnikov-De Hass trace was taken is shown by a circle.

Focusing on the intermediate density regime where the mobility is a power-law function of the electronic density, the exponent α was extracted for each device. We separated the data for the case where the doping is symmetric and asymmetric, although no significant difference was observed between both cases. Here, the symmetry/asymmetry of the structure refers to the distance between the quantum well and the top and bottom doping layers. These results are shown in figure 3.12. The power-law exponents α are extracted from at least two different devices fabricated from the same heterostructure (wafer), and it was verified that the exponent values were within each other's experimental error. This error is determined by expanding and shrinking the boundaries of region II to obtain a maximal and a minimal value on α during the fitting procedure.

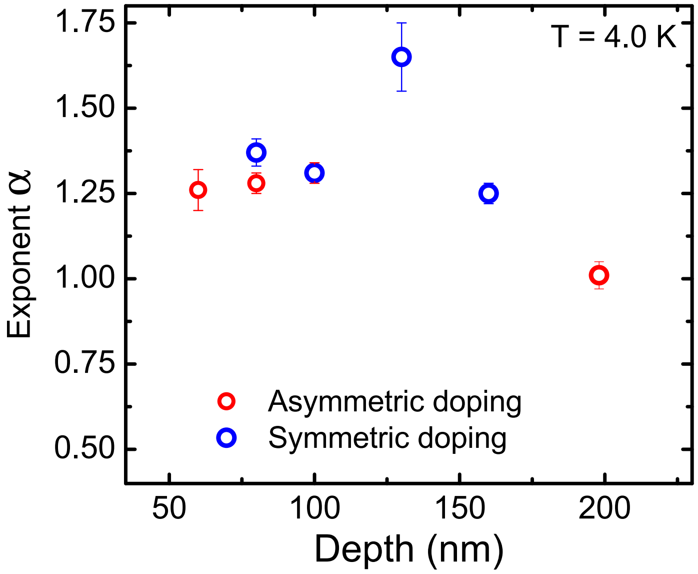

.

Fig. 3.12: Power-law exponent α versus the quantum-well depth for symmetrically-doped (blue open circles) and asymmetrically-doped (red open circles) heterostructures. All the heterostructures used to acquire this data are presented in table 3.1

As mentioned in section 2.2.1, the dominant scattering mechanism in our

GaAs heterostructures is expected to be arising from charged impurities, both intentional (dopants) and unintentional. For the heterostructure with the deepest 2DEG (VA0150), one can expect unintentional charged impurities, or background impurity scattering, to be the main source of disorder since the remote dopants are presumably contributing little to the resistivity (the delta doping layers being farther from the 2DEG). This expectation is in agreement with our experimental results where an exponent $\alpha \simeq 1$ is observed, as predicted theoretically in the case of background impurity scattering [14]. This is also consistent with this deep structure having the highest mobility since scattering off the dopants has little impact on the 2DEG mobility.

Since the ionized impurity background is not expected to change from heterostructure to heterostructure, scattering off unintentional charged impurities is unlikely to explain the general mobility decrease as the 2DEGs depth becomes shallower. However, one parameter that does change as the 2DEG is brought closer to the surface is the separation between the modulation doping layers and the 2DEG. Theoretically, scattering off unscreened remote ionized impurities should yield an exponent $\alpha = 1.5$, which is approximately reached for device VA0135, from a wafer with a 2DEG 130 nm deep ($\alpha = 1.65 \pm 0.1$). The intermediate value of $\alpha = 1.25 \pm 0.03$ obtained in device VA0160 might be explained by comparable contributions to scattering arising from both intentional and unintentional charged impurities. For samples shallower than 130 nm, the exponent reaches a value of $\alpha \simeq 1.3$. This decrease in the exponent value while the contribution to scattering from remote ionized impurities is expected to become stronger (and while the overall mobility decreases) can be explained by the following reasoning : as the dopants are moved closer to the 2DEG, the screening should become more effective. This increase in the screening strength should lower the value of the exponent α towards the fully screened value of $\alpha = 1$, as predicted theoretically and as confirmed by a detailed modeling performed by Sankar Das Sarma [14].

In summary, we have found that scattering off intentional remote ionized impurities is strongly affecting the mobility of shallow heterostructures and is significant for 2DEGs 160 nm deep and shallower. Despite this limitation, a mobility of $\sim 2 \times 10^5$ cm^2/ V $\cdot$ s is still achievable in 2DEGs as shallow as 60 nm. While being roughly two orders of magnitude lower than the highest mobility achieved GaAs/AlGaAs heterostructures, retaining this high mobility in doped shallow heterostructures is important. Indeed, due to the shadowing effect, shallow heterostructures will eventually be required to pattern the smallest nanostructures on 2DEGs. Furthermore, extremely high mobility is not always an important issue in nanostructure fabrication, as the involved fabrication process often degrades the mobility of the cleanest structures anyhow. While such shallow heterostructures have not been used to fabricate the one-dimensional Coulomb drag devices presented in this thesis, the growth of doped shallow structures of high quality is essential to the future development of 2DEG based nanoelectronics.

References

[1] Frost, J. E. F., Ritchie, D. A., and Jones, G. A. C. *J. Cryst. Growth* **111**, 305 (1991).

[2] Kane, B. E., Pfeiffer, L. N., West, K. W., and Harnett, C. K. *Appl. Phys. Lett.* **63**, 2132 (1993).

[3] Kane, B. E., Pfeiffer, L. N., and West, K. W. *Appl. Phys. Lett.* **67**, 1262 (1995).

[4] Holland, M. C., Skuras, E., Davies, J. H., Larkin, I. A., Long, A. R., and Stanley, C. R. *J. Cryst. Growth* **150**, 1215 (1995).

[5] Herfort, J. and Hirayama, Y. *Appl. Phys. Lett.* **69**, 3360 (1996).

[6] Kawaharazuka, A., Saku, T., Hirayama, Y., and Horikoshi, Y. *J. Appl. Phys.* **87**, 952 (2000).

[7] Kawaharazuka, A., Saku, T., Kikuchi, C. A., Horikoshi, Y., and Hirayama, Y. *Physica E* **13**, 663 (2002).

[8] Lilly, M. P., Reno, J. L., Simmons, J. A., Spielman, I. B., Eisenstein, J. P., Pfeiffer, L. N., West, K. W., Hwang, E. H., and Das Sarma, S. *Phys. Rev. Lett.* **90**, 056806 (2003).

[9] Das Gupta, K., Croxall, A. F., Mak, W. Y., Beere, H. E., Nicoll, C. A., Farrer, I., Sfigakis, F., and Ritchie, D. A. *Semicond. Sci. Technol.* **27**, 115006 (2012).

[10] Ottesen, V. Figure under a Creative Commons Attribution-Share Alike license.

[11] van der Pauw, L. J. *Philips. Tech. Rev.* **20**, 220 (1958).

[12] Manfra, M. J., Hwang, E. H., Das Sarma, S., Pfeiffer, L. N., West, K. W., and Sergent, A. M. *Phys. Rev. Lett.* **99**, 236402 (2007).

[13] Störmer, H. L., Gossard, A. C., and Wiegmann, W. *Solid State Commun.* **41**, 707 (1982).

[14] Hwang, E. H. and Das Sarma, S. *Phys. Rev. B* **77**, 235437 (2008).

4

Review of One-Dimensional Quantum Transport and 1D-1D Coulomb Drag

In this chapter, I present a review of the theoretical framework to one-dimensional transport along with some of the key experimental achievements realized in one-dimensional semiconducting systems. The overarching goal of this chapter is to provide the theoretical and experimental background necessary to understand the physics behind one-dimensional Coulomb drag. Towards this effort, I first present the Landauer-Büttiker formalism describing the conductance of interactionless quasi one-dimensional systems. Following this, the Luttinger liquid model, which is believed to describe the physics taking place in one-dimensional systems and to replace the Fermi liquid model valid in higher dimensions, is presented. Then, a brief review of the main theoretical models for one-dimensional Coulomb drag are presented, with an emphasis on their predictions regarding the temperature dependence of the drag signal. Finally, pioneering experiments realized in single and coupled gate-induced one-dimensional systems are presented, with a strong emphasis on the current state of affairs in experimental 1D Coulomb drag.

4.1 Theory of Ballistic Quantum Transport

4.1.1 Landauer-Büttiker formalism

Since the main subject of this thesis is to measure Coulomb drag in one-dimensional quantum wires, the conductance of a one-dimensional fermionic systems is of great interest. One of the simplest way to calculate this quantity is to consider transmission across a narrow channel connecting two Fermi-liquid reservoirs where the Pauli exclusion principle is the only form of electron-electron interaction that is considered.

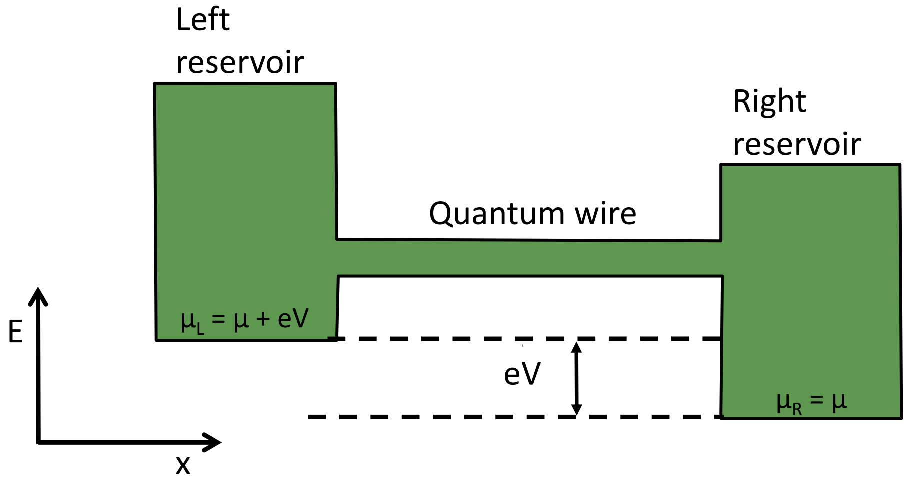

Fig. 4.1: Schematic of a quantum wire connected to two Fermi-liquid reservoirs. A difference in the chemical potential between the left and right reservoirs arises when a voltage V is applied across the quantum wire.

The basic picture of such a quantum wire connecting two Fermi-liquid reservoirs is presented in figure 4.1. To calculate the conductance across this system, one can consider contributions from the current going from the left reservoir to the right reservoir and from the current going in the other direction. These quantities are simply given by,

$$I_{R\to L} = \frac{2e}{2\pi}\sum_{\lambda}\int_0^{\infty} T_{R\to L}(k_x)v_L(k_x)f_F^L(k_x,\lambda)dk_x, \tag{4.1}$$

$$I_{L\to R} = \frac{2e}{2\pi}\sum_{\lambda}\int_0^{\infty} T_{L\to R}(k_x)v_R(k_x)f_F^R(k_x,\lambda)dk_x, \tag{4.2}$$

where λ refers to the transverse quantum number due to the quantization in the y-direction, $f_F^{L,R}$ is the fermi distribution function (equation 2.7), $v_{L,R}(k_x)$ is the electrons velocity in the wire's direction, $T(k_x)$ is the transmission probability across the wire and the factor of two accounts for the spin degeneracy of the system [1]. The total current is given by the difference between left-moving and right-moving electrons, $I = I_{R\to L} - I_{L\to R}$. Changing the integration variable from wave-vector to energy and taking into account the symmetry of the transmission coefficient, one obtains

$$I = \frac{2e}{h}\sum_{\lambda}\int_{-\infty}^{\infty} T_{\lambda}(\epsilon_x)[f_F^L(k_x,\lambda) - f_F^R(k_x,\lambda)]d\epsilon_x. \tag{4.3}$$

In this equation, ϵ_x is the electron energy. If a bias V is applied over the wire, a difference eV in chemical potential between the left and right reservoirs will occur. At $T = 0$, the Fermi distribution function can be rewritten as a δ function and then the total current becomes

$$I = \frac{2e}{h} \sum_{\lambda} \int_{-\infty}^{\infty} T_{\lambda}(\epsilon_x)[\delta(\mu + eV - \epsilon_x - \epsilon\lambda) - \delta(\mu - \epsilon_x - \epsilon\lambda] d\epsilon_x, \tag{4.4}$$

where μ is the chemical potential of the unbiased system. Carrying out the integral, one obtains

$$I = \frac{2e^2}{h} V \sum_{\lambda} T_{\lambda}(\epsilon_x), \tag{4.5}$$

and the conductance G thus becomes

$$G = \frac{I}{V} = \frac{2e^2}{h} \sum_{\lambda} T_{\lambda}(\epsilon_x), \tag{4.6}$$

which is known as the Landauer-Büttiker formula [1]. In the case of ballistic transport, the transmission across the wire is unhindered and therefore $\sum_{\lambda} T_{\lambda}(\epsilon_x) = N$ where N is the number of quantum mechanical channels in the quantum wires, yielding a conductance quantized in units of $2e^2/h$. In the non-ballistic case, $\sum_{\lambda} T_{\lambda}(\epsilon_x) < N$ and the exact quantization of the conductance is lost, although plateau-like features may still appear in the conductance whenever a conduction channel opens up. At finite temperature, the Fermi distribution function effectively broadens and smooths out the sharp features occurring at $T = 0$, as depicted in figure 4.2.

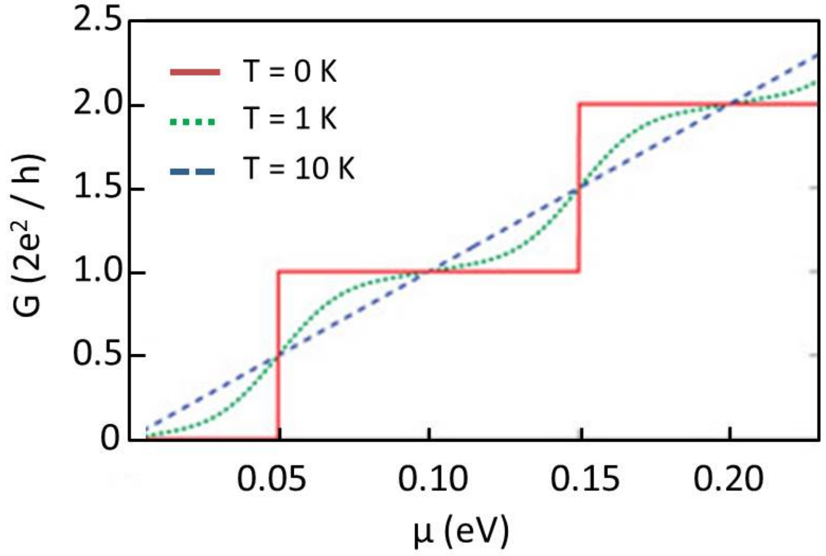

Fig. 4.2: Plot of the temperature broadening of the ideal conductance of a quantum wire by numerically solving equation 4.3. The value of the temperature and of the chemical potential are arbitrary.

The reason why such a simple interactionless transport model actually describes accurately the conductance of one-dimensional systems [2, 3] is that the physical processes giving rise to the wire's resistance take place entirely in the Fermi-liquid reservoirs [4, 5]. However, to understand the physics intrinsic to one-dimensional systems, interactions must be ultimately considered.

4.2 One-Dimensional Quantum Fluids

4.2.1 Failure of Fermi Liquid Theory in One-Dimension

As described in chapter 2, the Fermi liquid model provides a convenient framework for understanding the physics taking place in two- and three-dimensional systems. In such high-dimensional systems (*i.e.* D ≥ 2), particles can move through space without necessarily encountering other particles, as depicted in figure 2.1. However, in one-dimensional systems, such a free motion is not possible anymore as particles will unavoidably collide with one another as they move towards one direction or the other. Therefore, the mean-field quasi-particle formalism used to describe Fermi liquids can no longer be applied in one dimension since only *collective* motion can occur. In a sense, the elements of a one-dimensional system are infinitely correlated and thus the effect of interactions is stronger in one-dimension.

Another issue arising in the Fermi liquid model in one dimension is that perturbation theory cannot be used to determine the effect of interactions. This is best understood by considering correlation functions such as the density-density correlation, for example. This correlation measures the linear response of a fermion (electron) gas when subjected to an external potential. This response is given by the susceptibility of the electron gas,

$$\chi(q) = \frac{1}{V} \sum_k \frac{f_F(\epsilon(k)) - f_F(\epsilon(k+q))}{\epsilon(k) - \epsilon(k+q) + i\delta}, \tag{4.7}$$

where $\delta = 0^+$ is a vanishingly small quantity, V is the volume of the system and $\epsilon(k)$ is the fermion energy [6]. When the particles lie on the Fermi surface (*i.e.* when $|k| = k_F$, see figure 4.3), if there exists a vector Q such that $-\epsilon(k) = \epsilon(k+Q)$, then a singularity occurs in the susceptibility. For systems with more than one dimension, such a nesting property is only satisfied for a limited number of points and these singularities are smoothed out when the susceptibility is integrated over all possible wave vector values.

In one dimension, however, the nesting property is always satisfied close to the Fermi surface since it consists of only 2 points, as depicted in figure 4.3. Indeed, this is a consequence of the inversion property of physical systems and of the linear dispersion of fermions near Fermi points, yielding $\epsilon(k) = -\epsilon(k + 2k_F)$ and satisfying the nesting property. It follows from this that perturbation theory diverges at $Q = 2k_F$ in one-dimension, showing that the original non-interacting ground state is significantly different from the interacting one that perturbation theory is trying to describe.

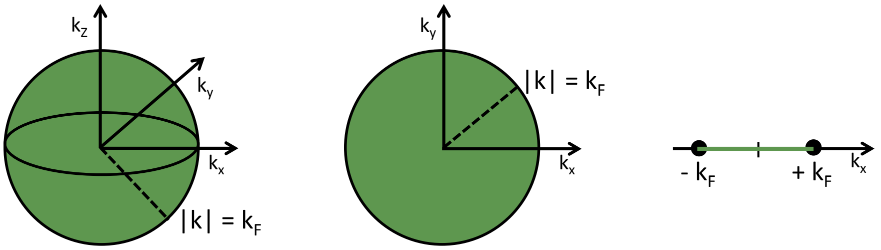

3D 2D 1D

Fig. 4.3: Schematics of the Fermi surface of a 3D, a 2D and a 1D electron gas. In 1D, the Fermi surface consists of only 2 points.

Since, unlike in higher dimensional Fermi liquids, a non-interacting ground state is not a suitable estimate for the interacting ground state in one-dimensional systems, a new model must be used to describe such low-dimensional systems. This can be achieved by considering the basic particle-hole excitations occurring in one-dimension. Particle-hole excitations are created by destroying a particle with momentum k below the Fermi level and creating an excited particle with momentum $k + q$ above it. In high dimensions, there exists a continuum of q values between 0 and $2k_F$ for which it is possible to create low-energy excitations (*i.e.* close to the Fermi energy), due to the freedom in the angle that the wave vector q can take. However, to produce low-energy excitations in one dimension, there are only two values of q available : $q = 0$ and $q = 2k_F$, since the Fermi surface is reduced to only two points and there is no freedom with the angle of the wave vector q. Thus, in contrast to high-dimensional systems, the low-energy and long-lived particle-hole excitations in one-dimensional systems must have a well defined value of both energy and momentum, making these excitations well-defined quasi-particles [6]. Since these excitations are bosonic in nature (being a combination of two fermions), rewriting the fermionic one-dimensional Hamiltonian in terms of bosons is a logical starting point for a model aiming to describe the low-energy physics of one-dimensional electrons.

4.2.2 Tomonaga-Luttinger Liquid Theory

Bosonization

The theoretical technique used to rewrite the Hamiltonian describing a system of fermions (such as electrons) in terms of bosonic operators is called *bosonization*. With this technique, it is possible to build a framework that encompasses most of the simple physics taking place in one-dimensional systems. The model was first brought forth by Tomonaga in 1950 [7] when he proposed that, if the excitation spectrum of a Fermi gas is linear (which is a reasonable approximation for excitations near the Fermi surface, see figure 4.5

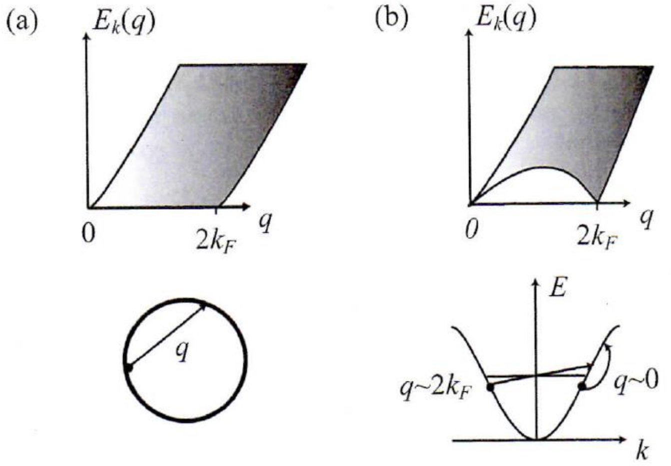

Fig. 4.4: Schematics of phase-space available for electron-hole excitations in **(a)** 2D and **(b)** 1D electron gases. In 1D, the low-energy particle-hole excitations have both a well defined momentum and energy. Figure taken from T. Giamarchi [6].

below), then its Hamiltonian can be rewritten in terms of bosonic fields for long-ranged and weak inter-particle forces. Luttinger later showed in 1963 that the constraints imposed by Tomonaga were superfluous [8], although his solution was later corrected by Mattis and Lieb [9]. Nowadays, this model is called the Tomonaga-Luttinger liquid (TLL) model, or simply the Luttinger liquid (LL) model. For the remainder of this section, the basics of the bosonization technique will be presented.

As mentioned previously, the energy (ϵ) of the particle-hole excitations is linearized and is given by

$$\epsilon(k) = \hbar k v_F, \tag{4.8}$$

where v_F is the Fermi velocity and k is the wave-vector. This linearization of the energy dispersion relation forces two branches of fermions to appear : left-moving ones and right-moving ones, as depicted in figure 4.5. This linear dispersion relation also implies that an infinite number of energy states are occupied below the Fermi energy, suggesting that a cut-off in momentum will be required in some circumstances to make the model well defined. Within this framework, the interactionless Hamiltonian of the system is defined as

$$H = \sum_{k,r=R,L} v_F(rk - k_F) c^\dagger_{r,k} c_{r,k}, \tag{4.9}$$

where c_k ($c^\dagger_k$) is the annihilation (creation) operator for a spinless fermion with wave-vector k and where $r = +1$ for right moving particles and $r = -1$ for left moving ones.

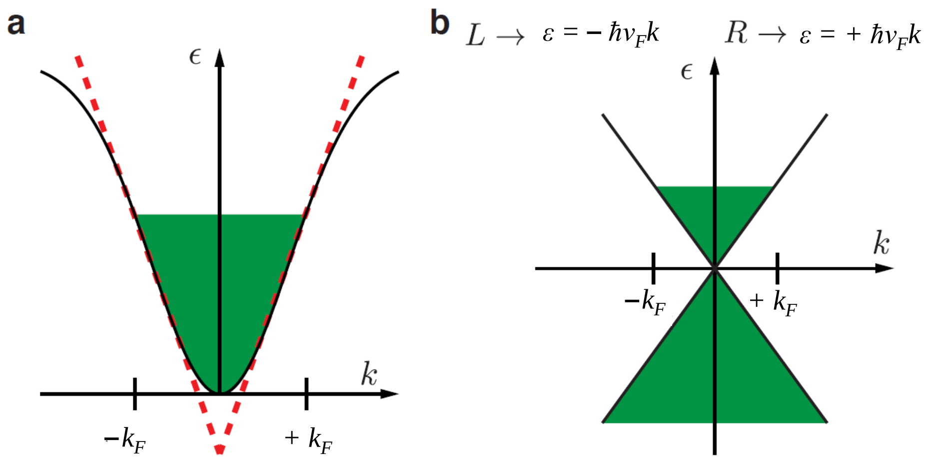

Fig. 4.5: **(a)** Band curvature of one-dimensional fermions. **(b)** Linear approximation to the band curvature of one-dimensional fermions used in the Tomonaga-Luttinger liquid model. An infinite number of states with negative energy are present due to the extension of the spectrum to all values of k. Also, fermions are now divided in two branches, left-moving and right-moving fermions.

Since particle-hole excitations are the basis of choice to describe one-dimensional systems, it is convenient to rewrite the Hamiltonian in terms of density fluctuations. This is because these fluctuations are essentially a superposition of particle-hole excitations, and so an operator creating such density fluctuations can be defined as

$$\rho^\dagger(q) = \sum_k c^\dagger_{k+q} c_k. \tag{4.10}$$

If one is now to consider spin, a pair of creation/annihilation operators should also be included for each spin species. For simplicity, I will present here the results for spinless fermions and will only re-introduce spins later in the section. Since the density fluctuation operator is a combination of two fermionic operators, it is intrinsically bosonic and so it can be written as a linear combination of bosonic operators b_q and $b_q^\dagger$. This intuitive insight can be verified by calculating the commutation relations of the density operators, which follow the same rules as boson operators, up to a normalization factor [6]. The creation and annhilation bosonic operators are then defined in terms of the density fluctuation operators,

$$b_q^\dagger = \left(\frac{2\pi}{L|q|}\right)^{1/2} \sum_r Y(rq)\rho_r^\dagger(q), \tag{4.11}$$

$$b_q = (\frac{2\pi}{L|q|})^{1/2} \sum_r Y(rq)\rho_r^\dagger(-q), \tag{4.12}$$

where L is the length of the system and $Y(x)$ is the standard step-function defined as $Y(x) = 1$ for $x > 0$ and $Y(x) = 0$ for $x < 0$ and assuming that $p \neq 0$. These new bosonic operators and the Hamiltonian of the system (equation 4.9) commute according to

$$[b_{p_0}, H] = v_F p_0 b_{p_0}, \tag{4.13}$$

$$[b_{p_0}^\dagger, H] = v_F p_0 b_{p_0}^\dagger. \tag{4.14}$$

From these commutation relations, it follows that the Hamiltonian in the bosonic basis is given by

$$H \simeq \sum_{p\neq 0} v_F |p| b_p^\dagger b_p. \tag{4.15}$$

Importantly, this Hamiltonian has a kinetic energy that is still quadratic in terms of the bosonic operators. This implies that under the Coulombic interactions, this Hamiltonian will remain quadratic and it will therefore be relatively simple to solve for the interacting Hamiltonian. It is convenient to introduce two bosonic fields to replace the boson operators. These fields are defined as

$$\begin{gathered}\phi(x), \theta(x) = \\ \mp (N_R \pm N_L)\tfrac{\pi x}{L} \mp \tfrac{i\pi}{L} \textstyle\sum_{p\neq 0} \left(\tfrac{L|p|}{2\pi}\right)^{1/2} \tfrac{1}{p} e^{-\beta|p|/2 - ipx}(b_p^\dagger \pm b_{-p}),\end{gathered} \tag{4.16}$$

where β is an arbitrary cutoff and $N_r = \sum_k [c_{r,k}^\dagger c_{r,k} - < 0|c_{r,k}^\dagger c_{r,k}|0 >]$. These fields also satisfy the following commutation relation,

$$[\phi(x_1), \Delta\theta(x_2)] = i\pi\delta(x_2 - x_1), \tag{4.17}$$

implying that the conjugate momentum to the field $\phi(x)$ is simply given by

$$\Pi(x) = \frac{1}{\pi}\Delta\theta(x). \tag{4.18}$$

Using equation 4.15 and equation 4.16, one can rewrite the interactionless Hamiltonian simply as

$$H = \frac{\hbar}{2\pi} \int dx v_F [(\pi \Pi(x))^2 + (\Delta\phi(x))^2]. \tag{4.19}$$

An impressive outcome of this model is that the Hamiltonian conserves a very similar form in the presence of interactions, *i.e.*,

$$H = \frac{\hbar}{2\pi} \int dx [uK(\pi \Pi(x))^2 + (\frac{u}{K}\Delta\phi(x))^2]. \tag{4.20}$$

where all interaction effects are now included into the dimensionless parameter K and the velocity-like parameter u. The physics of interacting one-dimensional fermionic systems can therefore be described by free bosonic excitations and a set of many-body parameters accounting for interaction effects. In addition, if spin is to be considered, one would simply need two types of fermions, spin-up fermions and spin-down fermions, and the new interactionless Hamiltonian simply becomes $H = H_\uparrow + H_\downarrow$. As well, one can introduce charge and spin degrees of freedom and redefine new bosonic fields as

$$\phi_\rho(x) = \frac{1}{\sqrt(2)}[\rho_\uparrow(x) + \rho_\downarrow(x)], \phi_\sigma(x) = \frac{1}{\sqrt(2)}[\rho_\uparrow(x) - \rho_\downarrow(x)], \tag{4.21}$$

where ρ denotes the charge channel, σ denotes the spin channel and $\uparrow, \downarrow$ denote the operators defined earlier for spin up and down fermions, respectively. Similar relations hold for the θ fields as well. Using these new fields, the interacting Hamiltonian in the presence of spin can now be written as

$$H = H_\rho + H_\sigma, \tag{4.22}$$

where H_ρ and H_σ are simply given by equation 4.20 with parameters K_ρ, u_ρ and K_σ, u_σ, respectively. So, when considering electrons with spin, the physics of the interacting system is still described by free bosonic excitations where charge excitations and spin excitations propagate independently from one another. This is know as *spin-charge separation*. Of course, the Tomonoga-Luttinger model described here is only a linear approximation of real physical systems. Nevertheless, Haldane [10] showed that the Hamiltonian obtained through the bosonization technique does describe the low-energy physical properties of any one-dimensional system with massless spin excitations, and the wave-function obtained within this linear approximation is simply the first-harmonic approximation of the full wave-function.

Physical Properties

From this model for interacting one-dimensional fermions, we can now explore different physical properties of one-dimensional systems subject to interactions. For example, within the Fermi liquid theory, the specific heat of a system is linear with temperature and given by

$$C_v = \frac{dE}{dT} = \frac{T}{v_F}\frac{L\pi}{3}. \tag{4.23}$$

Within the Luttinger liquid theory, a similar calculation yields a similar specific heat,

$$C_v = \frac{dE}{dT} = \frac{T}{\frac{1}{2}(u_\rho + u_\sigma)}\frac{L\pi}{3}. \tag{4.24}$$

We can readily see that the specific heat calculated within the Luttinger liquid model is simply the Fermi liquid result renormalized by a factor taking into account the effect of interactions. Similar phenomenon occur when calculating other quantities such as the spin susceptibility, the spin and the charge compressibility and the charge stiffness : the Luttinger liquid model results are Fermi-liquid like with a renormalization factor accounting for interactions.

While some physical properties of Luttinger liquids are Fermi-liquid like, correlations within the Luttinger model are however drastically different from their Fermi-liquid counterparts. This is because correlations usually decay (with interparticle separation) as $1/r^2$ in Fermi liquids whereas Luttinger liquid correlations decay algebraically with interparticle separation, *i.e.* by a power-law with a non-universal exponent, depending on the interactions strength. For example, the density correlation of a Luttinger liquid is given by

$$< \rho(x), \rho(0) > \simeq A_1 + \frac{A_2}{r^2} + A_3 \left(\frac{\beta}{r}\right)^{K_\rho + K_\sigma} + A_4 \left(\frac{\beta}{r}\right)^{4k_\rho} + [...], \tag{4.25}$$

where only the power-law dependence of the correlation function is explicitly presented. Such a power-law dependence with non-universal exponents of the correlation functions is a hallmark of a Luttinger liquid. This dependence also implies that one-dimensional systems are always on the verge of a phase-transition (divergent susceptibility) without ever being able to go through such ordering.

As mentioned previously, a quantity of interest for this thesis is the conductance of a one-dimensional system. Within the Luttinger-liquid framework, this conductance is given by [6]

$$G = \frac{2e^2}{h} K_\rho. \tag{4.26}$$

However, physical one-dimensional systems such as quantum wires are usually connected to Fermi-liquid reservoirs, and so the value of their conductance may also be determined by the properties of the leads. Therefore, rather than being given by the (reduced) Luttinger-liquid result, the conductance of physical quantum wires is actually described by Landauer's formula [1]. Thus, interaction and correlation effects are not apparent in the conductance of a single quantum wire, as experimentally observed by Kouwenhoven's [2] and Pepper's group [3].

The Luttinger liquid theoretical framework described here along with the Landauer-Büttiker formula are invaluable tool to understand the properties of single [11, 12] and coupled [13–17] one-dimensional systems. Now that an appropriate theoretical background has been formulated for one-dimensional systems, the discussion will move towards the theoretical description of Coulomb drag taking place between two such one-dimensional systems.

4.3 Theory of 1D-1D Coulomb Drag

The different theoretical models used to describe one-dimensional Coulomb drag can be divided into two main categories. The first one describes Coulomb drag as a mechanism originating from momentum-transfer between electrons in the drive wire and those in the drag wire. Historically, this approach was the first one to be considered. Recently, one-dimensional Coulomb drag has also been interpreted as originating from rectified energy fluctuations rather than momentum transfer because momentum is not a good quantum number in mesoscopic circuits. These two approaches are outlined in the following section of this chapter.

4.3.1 Momentum-Transfer Models

Fermi-Liquid Theory

One of the first approach to describe one-dimensional Coulomb drag was to consider the effect of momentum-exchange between the electrons in the drive and the drag wires, assuming that electrons are ballistic and behave according to the Fermi-liquid model [18–26]. Following Gurevich *et al.* [24], the drag current can be calculated using Boltzmann's equation (equation 2.10) and by considering momentum-exchange between electrons in both wires. This drag current[1] can be written as

$$I_D = -2eL \sum_N \int_0^\infty \frac{dk}{2\pi} \Lambda^{1,2}[f_F^{(1)}, f_F^{(2)}], \tag{4.27}$$

where the summation is carried out over the number of transverse quantized channels N, L is the wires' length and $\Lambda^{1,2}[f_F^{(1)}, f_F^{(2)}]$ is the collision integral from Boltzmann's equation with the index (1,2) referring to electrons in the first and second wire, respectively. Using the Landauer-Büttiker-Imry physical picture [27–29] where each wire is connected to two independent reservoirs in equilibrium, and assuming small excitations (*i.e.* $\frac{eV}{k_BT} \ll 1$), this collision integral is given by

$$\Lambda^{1,2}[f_F^{(1)}, f_F^{(2)}] = \tag{4.28}$$
$$\tfrac{16\pi e^4}{\hbar\kappa^2} \textstyle\sum_{n'} \int \tfrac{dp'}{2\pi\hbar} \int \tfrac{dq}{2\pi\hbar} g_{nn'}(q) \Delta[f_F^{(1)}, f_F^{(2)}] \delta(\epsilon^{(1)} + \epsilon^{(2)} - \epsilon'^{(1)} - \epsilon'^{(2)}),$$

where κ is the dielectric constant of the material, q is the momentum transferred between the wires, $\epsilon^{(1,2)} = \epsilon^{(1,2)}(n, p)$ is the initial electron energy,

---

[1] Strictly speaking, no current is allowed in the drag wire in a Coulomb drag experiment. However, theoretical studies often use an "effective" drag current, which is equivalent to the drag voltage divided by the wire resistance.

$\epsilon'^{(1,2)} = \epsilon'^{(1,2)}(n, p \mp q)$ is the electron energy after scattering and

$$\Delta[f_F^{(1)}, f_F^{(2)}] = \tag{4.29}$$

$$\pm\frac{eV}{k_BT}[1 - f_F(\epsilon^{(1)} - \mu)] \times [1 - f_F(\epsilon^{(2)} - \mu)] f_F(\epsilon'^{(1)} - \mu) f_F(\epsilon'^{(2)} - \mu),$$

$$g_{nn'}(q) = |\int d^2r_\perp \int d^2r'_\perp |\phi_N(r_\perp)|^2 |\phi_N(r'_\perp)|^2 K_0(q\Delta(r_\perp)/\hbar)|^2. \tag{4.30}$$

Here, $K_0(x)$ is the 0^{th} order modified Bessel function, $\Delta(r_\perp) = r_\perp^{(1)} - r_\perp^{(2)}$ and ϕ_N is the electron wavefunction in the N^{th} conduction channel. Iterating through the Boltzmann equation, one obtains as for the drag current [24]

$$I_D = \frac{e^5\hbar^3 L k_B T e V}{\kappa^2} \frac{g_{nn'}(2\hbar k_F)}{v_F^{(1)} v_F^{(2)} (v_F^{(1)} + v_F^{(2)})} \frac{(\Delta(\epsilon)/2k_BT)^2}{sinh^2(\Delta(\epsilon)/2k_BT)^2}. \tag{4.31}$$

The total drag resistance $R_D = -V_D/I = I_D G_D/I$ is therefore given by

$$R_D = \frac{e^2\hbar^2 L k_B T}{\kappa^2} \frac{g_{nn'}(2\hbar k_F)}{v_F^{(1)} v_F^{(2)} (v_F^{(1)} + v_F^{(2)})} \frac{(\Delta(\epsilon)/2k_BT)^2}{sinh^2(\Delta(\epsilon)/2k_BT)^2}. \tag{4.32}$$

Thus, within the Fermi-liquid formalism, one expects the one-dimensional Coulomb drag resistance to be strongly enhanced in the case where the wires have identical densities and to be exponentially suppressed with temperature in the case of wires with a large density imbalance. In the case of identical wires, Coulomb drag scales linearly with temperature, varies as v_F^{-3} and scales[2] as e^{-4k_Fd} for as long as $2k_Fd \gg 1$ (*i.e.* when the the modified Bessel function can be approximated by an exponential). This linear temperature dependence of the Coulomb drag is expected to hold for $\frac{eV}{k_BT} \ll 1$. If $\frac{eV}{k_BT} \gg 1$, the one-dimensional Coulomb drag temperature dependence is proportional to $cosh^{-4}(p^2/4m^*k_BT)$. Therefore, in the vicinity of the crossover between these two regimes, the temperature dependence of the drag resistance becomes non-monotonic [26]. The general shape of these temperature dependencies is presented in figure 4.6 (**a**) and (**b**).

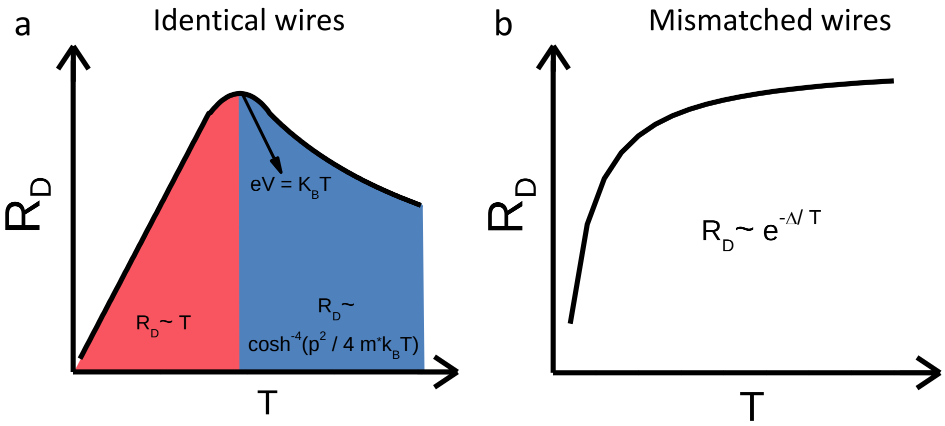

Fig. 4.6: Temperature dependence of the drag resistance within the Fermi liquid formalism for (**a**) wires with an identical density and (**b**) wires with a density mismatch.

Luttinger Liquid Theory - Backscattering

The predictions for Coulomb drag within the Fermi-liquid theory are based on a model that is not expected to be suitable to describe the underlying

---

[2] k and p are related by $p = \hbar k$.

physics of one dimensional systems. Therefore, theoretical calculations based on the Luttinger-liquid model have naturally been developed. Within the linear approximation of the Luttinger-liquid model, backscattering ($\theta = 180°$) is expected to be the sole contributor to the Coulomb drag signal. Several authors have calculated the Coulomb drag signal arising from backscattering in identical wires [30, 31]. Those calculations lead to a temperature dependence of the 1D Coulomb drag behaving in the low-temperature limit as a power-law [32–35], as an exponential decay [36], or as a combination of an exponential divergence and of a power-law [37, 38].

In the formalism developed by Klesse and Stern [37], for instance, the Hamiltonian of a system of interacting wires is given by $H = H_+ + H_- + H_b$, where H_+ and H_- are the Hamiltonians obtained via Luttinger liquid theory (equation 4.20 and equation 4.22) and describes the symmetric and anti-symmetric part of the total Hamiltonian (with new interaction constants $u^{+,-}_{\rho,\sigma}$ and $K^{+,-}_{\rho,\sigma}$). In our case, the new constant of interest is K^-_ρ, the interwire charge TLL interaction parameter. This constant is determined by the difference in small-momenta intra and interwire couplings,

$$K^-_\rho = \sqrt{\frac{1 + U^-_\rho}{1 - U^-_\rho}}, \tag{4.33}$$

where U^-_ρ is a measure of the interwire charge interactions. The Hamiltonian describing backscattering, H_b, is given by

$$\begin{aligned} H_b = \tfrac{2u_\sigma^+\lambda}{\pi\beta^2} \int dx \cos(2\phi_\sigma^+) \cos(2\phi_\sigma^-) - \tfrac{2u_\rho^-\bar{\lambda}}{\pi\beta^2} \int dx \cos(2\phi_\rho^-) \cos(2\phi_\sigma^-) \\ - \tfrac{2u_\rho^-\bar{\lambda}}{\pi\beta^2} \int dx \cos(2\phi_\rho^-) \cos(2\phi_\sigma^+), \end{aligned} \tag{4.34}$$

where $\phi_{\rho,\sigma}^{+,-}$ are the symmetric and antisymmetric bosonization fields, β is a cut-off parameter and $\lambda, \bar{\lambda}$ are coupling parameters. Within the renormalization group treatment and in the absence of interactions, the drag is simply given by $\rho_D(T) = \rho_0 \bar{\lambda}^2 T/E_F$. When interactions are considered, the drag resistance exhibits two qualitatively different behavior, depending on the temperature regime the system is in. In the strong coupling limit at the lowest temperatures, the backscattering Hamiltonian describes two interlocked charge-density waves [37]. In the weak-coupling regime at higher temperature, the coupling constant $\bar{\lambda}$ gets renormalized as a temperature dependent parameter. The transition between these two regimes occurs when $\bar{\lambda} \sim 1$, defining a crossover temperature T^* given by

$$T^* \sim T_F e^{-\frac{k_F d}{1-K_\rho^-}}. \tag{4.35}$$

The dependence of this crossover temperature with 1D density is shown for various values of d and K_ρ^- in figure 4.7.

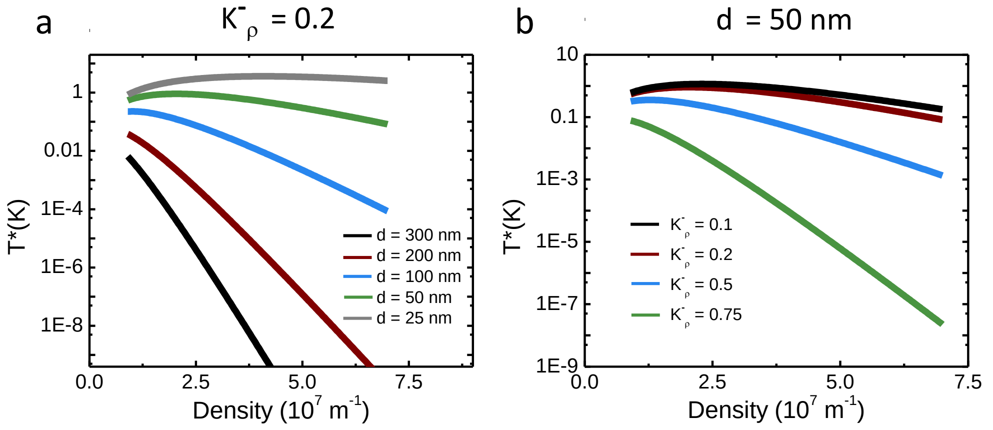

Fig. 4.7: Dependence of the crossover temperature T^* as a function of the 1D density for **(a)** various interwire separations d at fixed $K_\rho^- = 0.2$ and **(b)** various effective interaction parameter K_ρ^- at fixed $d = 50$ nm.

In the weak-coupling regime ($T > T^*$), the temperature dependence of the renormalized coupling constant can be obtained by solving a series of differential equations [37]. Performing the calculation, one obtains $\bar{\lambda}(T) = \lambda_0 \times (T/E_F)^{(K_\rho^- - 1)}$ and the drag signal is thus given by

$$R_D(T) \sim \rho_0 \lambda_0^2 (T/E_F)^{(2K_\rho^- - 1)}. \tag{4.36}$$

The interlocked charge-density waves arising in the strong coupling limit ($T < T^*$) behave as pinned charge density waves. In such systems, the drag signal arises from the thermal creation of soliton/anti-soliton pairs and is given by

$$R_D(T) \sim \rho_0 e^{E_s/T}, \tag{4.37}$$

where E_s is the energy of a soliton [39], which is of the order of the crossover temperature, namely $E_s \sim T^*$. The general shape of this temperature dependence is presented in figure 4.8 **(a)**.

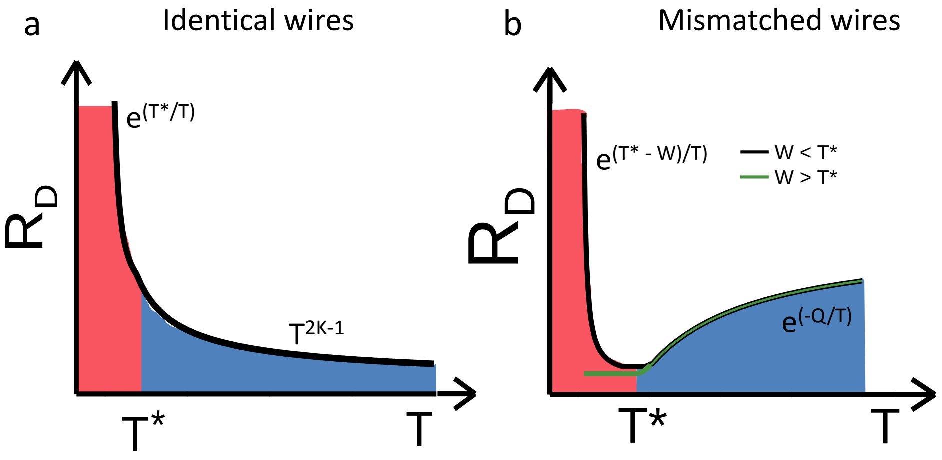

Fig. 4.8: Temperature dependence of the drag resistance within the Luttinger liquid formalism with backscattering for **(a)** wires with an identical density and **(b)** wires with a density mismatch. In the high temperature regime, only the exponential decaying envelope of R_D is plotted, which is a good approximation at large density imbalance between the wires (*i.e.* $Q \gg T$).

The situation is different for non-identical wires [40], or wires with a mismatch in electronic density. When $T < T^*$, the density mismatch between the wires can have a significant impact on the drag signal. To understand it, let us consider a difference in chemical potential W between both wires. If this difference is small, *i.e.* for $W < E_s \simeq T^*$, then the drag signal still behaves similarly to the identical wires case, that is

$$R_D(T) \sim a(T)e^{\Delta/T}, \tag{4.38}$$

where $\Delta \equiv T^* - W$ and the parameter a may be temperature dependent. On the other hand, if there is a large density mismatch between the wires and $W > T^*$, then the drag signal should be significantly reduced and is given by

$$R_D(T) \sim b(T)\left(W^2 - (T^*)^2\right)^{-1/2}, \tag{4.39}$$

where the parameter b can once again be temperature dependent [40]. The specific form of the parameters a and b is however currently unknown. In the weak coupling regime where $T > T^*$, density imbalance between the wires exponentially suppresses the drag signal such that the drag resistance is given by

$$R_D(T) \sim \rho_0 \lambda_0^2 (T/E_F)^{(2K_\rho^- - 1)} \times e^{-Q/T}. \tag{4.40}$$

where $Q = v_\rho^- |k_{F-2} - k_{F-1}| = v_\rho^- |\sqrt{k_{F-1}^2 + 2m^*W/\hbar} - k_F|$. Here, $k_{F-1} = k_F$ and k_{F-2} is the wave-vector of the wire that has been applied a bias W/e. When $Q \ll k_B T$, the exponential decay is negligible and equation 4.40 reverts back to equation 4.36. The general shape of these temperature dependencies is presented in figure 4.8 **(b)**.

If one considers one-dimensional systems at low-density such that $na_B \ll 1$ where $a_B = \kappa\hbar^2/m^*e^2$ is the Bohr radius and κ is the material dielectric constant, then one can reach the spin-incoherent regime for Luttinger liquids. In this regime, the spin exchange energy J between neighboring electrons is exponentially suppressed and $J \ll T \ll E_F$. An estimate of the value of $J \simeq E_F e^{-c/\sqrt{na_B}}$ as a function of 1D density is shown in figure 4.9. In this formalism, c is a constant that is numerically estimated to be 2.9 [41].

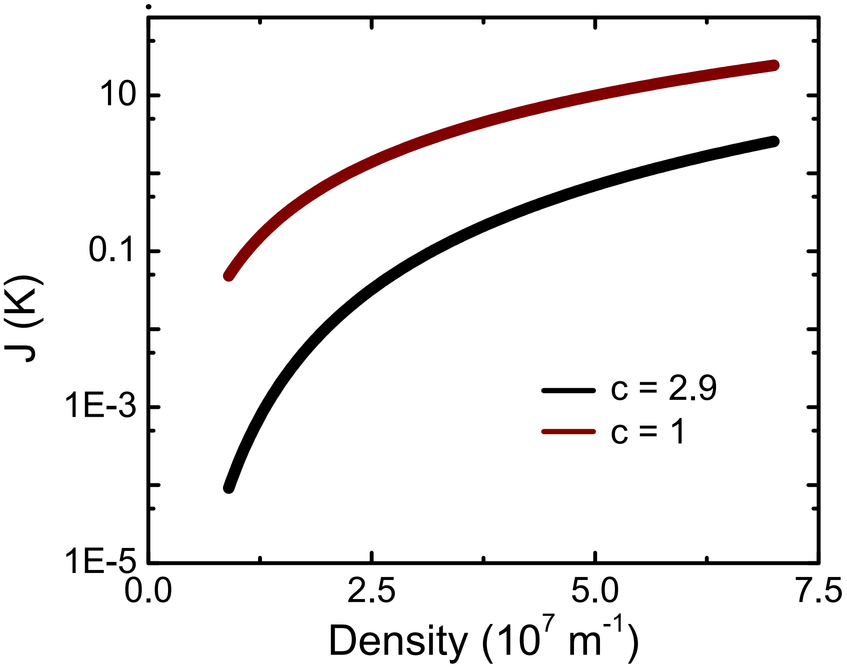

Fig. 4.9: Estimate of the spin exchange energy J as a function of 1D density using c = 2.9 and c = 1.

In this regime, the wires can be described as fluctuating Wigner solids, which dramatically affects the expected temperature dependence of the drag signal, leading to a non-monotonic temperature dependence of the signal [38]. Three different temperature regimes can be achieved within this model. At the lowest temperatures ($T < T^*$), the drag resistance is still given by equation 4.37. In the regime where $T^* < T < J$, the drag resistance is given by

$$R_D(T) \sim T^{\alpha_{2k_F}} e^{-cT/J}. \tag{4.41}$$

where $\alpha_{2k_F} = 2K_\rho - 1$ for clean wires and $\alpha_{2k_F} = 2K_\rho$ for disordered wires. In the highest temperature regime where $T > J$, the drag resistance instead scales as a power-law with temperature,

$$R_D(T) \sim T^{\alpha_{4k_F}}. \tag{4.42}$$

where $\alpha_{4k_F} = 8K_\rho - 3$ for clean wires and $\alpha_{4k_F} = 8K_\rho - 2$ for disordered wires. The general shape of these temperature dependencies is presented in figure 4.10.

The models presented thus far do not include the effect that the finite length of the quantum wires has on the Coulomb drag. When this is taken into account, a non-monotonic temperature dependence for the drag signal might arise [35], the specific of which depends on the value of two parameters : $u = eV/(\hbar\omega_L)$ and $\theta = k_B T/(\hbar\omega_L)$. Here, $\omega_L = v_\rho/L$ is the frequency of the collective plasmonic excitations of the system. These finite length effects are expected to be important for $u/\theta = eV_{drive}/T > 1$. Therefore, for a sufficiently low excitation bias and high temperature, finite-length effects should be negligible.

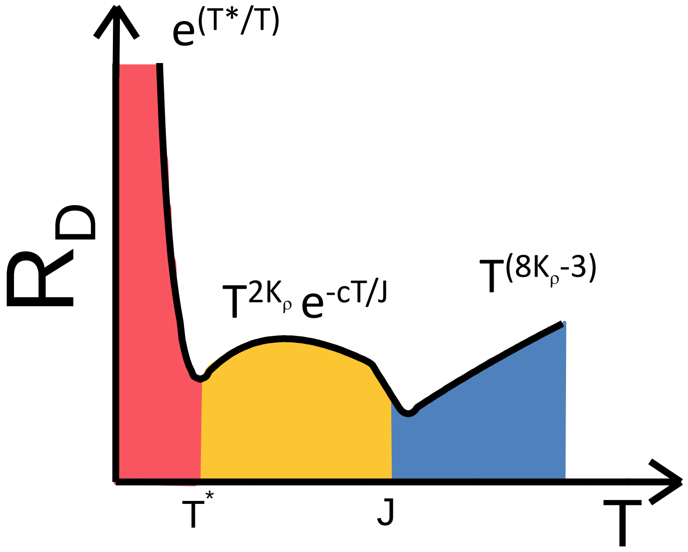

Fig. 4.10: Temperature dependence of the drag resistance of a Luttinger liquid in the spin-incoherent regime for disordered wires.

Luttinger Liquid Theory - Forward Scattering

While backscattering is the only source of momentum transfer yielding to one-dimensional Coulomb drag within the TLL model [42], other contributions to 1D Coulomb drag can occur if one goes beyond its linear approximation. When taking into consideration the non-linearity of the dispersion relation, forward-scattering becomes non-negligible, and can even theoretically be the dominant contribution to drag. As such, several authors have calculated the contribution of forward scattering for the drag [42–46] and predicted a temperature dependence for the drag varying as a power-law with a variety of possible exponent values depending on the experimental details.

Following the seminal work of Pustilnik *et al.* [42], the drag resistance arising from forward scattering is given by

$$R_D = \int_0^\infty dk \int_0^\infty d\omega \frac{k^2 U_{12}^2(k)}{4\pi^3 n_1 n_2 T} \frac{A_1(k,\omega) A_2(k,\omega)}{\sinh^2(\omega/2T)}, \tag{4.43}$$

where U_{12} is the interwire interaction potential and A_i is the imaginary part of the retarded density correlation function. This contribution is significant for $T > T_*$ and for relatively large interwire separation, per the ratio of forward scattering length l_0 to backscattering length l_{2k_F} is given by $l_0/l_{2k_F} \propto e^{-4k_F d}$. At a temperature $T < T^*$ and/or for $k_F d < 1$, backscattering is still the dominant mechanism inducing Coulomb drag and so the drag signal should diverge exponentially following equation 4.37.

In the case of identical wires at a temperature $T > T_F$, the drag resistance simplifies to

$$R_D \sim l_0^{-1} \left(\frac{T_0}{E_F}\right)^2 \left(\frac{T}{E_F}\right)^{-3/2}. \tag{4.44}$$

This behavior is modified if $T_0 < T < T_F$ with T_0 defined as $T_0 = v_F/d$. When this is the case, the temperature dependence of the drag resistance should saturate and be approximately constant,

$$R_D \sim l_0^{-1} \left(\frac{T_0}{E_F}\right)^2. \tag{4.45}$$

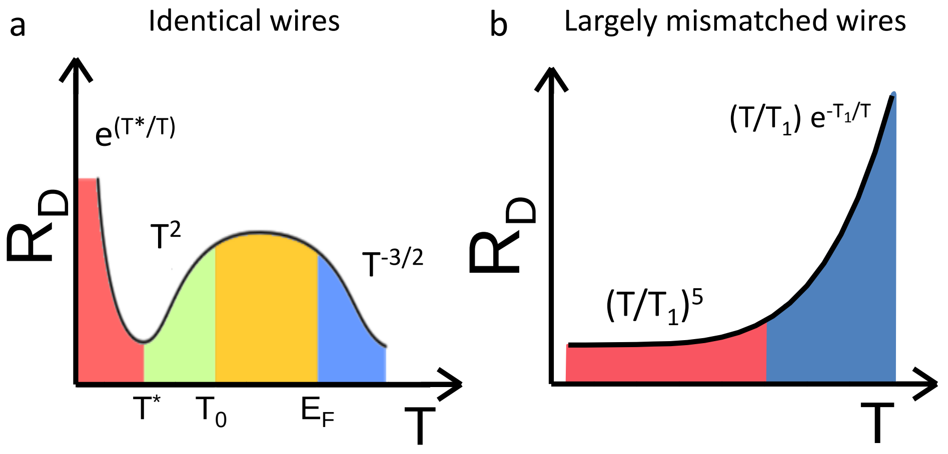

Fig. 4.11: Temperature dependence of the drag resistance within the Luttinger liquid formalism with forward scattering corrections for **(a)** wires with an identical density and **(b)** wires with a large density mismatch. For the large density mismatch case, only forward scattering is considered as backscattering is exponentially suppressed. For a slight density mismatch between the wires, the drag resistance can still increase with decreasing temperature for $T < T^*$ if backscattering is stronger than forward scattering.

If the temperature is lowered further so that $T^* < T < T_0$, then the drag resistance takes the form

$$R_D \sim \frac{c_i}{l_0}\left(\frac{T}{E_F}\right)^2, \tag{4.46}$$

where $c_i = \pi^2/4$ in the case of negligible intra-wire electron-electron interactions. When intra-wire interactions are taken into account, the general shape of equation 4.46 remains the same, but $c_i \propto \frac{g^6}{1+g}$ with g defined as $g = \frac{v_F}{u_\rho}$. A plot of this temperature dependence is presented in figure 4.11 **(a)**.

Once again, the overall behavior of the drag should be different for wires with mismatched densities. While this imbalance should not affect the form of the drag resistance in the high temperature regime ($T > T_1 = k_F \Delta(v_F)$), it does however significantly modify the shape of the drag signal at lower temperatures [42]. In this case, the temperature dependence of the drag signal can have two forms. At the lowest temperature and considering intra-wire interactions, the drag signal should scale as a power-law with temperature,

$$R_D \sim \left(\frac{T_1}{E_F}\right)^4 \left(\frac{T}{T_1}\right)^5 . \tag{4.47}$$

However, at higher temperature, the drag signal should deviate from a power-law dependence and rather follow an activated behavior,

$$R_D \sim \left(\frac{T_1}{E_F}\right)^2 \frac{T}{T_1} e^{-T_1/T} . \tag{4.48}$$

Considering $T_1 \sim 5.4$ K and $T_F \sim 20$ K, the transition between these two temperature regimes should occur at $T \sim 450$ mK, when both contribution have a comparable magnitude. The overall general trend of this temperature dependence is presented in figure 4.11 **(b)**. For large density imbalance between the wires, backscattering is exponentially suppressed and forward scattering is the dominant contribution to Coulomb drag. However, it still possible for backscattering to overcome forward scattering if there is only a slight density imbalance between the wires.

In summary, within the the momentum-transfer formalism, one expects the drag signal to be positive,[3] and to be maximal for the case of identical wires. It is also expected to follow the Onsager symmetry relation.[4] This remains true regardless of the specific model used. In contrast, the analytic form of the temperature dependence of the drag signal is heavily dependent on the specifics of the model used to calculate the drag resistance.

4.3.2 Charge-Fluctuation Models

The models discussed in the previous section describe the Coulomb drag phenomenon as originating from momentum-transfer between the electrons in the drive and the drag wire. However, this orthodox interpretation of one-dimensional Coulomb drag has recently been challenged by a few theoretical groups [47–51] arguing that in mesoscopic circuits, momentum is not a good quantum number and Coulomb drag might instead be understood in terms of energy (or charge) fluctuations.

This energy transfer occurs via spontaneous fluctuations that create charge accumulation in a wire, and charge depletion in the other. These voltages are then rectified and their direction and strength depend on the specific spatial symmetry of the system, on the specific impurities potential as well as on the transmission property of the wire at various energies. Thus, in such mesoscopic circuits, the Onsager symmetry relations can be broken [48, 50]. The fluctu-

---

[3] It is possible to obtain a negative drag resistance within the momentum-transfer formalism if one is measuring drag between electrons and effective holes, in a fashion similar to the one depicted in figure 2.12.

[4] If $R_D^{i,j}$ describes a Coulomb drag system where i is the drive wire and j is the drag wire, the Onsager symmetry relation states that $R_D^{1,2} = R_D^{2,1}$.

ations can either occur in the wire itself, or in the leads connecting the wire to the 2D reservoirs. In both cases, the presence of a negative Coulomb drag signal is predicted if the drive or drag wire possesses a sufficient electron-hole asymmetry in the transmission probability across the wires. The onset of a non-zero drag signal relies critically on the presence of electron-hole asymmetry and a local enhancement of such an asymmetry is expected to occur at the opening of 1D subbands in either wires, leading to a local maxima in the strength of the drag signal [49].

Coulomb drag calculations have only been performed for coupled quantum dots [50] in the case of an intrinsic coupling, a coupling taking place solely between the two electrical circuits and not their leads or reservoirs. However, similar calculations have been performed for contact-coupled wires, a system for which the fluctuations are occurring in the leads [49]. In this case, the Coulomb drag signal arising from energy fluctuations is given by

$$I_D = V\frac{h^2}{4\pi e^4}\int d\omega \frac{\alpha_+(\omega)}{\omega^2}\frac{\partial}{\partial\omega}\coth(\frac{\omega}{2T})\Gamma_1(\omega)\Gamma_2(\omega). \tag{4.49}$$

Here $\Gamma_i(\omega)$ is the rectification coefficient of the wire given by

$$\Gamma(\omega) = \frac{2e^3}{h}\sum_N \int d\epsilon\, (f_F(\epsilon_-) - f_F(\epsilon_+)) \left(|t_N(\epsilon_+)|^2 - |t_N(\epsilon_-)|^2\right), \tag{4.50}$$

where $\epsilon_-(\epsilon_+)$ is the energy of electrons (holes) and t_N is the transmission probability across the N^{th} channel of the wire. Also, $\alpha_+ = (2e^4/h^2) \times (|Z_{LL}|^2 -$

$2Z_{LR}Z_{RL} + |Z_{RR}|^2)$ is a dimensionless interaction kernel where Z_{ij} are elements of the trans-impedance matrix defined as $Z_{ij} = \partial\Phi_i/\partial I_j$ where Φ_i (I_j) is the fluctuating voltage (current). For a non-monotonic transmission probability across either wires in the case of density imbalance, it is possible for one of the rectification coefficients to be negative and as such obtain a negative Coulomb drag signal. Within this formalism, the drag signal is expected to follow a quadratic dependence with temperature, $R_D \propto T^2$.

A summary of all predictions for the temperature dependencies of Coulomb drag within the momentum-transfer and the charge-fluctuation models is presented in figure 4.12. In the following chapters of this thesis, more specifically in chapters 6 and 7, I will present experimental Coulomb drag data obtained in vertically-coupled quantum wires. These data will be compared to the various theoretical models for one-dimensional Coulomb drag described in this section.

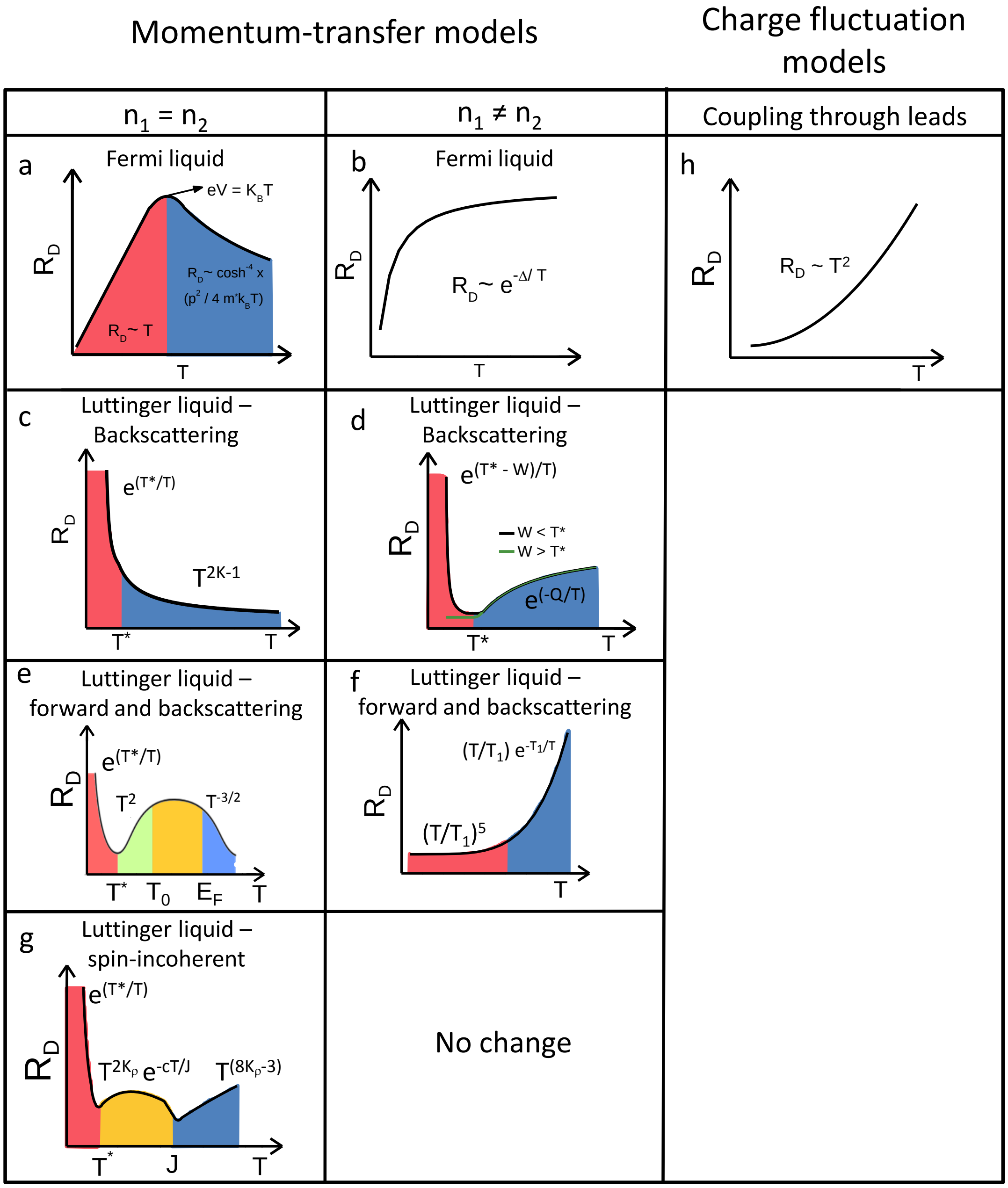

Fig. 4.12: Summary of the main theoretical results for the temperature dependence of 1D Coulomb drag. **(a)** Fermi liquid theory and identical wires, **(b)** Fermi liquid theory and density mismatched wires, **(c)** Luttinger liquid theory with backscattering and identical wires, **(d)** Luttinger liquid theory with backscattering and density mismatched wires, **(e)** Luttinger liquid theory with forward scattering and identical wires, **(f)** Luttinger liquid theory with forward scattering and density mismatched wires, **(g)** Luttinger liquid theory in the spin-incoherent regime and identical wires and **(h)** the charge-fluctuation model.

4.4 Pioneering Experiments in Quantum Wires

4.4.1 Single Quantum Wires

The first experimental realization of a ballistic and quantized one-dimensional wire was achieved in 1988 independently by Mooji's group at Delft University (in collaboration with Phillips laboratories) [2] and by Pepper's group at Cambridge University [3]. Both groups found that the conductance of a narrow constriction of variable width formed in a GaAs 2DEG was quantized in integer increments of $2e^2/h$, in agreement with Landauer's transport theory (equation 4.6). By applying a negative bias on a set of metal split gates deposited on the surface of the heterostructure, these two groups were able to effectively constrict the width of the 2DEG located underneath the gates, and an increase in the resistance of the resulting quantum wire was observed whenever a conduction channel would close. One of such measurements is presented in figure 4.13 along with a schematic of the split gates design used to produce the quantum wire.

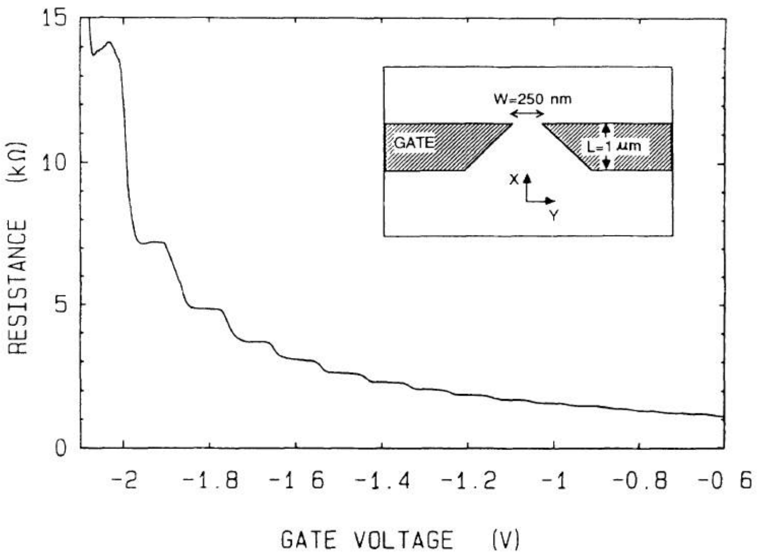

Fig. 4.13: First experimental observation of quantized resistance in a quantum wire. After subtracting a series resistance from the data, the plateau features are separated by integer values of $h/2e^2$. The inset shows a schematic of the split gates used to produce the quantum wire. Figure taken from van Wess *et al.* [2].

Following this important milestone, experiments were performed on quantum wires fabricated using several different techniques, such as ion implantation [52], dry [53] and wet [54, 55] etching, as well as cleaved-edge overgrowth (CEO) [56]. Despite one-dimensional systems being expected to behave as a Luttinger-liquid with electron-electron interactions playing an important role, the experimental results obtained in quantum wires have been completely understood in terms of interactionless electrons. It was not until 1995 that Tarucha's group in Japan showed partial evidence, from the temperature dependence of a quantum wire conductance, that quantum wires indeed behave as Luttinger liquids [57].

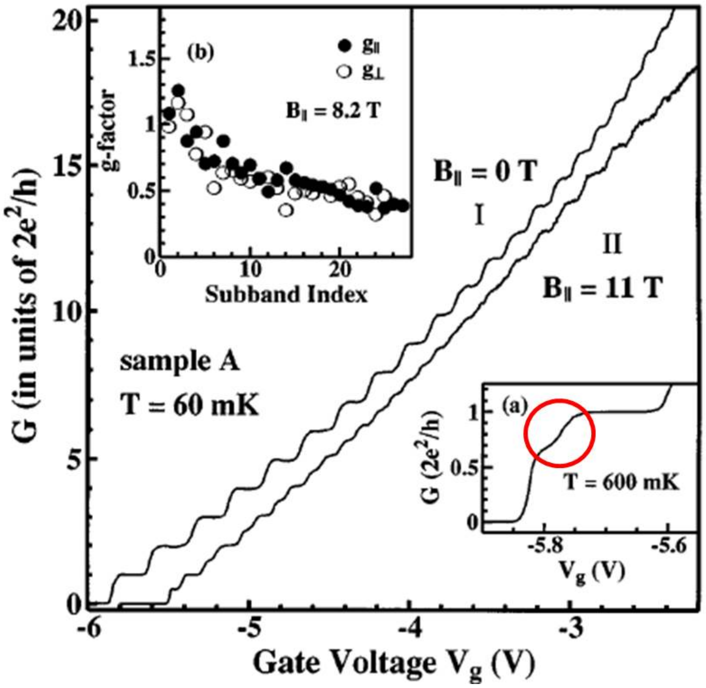

Fig. 4.14: Figure showing the quantized resistance observed in a quantum wire, along with the 0.7 structure in the inset. Figure taken from Thomas *et al.* [58].

Shortly after, perhaps the largest departure from the single-electron behavior in quantum wires was observed in 1996 in Pepper's group where a feature appearing at a conductance of $\sim 0.7 \times 2e^2/h$ was observed [58, 59]. The origin of this feature, now known as the 0.7 structure, is not fully understood to this day. This feature is believed to not be caused by impurity scattering, nor by a transmission resonance. An example of this anomalous structure is presented in figure 4.14. Experimental studies have found, amongst other things, that the 0.7 structure strengthens with temperature (up to $T \sim 1.5$ K) and that, in the presence of a magnetic field, moves towards a value of $\sim 0.5 \times 2e^2/h$, the conductance value of quantum wires where Zeeman splitting has occurred [58, 59].

In addition, a zero-bias anomaly also appears in its source-drain characteristics [60, 61]. Two of the most popular mechanisms to explain the origin of the 0.7 structure are : *i)* a spontaneous spin-polarization of the electrons [62, 63] and *ii)* Kondo-physics [64–66]. A spin-gap model [67, 68] and/or the presence of bound states [69, 70] have also been proposed to explain the origin of this structure. However, none of these models fully describe the properties this structure. Recently [71], the presence of a van Hove singularity in the local density of state near the first plateau of the quantum wire has been proposed to at the origin of the 0.7 structure and appears thus far to be in agreement with experimental results. Similar structures have also been observed at a higher conductance value (*i.e.* at $\sim 1.7 \times 2e^2/h$), although they have not been the subject of as much experimental and theoretical work [72]. For more information regarding this phenomenon, I refer the reader to a review by A. P. Micolich [73].

4.4.2 Coupled Quantum Wires Systems

Despite the large amount of experimental transport measurements performed in single quantum wires, very little conclusive evidence exists regarding the interacting nature of one-dimensional electrons, per the Luttinger liquid model. This is due to the very nature of the transport measurements realized in single quantum wires. In conductance measurements, one effectively probes a physical quantity that comes from processes entirely taking place outside the wire, where the electrons are non-interacting [4, 5]. Generally speaking, to observe interacting physics in the transport of single quantum wires, one would need to measure the wires' properties before they have been washed out by similar processes occurring in the reservoirs, at a frequency $f \gtrsim v_\rho/L \sim 10^{10}$ Hz where the excitation wavelength is shorter than the wire segment [17]. At low temperature, these high frequencies are however difficult to explore experimentally. In contrast, in systems of *coupled* quantum wires, it is possible to measure transport properties arising from processes solely occurring in the wires, and not in the leads, such as 1D tunneling and 1D Coulomb drag. Therefore, in *coupled* 1D system, it is possible to observe interacting electrons and Luttinger liquid physics at low frequency since such intrinsic 1D phenomenon would not be washed out by processes taking place in the leads. Coupling two quantum wires in close proximity, however, is a difficult feat that very few experimental groups have been able to achieve thus far.

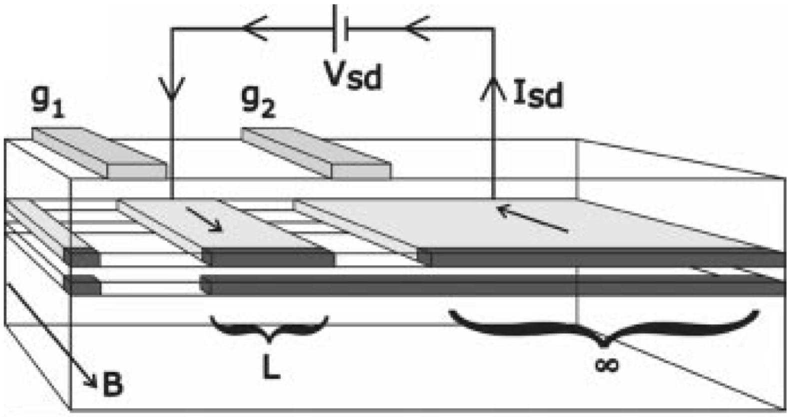

Fig. 4.15: Schematic of vertically-coupled quantum wires grown by cleaved-edge overgrowth. In this design, the lower quantum wire is not populated with electrons and can only be accessed through tunneling from the upper wire and the tunneling barrier are created by the gates g1 and g2. Figure taken from Auslaender *et al.* [74].

In 2002, Yacoby's group has been able to vertically couple two cleaved-edge overgrown quantum wires in close proximity [74], as shown in figure 4.15. Using this geometry and tunneling measurements, a series of seminal experiments were performed and verified several of Luttinger liquid predictions. These are the zero-bias anomaly in the one-dimensional tunneling [75], spin-charge separation [15] and charge partitioning [17]. Another study measuring 1D-2D tunneling between a 2DEG and an array of quantum wires was performed in Ritchie's group in 2009 [16]. Spin-charge separation and a zero-bias anomaly in the tunneling, two hallmarks of Luttinger liquids, were also observed in this experiment and confirmed that coupled 1D systems are perfectly suited to observed Luttinger liquid physics. Despite such success, the techniques used to perform these measurements were not suitable to perform Coulomb drag. In the Jompul *et al.* experiment, wires were only present in a single layer while in the Auslaender *et al.* experiment, both wires were not independently contacted. Therefore, a different design was required to perform a one-dimensional Coulomb drag measurement.

4.5 Previous Experimental 1D-1D Coulomb Drag Results

The first one-dimensional Coulomb drag experiments used a lateral coupling of the quantum wires where the device was fabricated in a single 2DEG and the wires were separated by a depleted 2DEG region, defined using an electrostatic split gate. A schematic of this lateral design, used by Debray *et* *al.* [76] and Yamamoto *et al.* [77], is presented in figure 4.16.

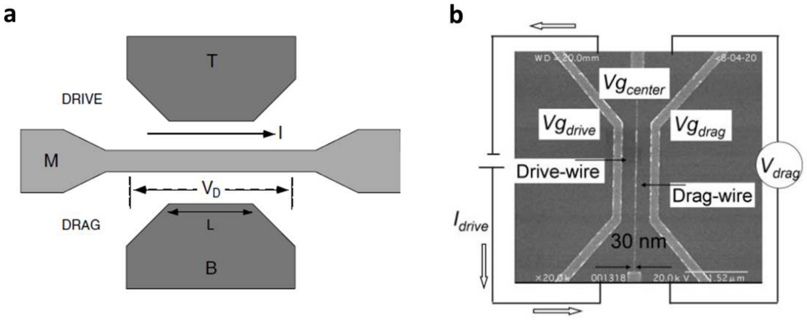

Fig. 4.16: Schematics of the laterally-coupled quantum wires used in previous one-dimensional Coulomb drag studies. In this design, both wires are fabricated in a single 2DEG and are separated by an electrostatic split gate. Figure **(a)** is taken from Debray *et al.* [76] and figure **(b)** from Yamamoto *et al.* [77].

The wires conductance in both these experiments is in the non-ballistic regime, whereby the 1D plateau-like features occur at non integer values of $2e^2/h$. One of the main drawback of the lateral geometry is that the barrier separating the two quantum wires has to be relatively wide. There are two mechanisms at the origin of this size limitation. Firstly, there is a shadowing effect in gated nanostructures, as previously explained in chapter 3 (see figure 3.1). The second factor contributing to the barrier size limitation is the need to suppress tunneling so as to not contaminate the drag signal. This leads to the need of a large depleted region to satisfy this condition. In addition to reducing the strength of the Coulomb drag signal, having a wide barrier makes the Coulomb drag measurement susceptible to be polluted by *phonon* drag since phonon drag becomes stronger than Coulomb drag as the interwire separation becomes larger. Theoretically, phonon drag has been estimated to

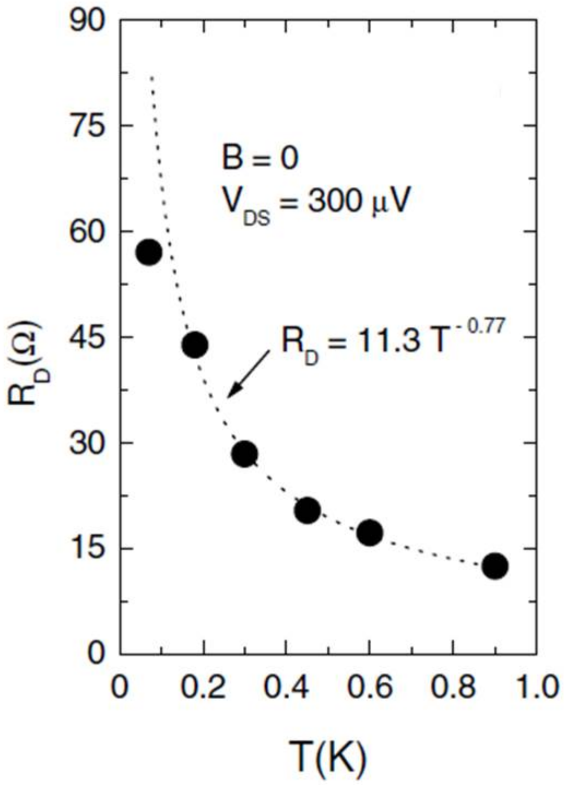

Fig. 4.17: Coulomb drag signal as a function of temperature in laterally-coupled quantum wires showing an increase of the drag resistance with decreasing temperature. Figure taken from Debray *et al.* [76].

have a non negligible impact on the Coulomb drag measurement above 0.1 K for $k_F d \gtrsim 5$ and to dominate the measurement for $k_F d \gtrsim 10$ [78].

Despite these limitations, 1D Coulomb drag experiments were performed by Debray *et al.* in 2001 [76]. These measurements showed a modulation of the Coulomb drag signal with the 1D subband occupancy of the wires, as well as evidence of an increase of the drag resistance as $T \to 0$ at a 1D subband occupancy of $N = 1$, where the drag signal was maximal. This trend, shown in figure 4.17, was interpreted in term of the Luttinger liquid theory, yielding to an interaction parameter $K_\rho^- \sim 0.2$, which is much lower than previous K_ρ values reported in the literature of GaAs/AlGaAs heterostructures [75]. [5] Their estimated dimensionless parameter $k_F d \sim 3$ suggests the measurement being outside of the phonon-drag dominated regime, with the caveat that their estimated k_F value is approximately six times lower than what is estimated from experiments with similar design and initial 2D parameters [15, 77, 79]. Such a large discrepancy raises some doubt as to whether or not the measurement was indeed influenced by phonons.

Another significant experimental Coulomb drag study was reported in 2006 [77]. In this case, the authors reported the observation of a negative Coulomb drag regime occurring at low density in the wires (*i.e.* 1D subband occupancy $N < 1$) and in the presence of a magnetic field. An example of the data is shown in figure 4.18. This observation of negative Coulomb drag was heuristically attributed to Wigner crystallization [77, 80], however, they were also were realized in a regime with $6 \lesssim 2k_F d \lesssim 13$, and so potentially susceptible to contamination by phonon drag.

In order to achieve a smaller separation between the quantum wires, and hence a smaller $2k_F d$, the quantum wires used in this thesis have been fabricated in a *vertical* geometry. In this geometry, a hard MBE-defined AlGaAs barrier separates the two quantum wires, offering several advantages. First, it is possible to couple the wires at the nanoscale ($d \sim 40$ nm) without significant

---

[5] This discrepancy could be partly explained by the fact that K_ρ^- is the TLL parameter of relative charge, which is determined by the difference of the small-momentum intra-wire and interwire couplings [37].

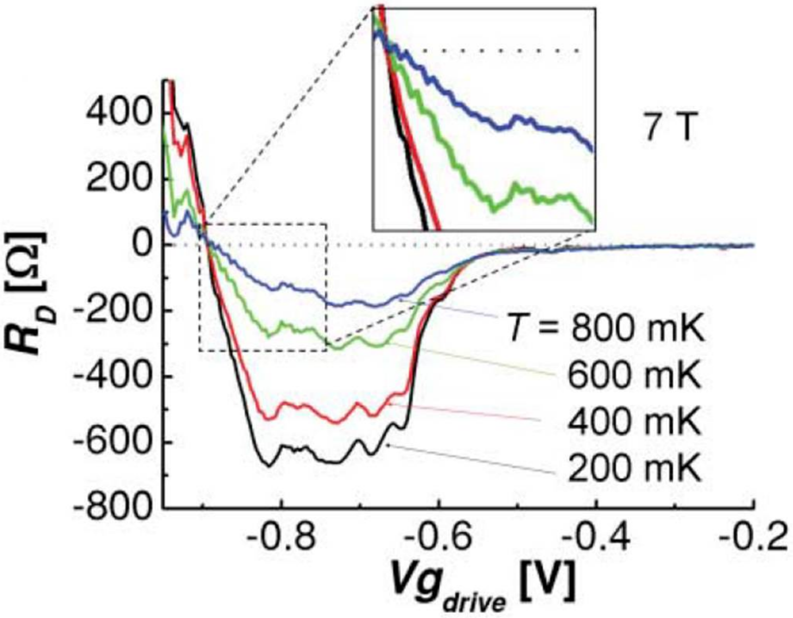

Fig. 4.18: Coulomb drag signal as a function of gate voltage (or 1D subband occupancy) showing a negative one-dimensional Coulomb drag signal at low 1D density. Figure taken from Yamamoto *et al.* [77].

1D tunneling, allowing us to explore an entirely new coupling regime. Such a strong coupling should also allow us to observe a stronger drag signal. Second, the barrier between the wires is atomically defined, allowing us to precisely know the interwire separation in these devices. The price to pay in this approach, however, is the heavy processing required to fabricate the wires. This fabrication process is described in the chapter 5 of this thesis.

References

[1] Landauer, R. *IBM J. Res. Dev.* **1**, 223 (1957).

[2] van Wees, B. J., van Houten, H., Beenakker, C. W. J., Williamson, J. G., Kouwenhoven, L. P., van der Marel, D., and Foxon, C. T. *Phys. Rev. Lett.* **60**, 848 (1988).

[3] Wharam, D. A., Thornton, T. J., Newbury, R., Pepper, M., Ahmed, H., Frost, J. E. F., Hasko, D. G., Peacock, D. C., Ritchie, D. A., and Jones, G. A. C. *J. Phys. C: Solid State Phys.* **21**, L209 (1988).

[4] Maslov, D. L. and Stone, M. *Phys. Rev. B* **52**, 5539 (1995).

[5] Ponomarenko, V. V. *Phys. Rev. B* **52**, 8666 (1995).

[6] Giamarchi, T. *Quantum Physics in One Dimension.* Oxford University Press, (2003).

[7] Tomonaga, S. *Progr. Theor. Phys.* **5**, 544 (1950).

[8] Luttinger, J. M. *J. Math. Phys.* **4**, 1154 (1963).

[9] Mattis, D. C. and Lieb, E. H. *J. Math. Phys.* **6**, 304 (1965).

[10] Haldane, F. D. M. *Phys. Rev. Lett.* **47**, 1840 (1981).

[11] Bockrath, M., Cobden, D. H., Lu, J., Rinzler, A. G., Smalley, R. E., Balents, L., and McEuen, P. L. *Nature* **397**, 598 (1998).

[12] Liao, Y.-A., Rittner, A. S. C., Paprotta, T., Li, W., Partridge, G. B., Huler, R. G., Baur, S. K., and Mueller, E. J. *Nature* **467**, 567 (2010).

[13] Milliken, F. P., Umbach, C. P., and Webb, R. A. *Solid. State. Comm.* **97**, 309 (1995).

[14] Chang, A. M., Pfeiffer, L. N., and West, K. W. *Phys. Rev. Lett.* **77**, 2538 (1996).

[15] Auslaender, O. M., Steinberg, H., Yacoby, A., Tserkovnyak, Y., Halperin, B. I., Baldwin, K. W., Pfeiffer, L. N., and West, K. W. *Science* **308**, 88 (2005).

[16] Jompul, Y., Ford, C. J. B., Griffiths, J. P., Farrer, I., Jones, G. A. C., Anderson, D., Ritchie, D. A., Silk, T. W., and Schofield, A. J. *Science* **325**, 597 (2009).

[17] Steinberg, H., Barak, G., Yacoby, A., Pfeiffer, L. N., West, K. W., Halperin, B. I., and Le Hur, K. *Nature Physics* **4**, 116 (2008).

[18] Tso, H. C. and Vasilopoulos, P. *Phys. Rev. B* **45**, 1333 (1992).

[19] Sirenko, Y. M. and Vasilopoulos, P. *Phys. Rev. B* **46**, 1611 (1992).

[20] Tanatar, B. *Solid State Comm.* **99**, 1 (1996).

[21] Tanatar, B. *Phys. Rev. B* **58**, 1154 (1998).

[22] Raichev, O. and Vasilopoulos, P. *Phys. Rev. B* **61**, 7511 (2000).

[23] Raichev, O. and Vasilopoulos, P. *J. Phys.: Condens. Matter* **12**, 6859 (2000).

[24] Gurevich, V. L., Pevzner, V. B., and Fenton, E. W. *J. Phys.: Condens. Matter* **10**, 2551 (1998).

[25] Lyo, S. K. *Phys. Rev. B* **68**, 045310 (2003).

[26] Muradowv, M. I. and Gurevich, V. L. *J. Phys.: Condens. Matter* **24**, 135304 (2012).

[27] Imry, Y. *Directions in Condensed Matter Physics.* World Scientific, (1986).

[28] Büttiker, M. *Phys. Rev. Lett.* **57**, 1761 (1986).

[29] Laudauer, R. *IBM J. Res. Dev.* **32**, 306 (1989).

[30] Flensberg, K. *Phys. Rev. Lett.* **81**, 184 (1998).

[31] Ponomarenko, V. V. and Averin, D. V. *Phys. Rev. Lett.* **85**, 4928 (2000).

[32] Nazarov, Y. V. and Averin, D. V. *Phys. Rev. Lett.* **81**, 653 (1998).

[33] Schlottmann, P. *Phys. Rev. B* **69**, 035110 (2004).

[34] Schlottmann, P. *Phys. Rev. B* **70**, 115306 (2004).

[35] Peguiron, J., Bruder, C., and Trauzettel, B. *Phys. Rev. Lett.* **99**, 086404 (2007).

[36] Dmitriev, A. P., Gornyi, I. V., and Polyakov, D. G. *Phys. Rev. B* **86**, 245402 (2012).

[37] Klesse, R. and Stern, A. *Phys. Rev. B* **62**, 16912 (2000).

[38] Fiete, G. A., Le Hur, K., and Balents, L. *Phys. Rev. B* **73**, 165104 (2006).

[39] Rice, M. J., Bishop, A. R., Krumhansl, J. A., and Trullinger, S. E. *Phys. Rev. Lett.* **36**, 432 (1976).

[40] Fuchs, T., Klesse, R., and Stern, A. *Phys. Rev. B* **71**, 045321 (2005).

[41] Matveev, K. A. *Phys. Rev. Lett.* **92**, 106801 (2004).

[42] Pustilnik, M., Mishchenko, E. G., Glazman, L. I., and Andreev, A. V. *Phys. Rev. Lett.* **91**, 126805 (2003).

[43] Mortensen, N. A., Flensberg, K., and Jauho, A.-P. *Phys. Rev. B* **65**, 085317 (2002).

[44] Aristov, D. N. *Phys. Rev. B* **76**, 085327 (2007).

[45] Rozhkov, A. V. *Phys. Rev. B* **77**, 125109 (2008).

[46] Pereira, R. G. and Sela, E. *Phys. Rev. B* **82**, 115324 (2010).

[47] Narozhny, B. N. and Aleiner, I. L. *Phys. Rev. Lett.* **84**, 5383 (2000).

[48] Mortensen, N. A., Flensberg, K., and Jauho, A. P. *Phys. Rev. Lett.* **86**, 1841 (2001).

[49] Levchenko, A. and Kamenev, A. *Phys. Rev. Lett.* **101**, 216806 (2008).

[50] Sánchez, R., López, R., Sánchez, D., and Büttiker, M. *Phys. Rev. Lett.* **104**, 076801 (2010).

[51] Büttiker, M. and Sánchez, R. *Nature Nanotech.* **6**, 757 (2011).

[52] Nakata, N., Hirayama, Y., Tarucha, S., and Horikoshi, Y. *J. Appl. Phys. Lett.* **69**, 3633 (1991).

[53] Ismail, K., Antoniadis, D. A., and Smith, H. I. *Appl. Phys. Lett.* **54**, 1130 (1989).

[54] Ghanbari, R. A., Chu, W., Moon, E. E., Burkhardt, M., Yee, K., Antoniadis, D. A., Smith, H. I., Schattenburg, M. L., Rhee, K. W., Bass, R., Peekerar, M. C., and Melloch, M. R. *J. Vac. Sci. Technol. B* **10**, 3196 (1992).

[55] Grundbacher, R., Chang, H., Hannan, M., and Adesida, I. *J. Vac. Sci. Technol. B* **11**, 2254 (1993).

[56] Yacoby, A., Störmer, H. L., Baldwin, K. W., Pfeiffer, L. N., and West, K. W. *Solid State Commun.* **101**, 77 (1997).

[57] Tarucha, S., Honda, T., and Saku, T. *Solid State Commun.* **94**, 413 (1995).

[58] Thomas, K. J., Nicholls, J. T., Simmons, M. Y., Pepper, M., Mace, D. R., and Ritchie, D. A. *Phys. Rev. Lett.* **77**, 135 (1996).

[59] Thomas, K. J., Nicholls, J. T., Appleyard, N. J., Simmons, M. Y., Pepper, M., Mace, D. R., Tribe, W. R., and Ritchie, D. A. *Phys. Rev. B* **58**, 4846 (1998).

[60] Kristensen, A., Bruus, H., Hansen, A. E., Jensen, J. B., Lindelof, P. E., Marckmann, C. J., Nygard, J., Sørenson, C. B., Beuscher, F., Forchel, A., and Michel, M. *Phys. Rev. B* **62**, 10950 (2000).

[61] Cronenwett, S. M., Lynch, H. J., Goldhaber-Gordon, D., Kouwenhoven, L. P., Marcus, C. M., Hirose, K., Wingreen, N. S., and Umansky, V. *Phys. Rev. Lett.* **88**, 226805 (2002).

[62] Wang, C.-K. and Berggren, K.-F. *Phys. Rev. B* **54**, 14257 (1996).

[63] Wang, C.-K. and Berggren, K.-F. *Phys. Rev. B* **57**, 4552 (1998).

[64] Lindelof, P. E. *Proc. SPIE* **4415**, 77 (2001).

[65] Meir, Y., Hirose, K., and Wingreen, N. S. *Phys. Rev. Lett.* **89**, 196802 (2002).

[66] Lindelof, P. E. and Aagesen, M. *J. Phys.: Condens. Matter* **20**, 164207 (2008).

[67] Bruus, H., Cheianov, V. V., and Flensberg, K. *Physica E* **10**, 97 (2001).

[68] Kristensen, A. and Bruus, H. *Phys. Scr.* **T101**, 151 (2002).

[69] Rejec, T. and Meir, Y. *Nature* **442**, 900 (2006).

[70] Güçlü, A. D., Umrigar, C. J., Jiang, H., and Baranger, H. U. *Phys. Rev. B* **80**, 201302 (2009).

[71] Bauer, F., Heyder, J., Schubert, E., Borowsky, D., Taubert, D., Bruognolo, B., Schuh, D., Wegscheider, W., von Delft, J., and Ludwig, S. *Nature* **501**, 73 (2013).

[72] Graham, A. C., Thomas, K. J., Pepper, M., Cooper, N. R., Simmons, M. Y., and Ritchie, D. A. *Phys. Rev. Lett.* **91**, 136404 (2003).

[73] Micolich, A. P. *J. Phys.: Condens. Matter* **23**, 443201 (2011).

[74] Auslaender, O. M., Yacoby, A., Picciotto, R., Baldwin, K. W., Pfeiffer, L. N., and West, K. W. *Science* **295**, 825 (2002).

[75] Tserkovnyak, Y., Halperin, B. I., Auslaender, O. M., and Yacoby, A. *Phys. Rev. B* **68**, 125312 (2003).

[76] Debray, P., Zverev, V., Raichev, O., Klesse, R., Vasilopoulos, P., and Newrock, R. S. *J. Phys.: Condens. Matter* **13**, 3389 (2001).

[77] Yamamoto, M., Stopa, M., Tokura, Y., Hirayama, Y., and Tarucha, S. *Science* **313**, 204 (2006).

[78] Raichev, O. E. *Phys. Rev. B* **64**, 035324 (2001).

[79] Bielejec, E., Reno, J. L., Lyo, S. K., and Lilly, M. P. *Solid State Comm.* **147**, 79 (2008).

[80] Yamamoto, M., Takagi, H., Stopa, M., and Tarucha, S. *Phys. Rev. B* **85**, 041308(R) (2012).

5

Fabrication of Vertically-Integrated 1D-1D Devices

In this chapter, the design and the fabrication details of the vertically-integrated quantum wires are presented. Despite the fact that fabricating vertically-coupled quantum wires is significantly harder than fabricating their laterally-coupled counterpart, the vertical geometry is the prime choice for the Coulomb drag experiment since it circumvents most of the drawbacks of the horizontal geometry. Indeed, as described in chapter 4, the effective $2k_Fd$ parameter is relatively large in the lateral geometry, *i. e.* $2k_Fd > 5$. In contrast, it is relatively straightforward to achieve a regime where $2k_Fd < 5$ in the vertical geometry, so that both phonon drag and tunneling are negligible. In the remainder of this chapter, I will present the details of the GaAs/AlGaAs heterostructure in which the vertically-coupled quantum wires are fabricated as well as the design and the fabrication process used to independently contact each wire.

5.1 Heterostructure Description

Since the two quantum wires are fabricated in two different quantum wells in the vertical geometry, a double quantum well heterostructure has to be used as starting material. This contrasts with the single quantum well heterostructure used in previous 1D Coulomb drag studies performed in a lateral geometry and depicted in figure 3.4. Such a double quantum-well heterostructure is shown in figure 5.1 and consists of two quantum wells separated by a thin AlGaAs dielectric layer. The width of this barrier can be adjusted during the growth process and can be as thin as one epitaxial layer. From previous studies performed in double quantum well heterostructures [1], it was determined that a barrier with a width larger than 11 nm is required to have negligible tunneling between both layers when the barrier aluminum content is 30%. Such a low tunneling signal is required to perform Coulomb drag experiments.

To fabricate the vertically-coupled quantum wires, one needs to define a single quantum wire on each side of the heterostruture. The technique of choice to realize this difficult task is the epoxy-bound-and-stop-etch (EBASE) technique [2], developed at Sandia National Laboratories in the 1990's. This technique involves gluing a host substrate on top of the device, and mechanically lapping and chemically etching the original substrate until the bottom surface is $\sim$ 150 nm away from the lower quantum well. A key element of this technique is the presence of two additional layers in the wafer located between the spacer and the buffers of the heterostructure. The thickest of these layers is an AlGaAs stop-etch layer with a 55% aluminum concentration that

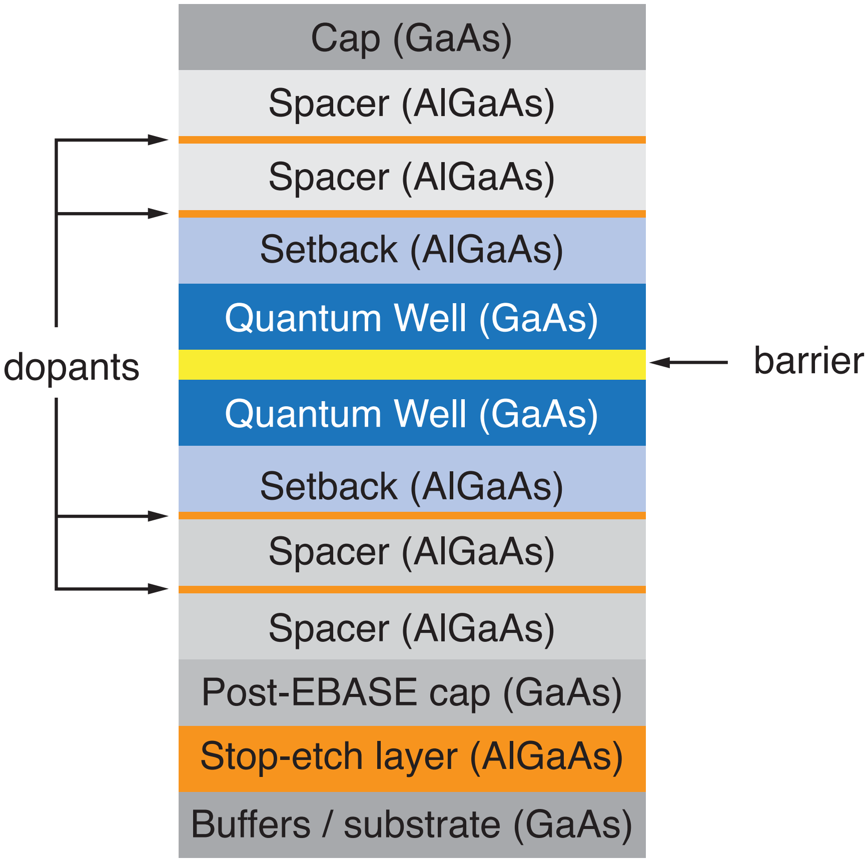

Fig. 5.1: Schematic of a generic double quantum well modulation-doped GaAs/AlGaAs heterostructure with a stop-etch layer. The width of the barrier separating both quantum wells can be adjusted during the growth process and can be as thin as one epitaxial layer. In a typical heterostructure, the aluminum concentration of the barrier is 30%.

allows to smooth out through chemical etching any unevenness arising from the mechanical lapping of the heterostructure. The thinner layer is made out of GaAs and its purpose is two-fold. Firstly, it acts as an additional stop-etch layer during the chemical etching of the first stop-etch layer. Secondly, it also serves as a capping layer protecting the AlGaAs spacers from oxidation once the EBASE process is completed. The specific details of the EBASE process will be presented in the next section.

5.2 Cleanroom Processing Details

In this section, I provide a step by step description of the fabrication process of vertically-coupled quantum wires. All the technical details concerning the tools and the recipes used are given in appendix A. Many iterations of the fabrication process have been required to successfully fabricate these devices and only the finalized procedure will be presented here.

Starting with a double quantum well heterostructure with a stop-etch layer, the wafer is cleaved into 6 mm × 9 mm pieces using a diamond-tip scribe. These pieces are then cleaned using acetone, methanol and isopropanol (in that order) for $\sim$ 15 s for each solvent. It is important to always rinse the acetone with methanol and isopropanol as acetone leaves residues on GaAs that would likely affect the subsequent processing. Following the cleaving, a mesa structure is etched on each piece. The mesa structure mask is defined using positive photolithography and the etch is carried out using phosphoric acid, as described in appendix A. The etch should be deep enough to prevent conduction outside of the mesa structure and must therefore be deeper than both quantum wells depth,[1] yet shallow enough as to not etch the stop-etch layers. In typical structures, a $\sim$ 2000 $\AA$ deep etch is sufficient to ensure that conduction can only occur within the mesa structure. The mesa pattern

---

[1] Surface depletion might allow the etch to be more shallow, but it is safest if the etch goes through both wells.

defines three independent sections; therefore three different coupled-quantum wires devices are fabricated on each GaAs/AlGaAs wafer piece, minimizing the risk of having a chip with no working devices. A schematic of the mesa is shown in figure 5.2.

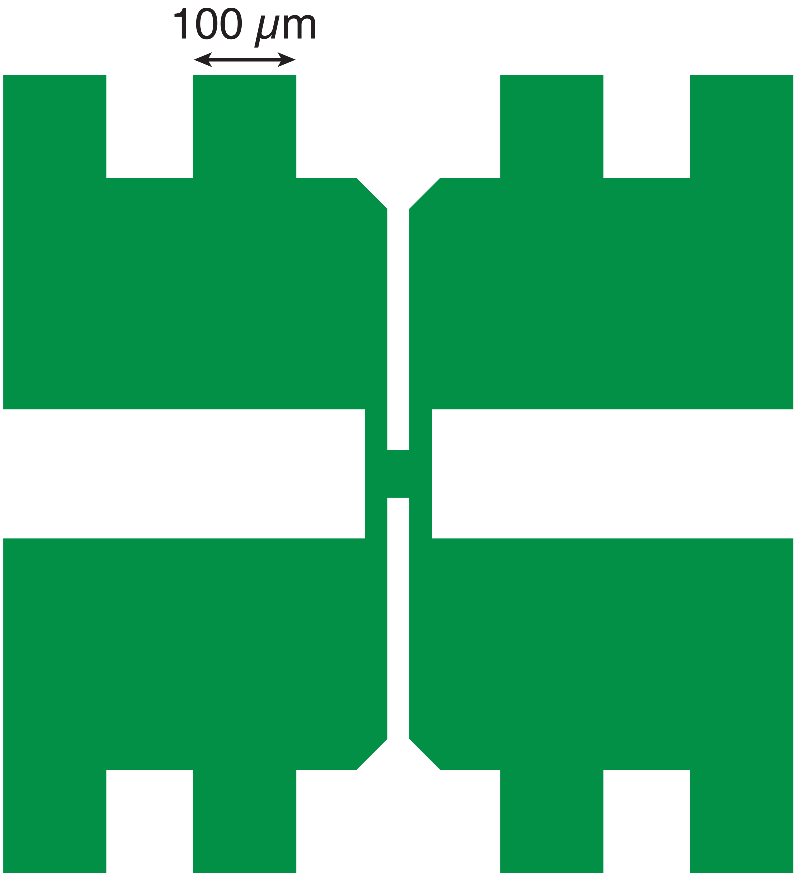

Fig. 5.2: Schematic of the mesa structure used to fabricate the vertically-integrated quantum wires. Conduction can only occur within the green sections of the figure as the 2DEG has been etched out elsewhere (white sections). On a typical chip, three such mesa structures are defined.

Following the mesa etch, ohmic contacts are deposited on the structure to electrically connect specific regions of the 2DEG. The mask used to deposit the ohmic contacts is defined with photo-lithography. Then, using e-beam evaporation, a stack of Ge/Au/Ni/Au of thickness 260 $\AA$ / 540 $\AA$ / 140 $\AA$ / 1500 $\AA$, respectively, is deposited on top of the structure.[2] The structure is then soaked in acetone for at least 4 hours to lift up the metal and, after a solvent rinse, the ohmic contacts are annealed at 420°C for 60 seconds following the procedure outlined in appendix A. The annealing process is required for the metal to diffuse through the heterostructure and thus electrically connect the 2DEGs.

Once the ohmic contacts are fabricated, a set of large electrostatic split-gates are deposited on top of the structure. The mask used to define these gates is once again achieved with positive photo-lithography and a Ti-Au (150 Å/ 1500 Å) stack is deposited over the mask using e-beam evaporation and standard lift-off procedures. In addition to the split-gates, a set of alignment marks is simultaneously deposited on the structure to allow for a careful alignment of the upper wire, which will is defined using e-beam lithography.

This upper quantum wire, however, is not defined at the same time as the photo-lithographically defined section of the gates since the photo-lithographic resolution is not precise enough to fabricate a quantum wire with a 500 nm width. The large portion of the gates defining the quantum wire are made separately from the finer portions because of the following reasons. Firstly, it is much faster to create a large *in situ* polymer mask using photo-lithography than it is using e-beam lithography. Also, e-beam lithography might damage

---

[2] For more details concerning the e-beam evaporation, see appendix A.

the 2DEG owing to the high energy electron beam impacting the heterostructure. Therefore, limiting the exposure to the electron beam to a small area minimizes the risks of degrading the 2DEG quality. A top view of the different fabrication steps taken up to this point are shown in figure 5.3. From the figure, it can be seen that the gates and the ohmic contacts expand far away from the mesa structure, connecting it to large soldering pads for easy wire bounding.

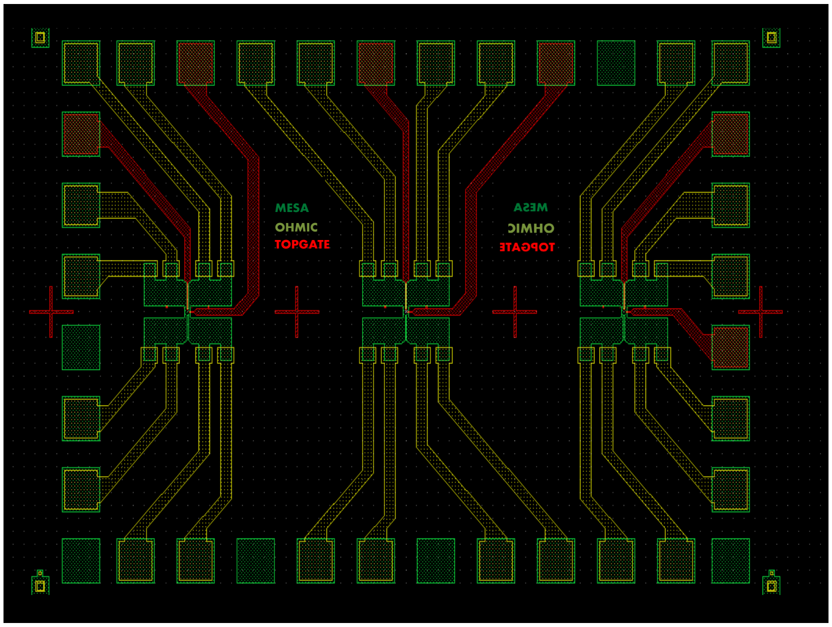

Fig. 5.3: Schematic of the top view of a device once the large split-gates are deposited, yet prior to the upper wire definition. The mesa structure is shown in green, the ohmic contacts in yellow and the upper gates in red. The large red crosses are alignment marks enabling alignment of the e-beam defined section of the gates together with the section made using photo-lithography.

The last fabrication step that is performed prior to the EBASE procedure is the fabrication of the upper quantum wire using e-beam lithography. The lithographic dimensions of the wire are designed to be 5 μm long and 0.5 μm wide and the e-beam lithography is performed with a LEO 440 SEM fitted with the Nanometer Pattern Generation System (NPGS) software. This software allows one to remotely control a commercial scanning electron microscope (SEM) and use it as an e-beam lithography tool.[3] Before performing the lithography, 495 C-4 PMMA is spun on the sample at 5000 rpm for 30 seconds and then baked at 175°C for 15 minutes. Following the e-beam lithography, the PMMA is developed using MIBK : IPA in a ratio of 1 : 3. Finally, e-beam evaporation along with standard lift-off procedures are used to deposit a 100 $\AA$ / 500 $\AA$ stack of Ti-Au, forming the upper quantum wire. At this point of the fabrication process, half of the device is completed and a single quantum wire is present on the top of the structure. The design of this wire is shown in figure 5.4. The design includes two gates : a large T-shaped pinch-off gate, permitting to achieve independent contacts to both layers, and a smaller plunger gate, allowing to control the 1D subband occupancy of the quantum wire. In addition to the quantum wire itself, a set of cross-shaped alignment marks is deposited. These marks are used when the lower quantum wire is deposited on the structure (using the same design, but rotated by 180°) so as to align it with the previously defined upper wire.

The EBASE procedure begins once the upper wire is fabricated. The first step is to cleave and clean with solvents a piece of bare GaAs with a size ~ 1 mm larger than the original heterostructure in length and width. Using EPO-TEK 353 ND, a two-component epoxy, the bare GaAs is then glued on top

---

[3] For more details, please consult appendix A.

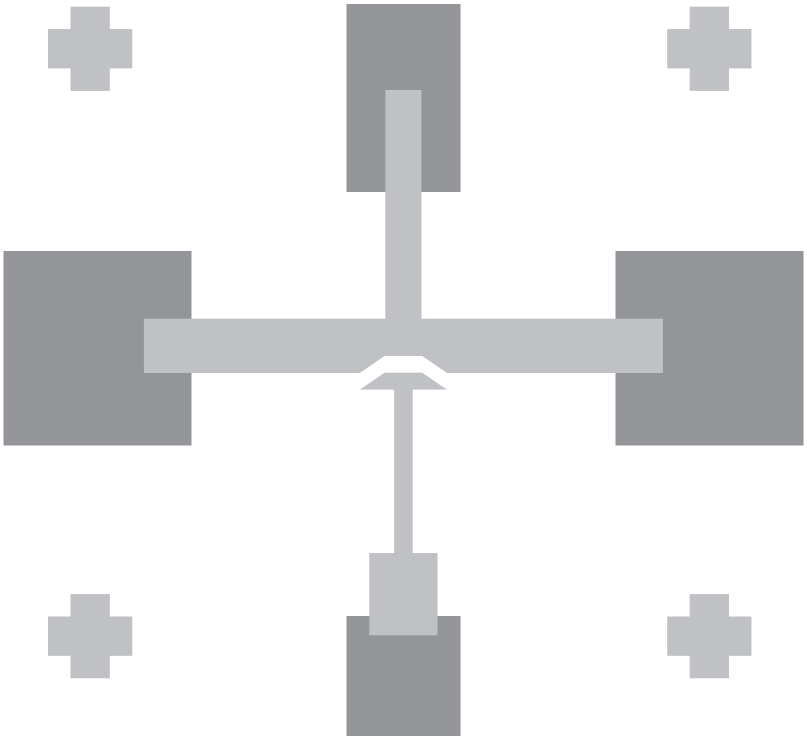

Fig. 5.4: Design of a single quantum wire in the vertically-integrated double quantum wire geometry. This design includes two gates: a large T-shaped pinch-off gate allowing to achieve independent contacts to both layers and a smaller plunger gate allowing to control the 1D subband occupancy of the wire. Cross-shaped alignment marks are also included in this design.

of the device and cured at 130° C for 60 minutes. At this point, the device is flipped and the original substrate is mechanically lapped until $\sim 600\ \mu$m of material has been removed. The lapping is performed using a Buehler minimat tool and is carried out in two steps : a first step removing $\sim 525\ \mu$m of material using a grade 240 sand paper, and then a second one removing $\sim 75\ \mu$m of material using a 600 grade sand paper. This two-step process ensures that the surface is as smooth as possible once this fabrication process is over.[4]

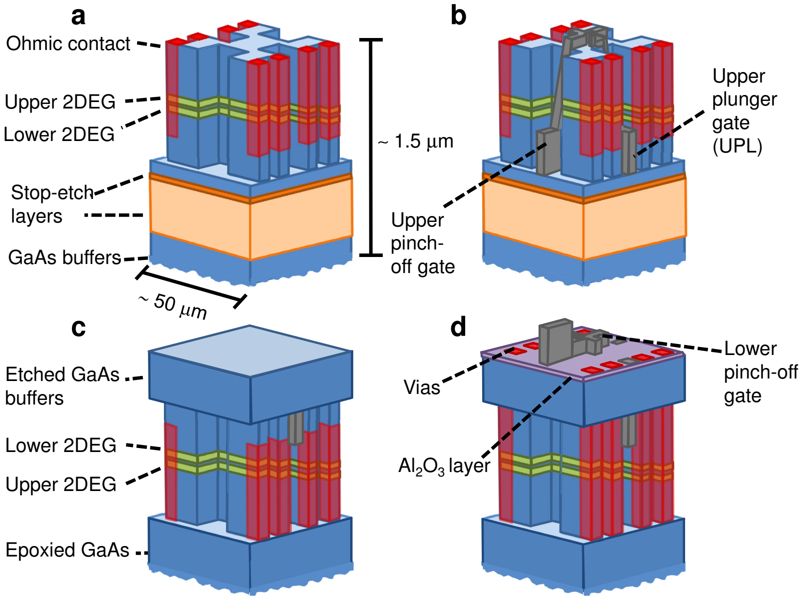

Fig. 5.5: **(a)** Diagram of the double quantum wires device subsequent to mesa etching, and the Ge-Au-Ni-Au ohmic contacts deposition and annealing. For clarity, the scale bar in the x-y direction (50 μm) is dramatically larger than in the z-direction (1.5 μm). **(b)** Diagram showing the deposited upper pinch-off and plunger Ti-Au gates. The off-mesa section of the gates is patterned using photo-lithography while electron-beam lithography is used to define the on-mesa gates. **(c)** Diagram after the epoxy-bond-and-stop-etch (EBASE) procedure. Note that due to a flipping process following the new substrate bonding, the upper 2DEG is now at the bottom. Similarly, the upper gates are now buried between the mesa and the epoxied GaAs. The original substrate has been lapped and etched down to $\sim$ 300 nm. **(d)** Diagram showing the final layout of the double quantum wires device after an Al_2O_3 insulating layer is deposited, with vias etched through the device to connect the upper gates and the ohmic contacts to the surface, and another set of Ti-Au split gates deposited.

To further smoothen out the lower surface (which is now on top of the

---

[4] For more details, please consult appendix A.

device since the device has been flipped), the sample is then etched in citric acid and peroxide in a ratio of 5 : 1. Prior to the etching, the epoxied substrate is mounted on a glass slide using crystal bound to prevent its etching. Due to the stop-etch layer inserted during the growth process of the heterostructure, and also because citric acid etch rate is $\sim$ 100 times faster on GaAs ($\sim$ 600 nm per minute) than on AlGaAs, any unevenness that arose during the mechanical lapping is dramatically reduced by this etching process. After the etching, the heterostructure new surface is then smooth enough to reflect light and appears bright to the eye. The citric etch process takes between 45 and 90 minutes at a temperature of 65°C, depending on the exact quantity of material required to etch after the mechanical lapping. Once the citric etch is over, acetone is used to dissolve the crystal bound and remove the device from the glass slide.

In order to bring the new surface even closer to the lower 2DEG ($\sim$ 150 nm), the stop-etch layer itself is etched away, using hydrofluoric (HF) acid at a concentration of 45%. This etch is very fast and occurs at a rate of ~ 40 $\mathring{A}$ per second. Owing to all the etching process during the EBASE procedure, it has been found that pin-holes are likely to form on the structure outside the mesa. The presence of such pin-holes can undesirably electrically connect the upper gates buried under the new surface with the soon-to-be deposited lower gates. Such an electrical-short renders the device inoperable so, to avoid this possibility, a thin Al_2O_3 layer $\sim$ 50 nm thick is deposited using atomic layer deposition (ALD) after the HF etch.[5] Following this, a set of vias is fabricated

---

[5] The Al_2O_3 layer is deposited at 200° C using a Picosum R150 tool. For more details, consult appendix A. It is the only fabrication step that was not performed by the author of this thesis.

in the sample to connect the buried ohmic contacts and upper gates to the new surface. The size and position of these vias are defined using positive photo-lithography and two successive etches : a buffered-oxide etch (BOE) to etch the Al_2O_3 layer at a rate of ~ 15 $\mathring{A}$ per second and a phosphoric etch to etch the GaAs/AlGaAs heterostructure.

Following the vias etch, another set of gates is deposited on the device and is aligned with the upper gates buried underneath the surface using the previously deposited alignment marks. The misalignment occurring with the SEM used in the device fabrication is not uniform in both x-y directions, with an average misalignment of $\sim$ 25 nm in the direction perpendicular to the wires and an average misalignment of $\sim$ 1.5 μm in the direction parallel to the wires. While this parallel misalignment is relatively large, its main effect is to reduce the effective overlap between the quantum wires. However, very importantly, it does not affect the effective interwire separation such as the perpendicular misalignment would.

Figure 5.5 summarizes the fabrication process and shows a three-dimensional sketch of the device at various stage of the fabrication process. A photograph of a chip containing 3 devices with only the e-beam defined section of the lower wire missing is also presented in figure 5.6. Some large scale defects, consisting of base material that has not been etched away, are visible on the surface. In this chip, these defects prevent the definition of the lower quantum wire on the left-most device.

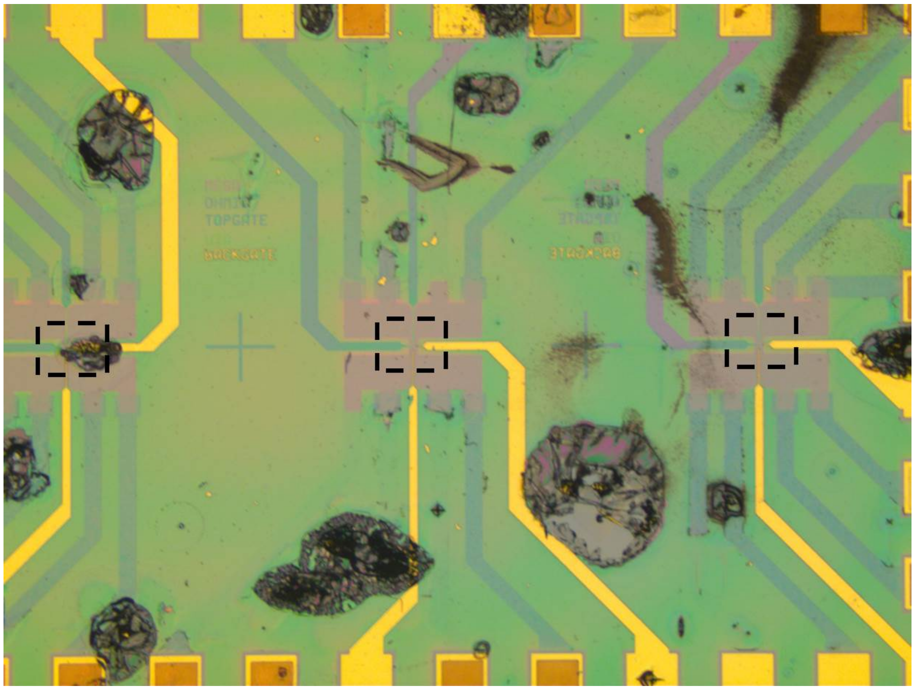

Fig. 5.6: Photograph of a vertically-coupled double quantum wires chip (3 potential devices) prior to the fabrication of the e-beam defined section of the lower wire. Some material has not been etched away during the EBASE procedure and is visible on the photograph. The regions where quantum wires are present are highlighted by dotted rectangles.

5.3 Design and Final Product

Using the fabrication process described above, several devices have been successfully fabricated in heterostructure EA0975, a double-quantum well heterostructure with a 15 nm wide barrier separating both quantum wells whose growth details are presented in figure 5.7. In these devices, the quantum wires are lithographically defined to be 500 nm wide and 5 μm long. The final design of the device is presented in figure 5.8 **(a)**. When a suitable electrostatic bias is applied to both the upper and the lower pinch-off gates (UPL and

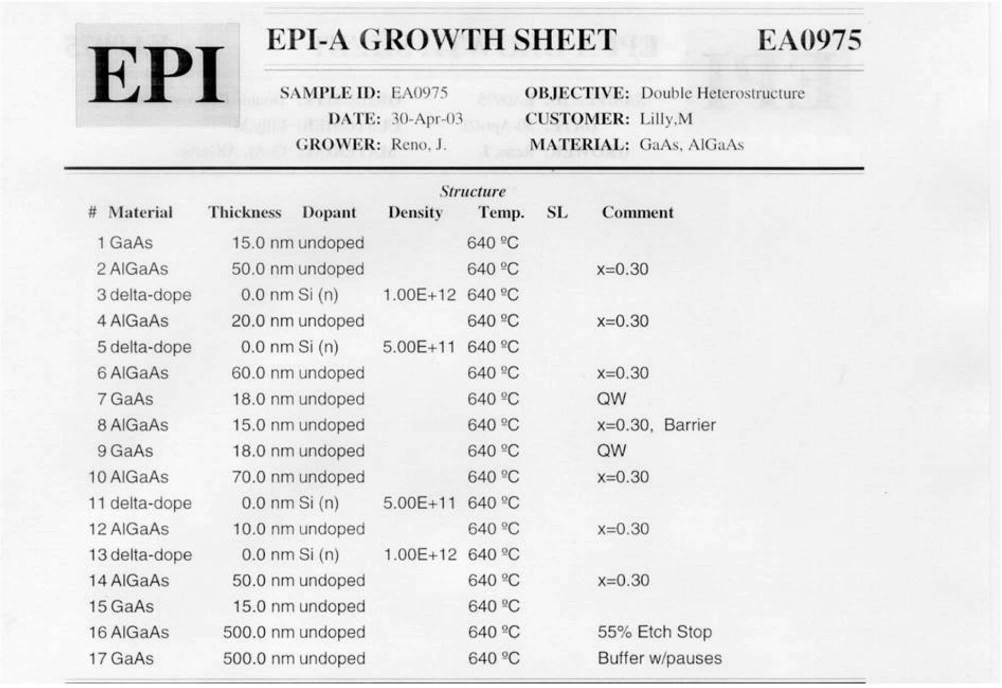

EPI

EPI-A GROWTH SHEET **EA0975**

SAMPLE ID: EA0975
DATE: 30-Apr-03
GROWER: Reno, J.
OBJECTIVE: Double Heterostructure
CUSTOMER: Lilly,M
MATERIAL: GaAs, AlGaAs

Structure

#	Material	Thickness	Dopant	Density	Temp.	SL	Comment
1	GaAs	15.0 nm	undoped		640 ºC		
2	AlGaAs	50.0 nm	undoped		640 ºC		x=0.30
3	delta-dope	0.0 nm	Si (n)	1.00E+12	640 ºC		
4	AlGaAs	20.0 nm	undoped		640 ºC		x=0.30
5	delta-dope	0.0 nm	Si (n)	5.00E+11	640 ºC		
6	AlGaAs	60.0 nm	undoped		640 ºC		x=0.30
7	GaAs	18.0 nm	undoped		640 ºC		QW
8	AlGaAs	15.0 nm	undoped		640 ºC		x=0.30, Barrier
9	GaAs	18.0 nm	undoped		640 ºC		QW
10	AlGaAs	70.0 nm	undoped		640 ºC		x=0.30
11	delta-dope	0.0 nm	Si (n)	5.00E+11	640 ºC		
12	AlGaAs	10.0 nm	undoped		640 ºC		x=0.30
13	delta-dope	0.0 nm	Si (n)	1.00E+12	640 ºC		
14	AlGaAs	50.0 nm	undoped		640 ºC		x=0.30
15	GaAs	15.0 nm	undoped		640 ºC		
16	AlGaAs	500.0 nm	undoped		640 ºC		55% Etch Stop
17	GaAs	500.0 nm	undoped		640 ºC		Buffer w/pauses

Fig. 5.7: Growth sheet of EA0975, a GaAs/AlGaAs double quantum well heterostructure with a 15 nm wide barrier separating both quantum wells. The heterostructure was grown by Dr. John Reno from the Center for Integrated Nanotechnologies (CINT) at Sandia National Laboratories.

LPL respectively), it selectively depletes the 2DEG closest to them, effectively connecting each quantum wire via different and independent ohmic contacts. For instance, as sketched in figure 5.8 **(b)** and **(d)**, given a suitable bias on the pinch-off gates, the lower wire (on top of the device due to the flipping process during the fabrication) is only connected through to ohmic contacts on the right side of the device and, similarly, the upper quantum wire is only connected to the left ohmic contacts. In this setup, it is then possible to adjust

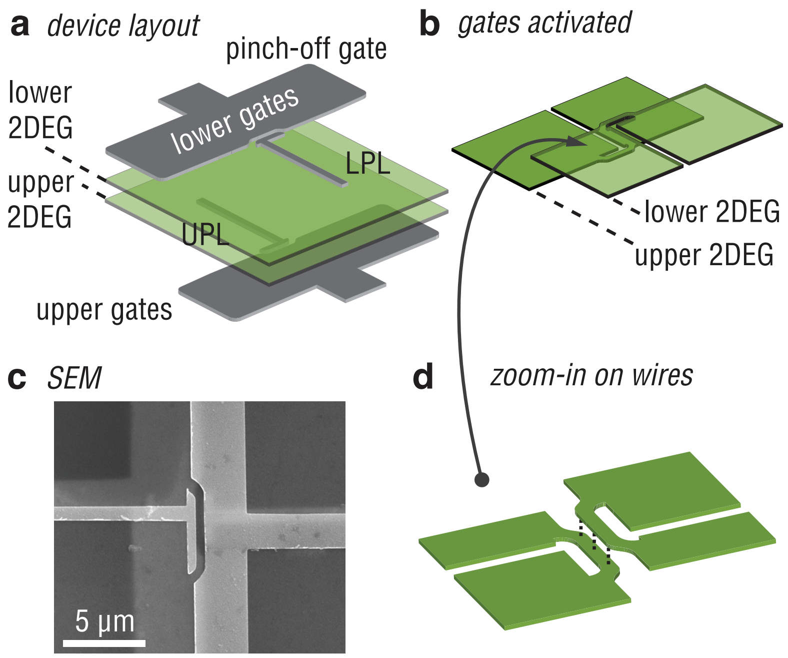

Fig. 5.8: **(a)** Schematic of the active part of the double quantum wires device. The EBASE process causes the lower gates and the lower 2DEG to be above the upper gates and 2DEG. **(b)** Schematic of the active part of the device when a suitable bias is applied on all four split gates, effectively coupling both circuits solely through one dimensional regions. The T-shaped pinch-off gates are simultaneously adjusted to deplete their respective 2DEG, effectively preventing any current flow in the section of the layer underneath (above) the lower wire (upper wire), and generating two independently contacted 2DEGs. Using the plunger gates, the two quantum wires are then formed. **(c)** Scanning electron microscope (SEM) photograph of a completed device (device 2-C). The lower plunger (LPL) and pinch-off gates are visible on the surface of the device. **(d)** Zoom-in on the interacting region of the device.

the subband occupancy of each quantum wire by varying the voltage applied to the plunger gates.

A SEM picture of a typical device is presented in figure 5.8 **(c)**. In this picture, the lower gates are visible on top of the device and appear as light tones of gray. Looking carefully, it is also possible to observed the upper gates buried underneath the surface, which appear faintly on the SEM picture. From this picture, it was determined that the wires have an effective lateral overlap of 2.7 μm and are aligned within 25 nm of each other in the direction perpendicular to the wires. This particular device, labeled 2-C, is the device that has been used to perform the Coulomb drag measurements presented in the next chapter of this thesis. Device 2-C, along with two similar devices, has also been used to measure the temperature dependence of 1D Coulomb drag presented in chapter 7 of this thesis.

References

[1] Laroche, D., Bielejec, E. S., Reno, J. L., Gervais, G., and Lilly, M. P. *Physica E* **40**, 1569 (2008).

[2] Weckwerth, M. V., Simmons, J. A., Harff, N. E., Sherwin, M. E., Blount, M. A., Baca, W. E., and Chui, H. C. *Superlatt. Microstruct.* **20**, 561 (1996).

6

Quantum Transport and Coulomb drag in Vertically-Integrated 1D-1D Devices

In this chapter, the initial characterization of the vertically-integrated quantum wires along with a study of the 1D subband dependency of the Coulomb drag signal is presented for independently contacted quantum wires with the closest interwire separation reported to date. After a description of the experimental setup, the initial conductance measurements performed on the quantum wires are presented. Then, a detailed study of the 1D Coulomb drag dependency on the subband occupancy is presented, as well as our discovery of a novel high-density negative Coulomb drag regime. This observation is *a priori* not readily explained by current Coulomb drag theories based on momentum-transfer models in single channel quantum wires. Possible explanations with alternative theories describing the Coulomb drag as a result of energy fluctuations of electron and holes in mesoscopic circuits are presented.

6.1 Experimental Details

6.1.1 Device Details

The 1D subband dependency of the Coulomb drag signal has been performed in vertically-coupled quantum wires fabricated in wafer EA0975, a double quantum well heterostructure with a 15 nm wide barrier separating the quantum wells. A SEM picture of these wires was presented in figure 5.8 **(c)**. Both Van der pauwn and Shubnikov-De Hass measurements were performed in the device (after processing) in a helium-3 refrigerator with the split-gates grounded. These measurements yielded a two-dimensional electronic density of 1.1 (1.4) $\times 10^{11}$ cm^{-2} for the upper (lower) 2DEG, and a combined mobility (for both layers) of 4.0×10^5 cm^2 / V$\cdot$ s.

Determining the 1D density of the wires when a single 1D subband is occupied is difficult. Yet, an estimate can be made from the square-root of the 2D density.[1] Taking into consideration the slight vertical misalignment between the wires, we estimate the effective $2k_F d$ parameter to be bounded between 3.9 and 4.7, anchoring our device in a regime where phonon-drag would likely be negligible [2]. All the measurements presented in this section have been performed on a single sample (sample 2-C, wafer EA0975), and have been qualitatively reproduced over different coolings. Furthermore, these results were later reproduced in other devices (devices 3-R and 2-L, wafer EA0975). The results obtained with these other devices will be presented in chapter 7.

---

[1] This estimate yields a 1D density of 3.3 (3.7) $\times 10^7$ m^{-1} for the upper (lower) wire and is consistent with the 1D densities measured in tunneling experiments realized in similar heterostructures [1].

6.1.2 Helium-3 Refrigerator

The refrigerator used to perform the low-temperature measurements (in this chapter) is an Oxford Instruments ^{3}He sorption pumped system where the device is immersed in liquid ^{3}He. This refrigerator is top loading and is equipped with a sliding seal; allowing for quickly changing or thermally cycling the device. The refrigerator is installed within a 14 T superconducting magnet mounted in a typical ^{4}He dewar in a way that the device is in the center of the magnetic field. The magnet is powered using an Oxford Instruments IPS 120-10 power supply that can provide up to 120 A to the superconducting magnet. A schematic of this setup is shown in figure 6.1.

This refrigerator works as a single shot system, meaning that when the system is cold and not condensed, the ^{3}He gas is located in the sorb. At first, the ^{3}He is taken out of the sorb by heating it above 40 K. Once all the helium gas has been evacuated from the sorb, the temperature of the sorb is lowered and the ^{3}He condenses at the 1 K pot, provided that the 1 K pot temperature is below $\sim$ 1.6 K. The liquid ^{3}He then collects inside the ^{3}He pot and the cold sorb can act as a pump for the ^{3}He liquid, lowering its temperature down to $\sim$ 330 mK. For this refrigerator, the hold time of the condensed ^{3}He is approximately 9 hours. Both a germanium and a 470 Ω calibrated Speer resistors are used to measure the temperature of the ^{3}He pot. Assuming thermal equilibrium with the device, a reasonable assumption, these thermometers also measure the temperature of the device. The thermalization of the sample with the ^{3}He pot is consistent with the lack of saturation of the temperature dependence of the drag resistance down to the base temperature of the refrigerator, $\sim$ 330 mK.

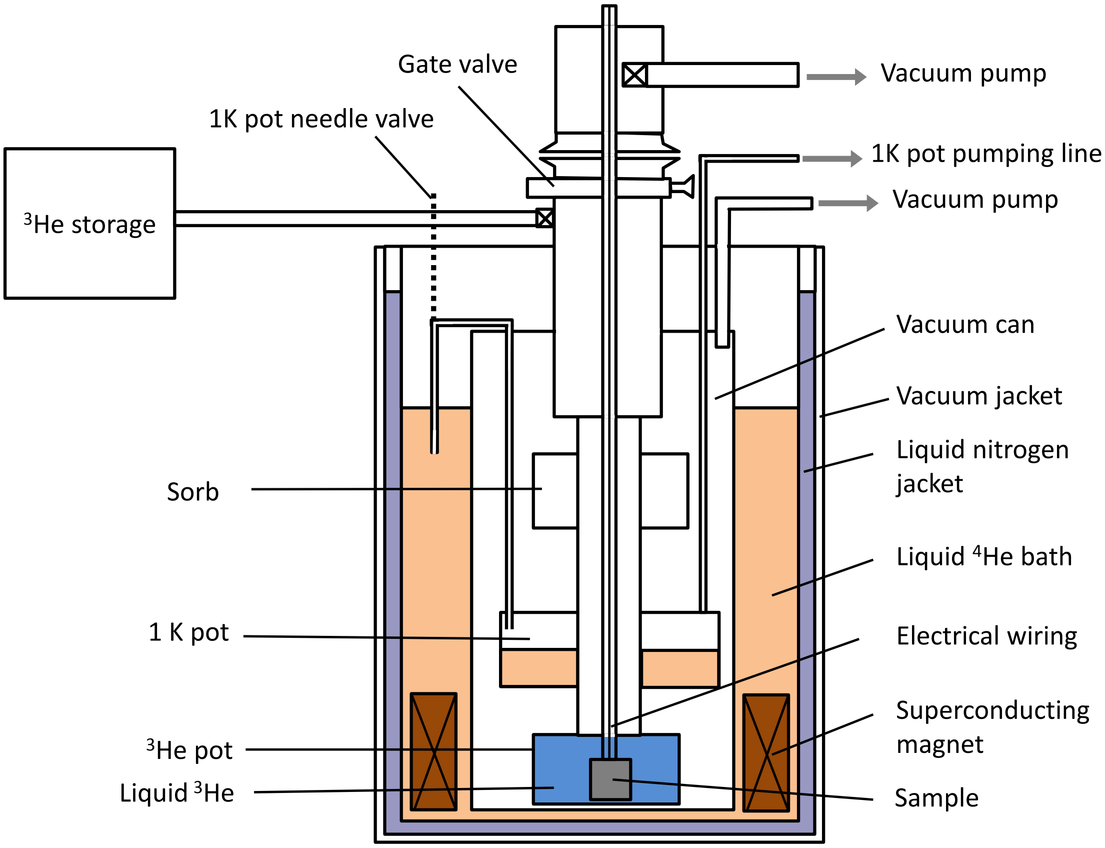

Fig. 6.1: Schematic of the helium-3 refrigerator used in this work.

The temperature of the 1 K pot is measured with a 470 Ω calibrated Speer resistor and the sorb temperature with a 270 Ω calibrated Allan Bradley resistor.

6.1.3 Measurement Setups and Schematics

The results from several different type of measurements are presented in this section, including conductance, tunneling and Coulomb drag measurements. All measurements are performed using standard low-frequency lock-in amplifier techniques at a frequency of either 9 Hz or 13 Hz. The lock-in amplifiers are Stanford SR 830 and are used to source and measure the AC signals. Unless otherwise specified, Keithley K-2400 source-measure units are used to source and measure DC signals, and E&G park model 113 voltage pre-amplifiers are used for both AC and DC voltage measurements. The current pre-amplifiers integrated with the SR 830 lock-in amplifiers are used to directly measure the AC currents.

In our experimental setup, great care was taken to ensure that no grounding loops existed, and that all devices were isolated. All instruments, wires, leads, etc. were used with grounded shielding whenever possible. The noise in the device is of the order of $\sim 50\ nV/\sqrt{Hz}$. This noise is principally preamp limited. In the regime where the experiment was performed (resistance of $\sim 20\ k\Omega$ and frequency of $\sim 10\ Hz$), the noise figure of the pre-amplifier is $\sim$ 3 db. Therefore, the noise arising through the use of the amplifier is given by $\delta V = 10^{3/20} \times gain \times \delta V_{Johnson} = 47.3\ nV/\sqrt{Hz}$, where the $gain = 100$ is the value of the gain of the pre-amplifier and where $\delta V_{Johnson} = \sqrt{4k_BTR}$ is the intrinsic Johnson (or thermal) noise per $\sqrt{Hz}$ with a measurement bandwidth $\Delta f = 0.833Hz$. The noise level of our measurement is thus comparable to the intrinsic noise of the voltage pre-amplifier, confirming that external sources of noise were properly controlled and are negligible.

Conductance Measurement Details

The circuit diagram for the conductance measurement is shown in figure 6.2. The (unbiased) interlayer resistance and the resistance of each layer

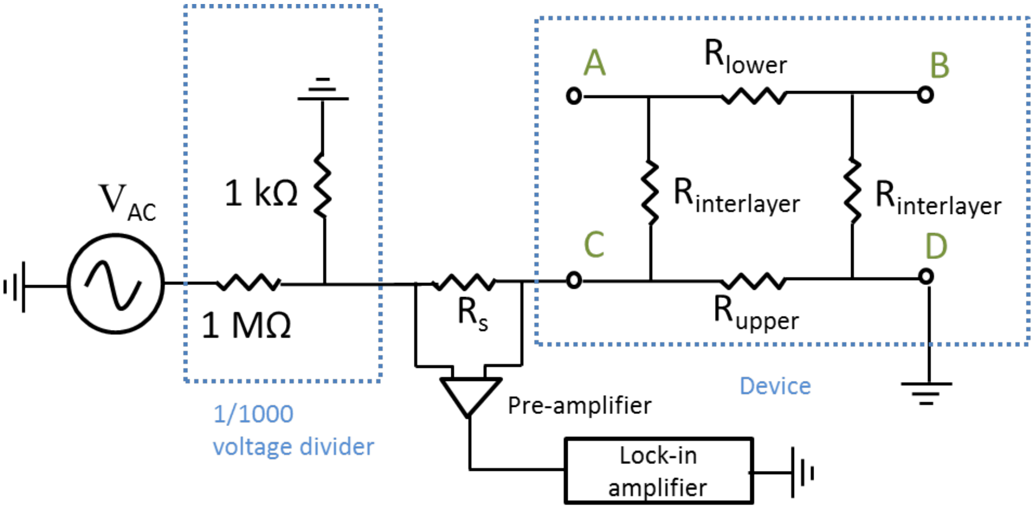

Fig. 6.2: Circuit diagram of the upper layer (or wire) conductance measurement. By changing the terminal at which the AC voltage (terminal C in this circuit) is sourced and the grounded terminal (terminal D in this circuit), it is possible to measure the conductance of the upper layer (C-D), of the lower layer (A-B) as well as the interlayer conductance (C-A). In a typical measurement, a sensing resistor R_s of 996 Ω is used and a net constant bias of ~ 50 μV is set across the DUT and the sense resistor.

(or wire, depending on the voltage applied to the split gates) is measured using a two-terminal geometry. In the configuration shown in figure 6.2, the conductance of the upper layer is being measured. However, changing the terminals at which the bias is applied and the grounded terminal (terminal C and D respectively in figure 6.2) allows us to measure the interlayer resistance (using terminals C and A, respectively) or the lower layer resistance (using terminals A and B, respectively).

In a typical measurement, a sensing resistor $R_s = 996$ Ω is used and a 50 mV bias is set across the circuit. This creates a ~ 50 μV drop across the sensing resistor and the device under test (DUT), as long as their combined resistance is much less than 1 MΩ. The exact voltage drop across the sensing resistance and the DUT is also measured before each measurement. The resistance across the DUT is then obtained from the value of the voltage drop across the sensing resistor, V_s. Following Ohm's law (V = RI), we obtain that $R_{DUT} = \frac{V-V_s}{V_s} \times R_s = G_{DUT}^{-1}$. The value of the DUT conductance is then converted in natural units of $2e^2/h = (12942)^{-1}\Omega^{-1}$ by multiplying the conductance by a factor of 12942.

Tunneling Measurement Details

A tunneling measurement can only take place when an appropriate bias is applied to both the upper and the lower pinch-off gates. The technique of choice to optimize these voltages will be presented in the following section. The tunneling measurements have been performed in two different ways, both yielding identical results (within error), as shown in figure 6.3. The circuit diagram for each of these setups is presented in figure 6.4 **(a)** and **(b)**.

Using the circuit presented in figure 6.4 **(a)**, the tunneling resistance is obtained by performing a numerical derivative of the DC I-V curve from a source-measure unit. In this setup, a DC voltage is set through the circuit and the resulting current is measured using the source-measure unit (a Keithley K-2400 in this case). The numerical derivative of this I-V curve yields the value of the tunneling resistance as a function of the bias voltage. This tunneling resistance can also be measured directly without resorting to numerical derivatives. To achieve this, one relies on the fact that a small AC voltage

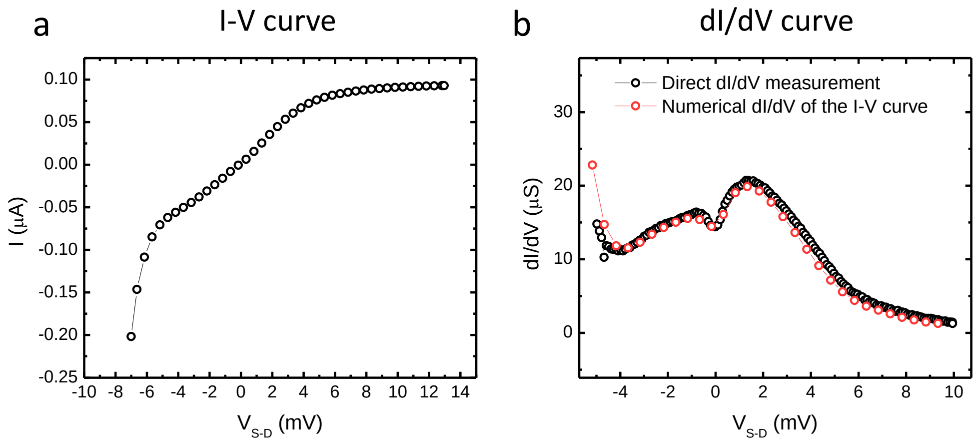

Fig. 6.3: **(a)** DC I-V curve of 2D-2D tunneling taken using a source-measure unit. **(b)** Comparison between the tunneling conductance measured directly using an AC dI/dV measurement (black curve) and between the numerical derivative of the I-V curve shown in panel **(a)**. Both schemes for obtaining the tunnel conductance yield identical results (within error).

superimposed on top of a DC bias naturally measures the derivative of the I-V curve. Such a technique is called a dI/dV measurement and the circuit diagram for this measurement scheme is presented in figure 6.4 **(b)**. Here, an Isomax isolation transformer[2] is used to cut the ground and superimpose the AC and DC signals together. The DC bias is measured using a digital voltmeter and the AC voltage and current signals are measured using a lock-in amplifier, together with a voltage and a current pre-amplifier, respectively. The tunneling resistance at a given voltage bias V_{bias} is then given simply by $R_{tunnel} = V_{AC}/I_{AC}$.

---

[2] This transformer has been found to be effective at frequencies $f > 1$ Hz.

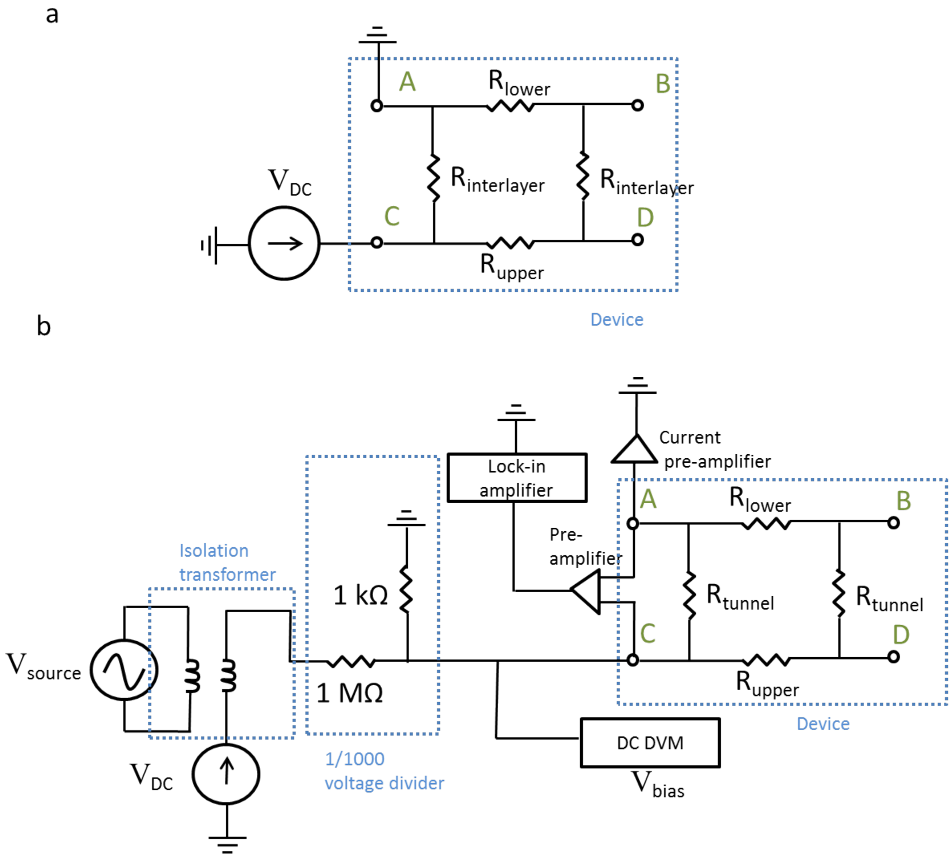

Fig. 6.4: Circuit diagram for the tunneling measurements. **(a)** This numerical derivative circuit only uses a source-measure unit setting a voltage across the circuit and measuring the resulting current. The numerical derivative of the resulting I-V curve is then calculated to obtain the tunneling resistance. **(b)** In this setup, the dI/dV tunneling resistance of the device is directly measured. An isolation transformer is used to superimpose a small AC signal on top of a DC signal. Then, for a given V_{bias}, the tunneling conductance is obtained by dividing the AC voltage across the device by the AC current sourced through the device.

Coulomb Drag Measurement Details

When all the split gates of the device are biased in a way such that the tunneling resistance between both wires is large enough ($R_{tunnel} \geq 10\ M\Omega$), tunneling is negligible and it is then possible to perform Coulomb drag measurements. In figure 6.5, two different setups used to measure Coulomb drag are shown.

The setup presented in figure 6.5 **(a)** is the simplest setup to perform a Coulomb drag experiment. A constant current of 4.5 nA is sourced through the drive wire (terminal C and D) (produced using a constant voltage source in series with a 11 MΩ resistance) and measured using a current pre-amplifier. Simultaneously, the voltage drop is measured across the drag wire (terminal A and B) while the wire is grounded through the voltage pre-amplifier. We caution however that using such a simple setup, an effective bias may develop between both wires, arising from a different grounding point across the wires, which could affect the Coulomb drag signal.

Therefore, the Coulomb drag signal has also been measured using a symmetric circuit where a virtual ground is added to each circuit so as to ensure that each quantum wire is at an effective zero bias. Such a circuit is shown in figure 6.5 **(b)**. Here, two 5.5 MΩ resistors placed on both sides of the DUT are used to create a 4.5 nA constant current. Rather than measuring the drive current using a current pre-amplifier, here it is measured using a 10 kΩ sensing resistor. An isolation transformer is once again used to break the ground and a new grounding point is manually inserted in such a way that the drive wire lies at zero bias at midpoint. Similarly, the drag circuit is made symmetric and a grounding point is manually set so that the drag wire also lies at zero bias at midpoint.

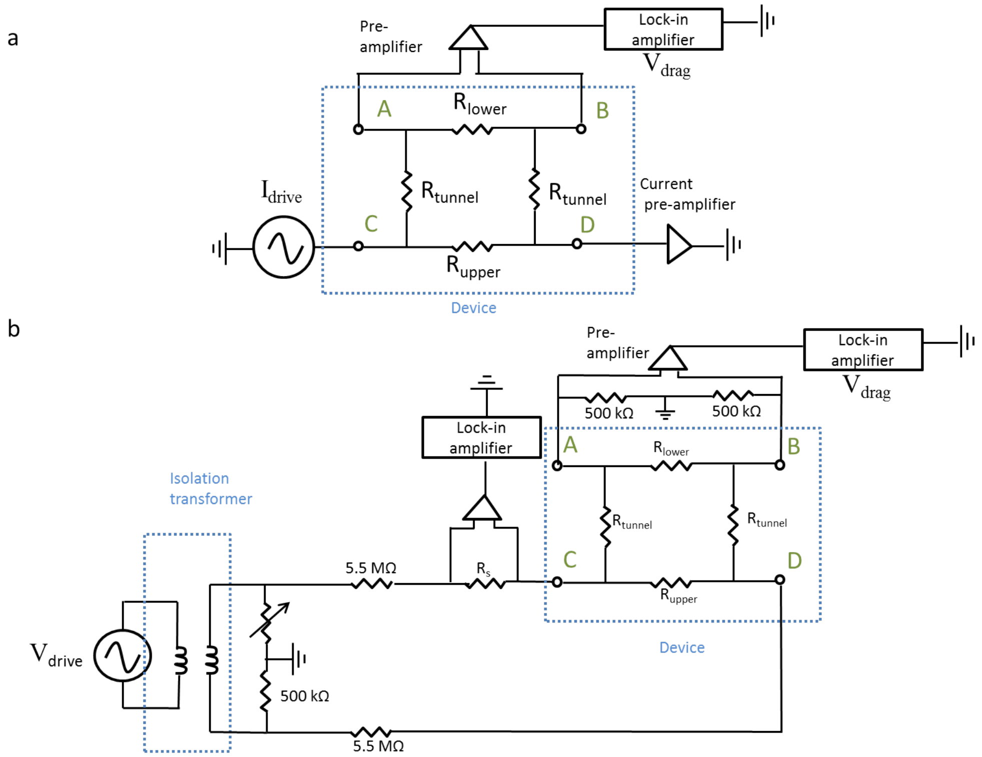

Fig. 6.5: Circuit diagram for the Coulomb drag measurements. **(a)** This Coulomb drag setup simply consists of sourcing a constant current through the drive wire and of measuring the resulting voltage drop in the other wire. The drag wire in which the voltage drop is measured is grounded through the voltage pre-amplifier and both contacts A and B are left floating. **(b)** In this Coulomb drag setup, special care is taken to ensure that each layer is identically grounded and that each circuit is symmetric. In this case, the drive current is measured using a sensing resistor. Symmetry can be achieved by adjusting the value of the variable resistor in a way that each branch of the circuit has an identical resistance. The drag wire midpoint is set to zero bias by virtue of a virtual ground. It was found that the drag signal measured using circuit **(a)** and **(b)** were practically identical, with an offset of only a few hundredth of volts.

Despite all the precautions taken to form a truly symmetric circuit, the Coulomb drag signal was found to be almost identical using either circuit. Only a small shifting of the Coulomb drag versus LPL voltage curve by at most a few hundredth of volts was observed, due to the wires in setup **(a)** having a small non-zero bias (a few hundredth of volts at most), resulting in the circuit experiencing a slightly larger effective LPL and/or UPL bias. Therefore, for most of the Coulomb drag measurements presented in the remainder of this thesis, the simple circuit shown in figure 6.5 **(a)** was used.

6.2 Conductance and Tunneling Measurements

6.2.1 Pinch-Off Gates Optimization

Prior to performing one-dimensional Coulomb drag measurements, it is of paramount importance to characterize the wires that are used to carry out these measurements. The first step is to determine the appropriate bias that needs to be applied to both T-shaped pinch-off gates to create the independently contacted layers in which independent quantum wires are defined. To achieve independent contacts to each layer, the device has to be operated with the PO gates biased so as to effectively cut conduction across the 2DEG on the opposite side of the wires. The value of these biases are determined by sweeping the voltage applied on both pinch-off gates subsequently in two directions, *i.e.* perpendicularly to the wires direction (terminals C-A in figure 6.2) and in the upper (lower) wire direction for LPO (UPO) (terminals C-D (A-B) in figure 6.2). The result of such a gate sweep is shown in figure 6.6.

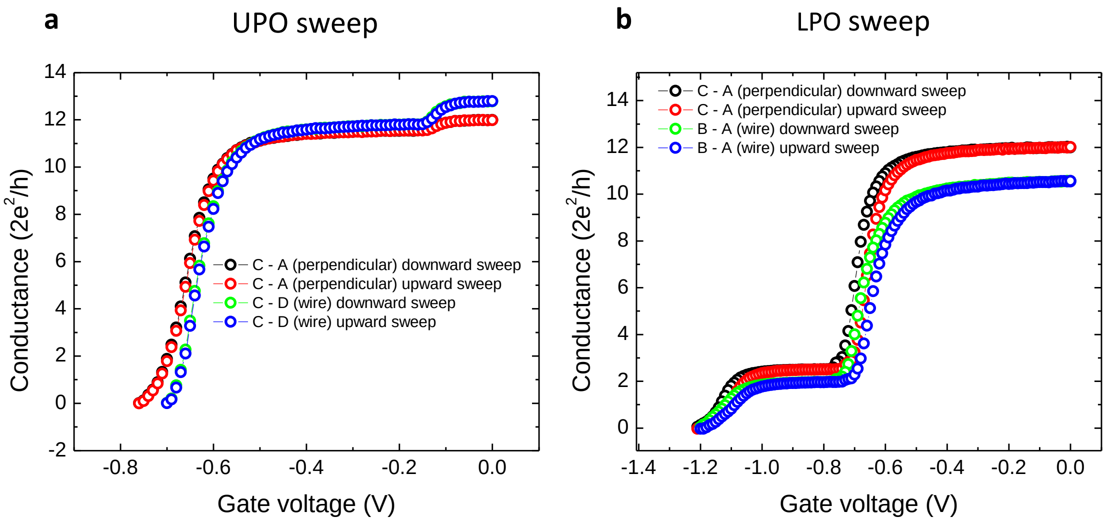

Fig. 6.6: Conductance of the coupled 2DEGs in the direction perpendicular to the wires (terminals C-A in figure 6.2 and black and red curves) and in the wire direction (green and blue curves) as a function of gate voltage for **(a)** the upper pinch-off gate, and **(b)** the lower pinch-off gate. Each voltage sweep is performed in both directions (from positive to negative voltage, and the reverse) to account for the possibility of hysteresis in the device. These data have been taken in device 2-C from wafer EA0975.

For each voltage sweep, the conductance is maximal at low bias and it drops with decreasing gate voltage until a "step" is reached. Past this point, the conductance remains nearly constant with gate voltage until a sufficiently negative bias is applied to the gates. Then, the conductance drops once again with decreasing gate voltage until the device is completely pinched-off. The conductance steps in these sweeps occur when the gate voltage is such that the 2DEGs closest to the gate is depleted and conduction can only occur through the 2DEG farthest from the biased gate. Therefore, by adjusting the bias of each pinch-off gate such that it lies on a conductance step, one can effectively create two independent 2DEG regions. We stress that observing a conductance step at the same bias in the direction parallel and perpendicular to the wires is essential for the good operation of the devices. Indeed, a reduced wire conductance or a decrease in the tunneling resistance would be observed if both steps were to occur at different gate voltages.

From the conductance value of these steps, it is easily noticeable that the layers do not have identical conductances. In this device, the lower layer is more conducting than the upper layer with a conductance of $\sim 11.5 \times 2e^2/h$, as opposed to $\sim 2.5 \times 2e^2/h$ in the upper layer (as can be seen in figure 6.6 **(a)** and **(b)** respectively). This relative large conductance difference between both layers is reflected on the individual wire conductances.

Another noteworthy feature is the presence of a slight hysteresis occurring during the LPO voltage sweep, most likely caused by charges accumulation in the dielectric layer. While the presence of such an hysteresis is not desirable, it only occurs for voltage bias resulting in a rapid change in the conductance across the device. Since the pinch-off gates are usually operated at a constant voltage in a way that the conductance across the device lies on a step where no hysteresis is observed, this hysteresis is not expected to affect the data in any significant way.

6.2.2 2D Tunneling Measurements

As mentioned previously, the device has to be operated with the PO gates biased so as to effectively cut conduction across the 2DEG on the opposite side of the wires to achieve independent contacts to each layer. Owing to a capacitive coupling between each PO gates, two potential pitfalls can occur when determining the optimal voltage bias to apply on the PO gates. If the applied voltages are too negative, the conduction in the wire direction will be severely reduced, effectively reducing the number of accessible 1D subbands once a quantum wire is created. However, if the applied voltages are not negative enough, parasitic 2D tunneling will be present in the device, which is far from desirable. Therefore, the value of the biases applied to each PO gate have to be optimized for maximal conductance in the wire direction while maintaining a sufficiently high tunneling resistance. The result of this optimization process yields a tunneling resistance larger than ~ 10 MΩ between both layers. We use transport measurements, described below, to determine the appropriate operating voltages.

Using gate voltages for which the layer conductances are on a step, 2D-2D tunneling measurements have been performed in the device with increasingly negative biases applied on the PO gates. This was done until a sufficiently small tunneling conductance was measured. An example of such 2D-2D tunneling measurements is shown in figure 6.7 where PO gate voltages of - 0.80 V and -0.19 V applied on LPO and UPO have been selected as the appropriate voltage biases (purple curve). This procedure is performed for each thermal cycling of the device as the resulting optimal gate voltages, while similar, still slightly change from cooling to cooling.

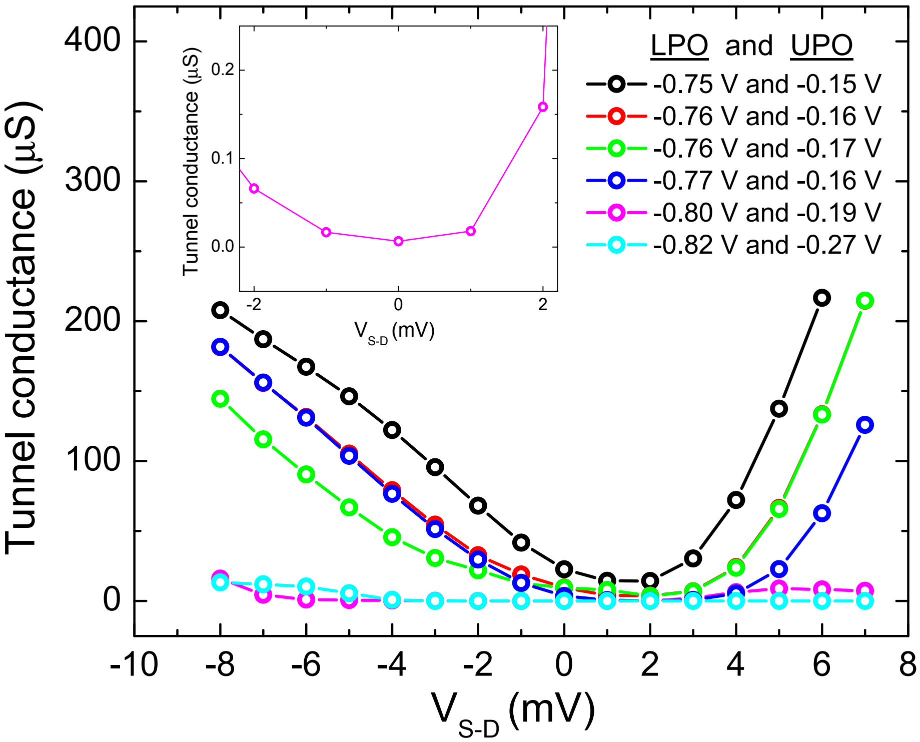

Fig. 6.7: Example of a 2D-2D tunneling measurement where the tunneling conductance is plotted against the source-drain bias across the tunnel barrier for various PO gate voltages. The optimal bias is selected to be the least negative bias for which the tunneling resistance is larger than ∼ 10 MΩ (or equivalently, the tunneling conductance is smaller than ∼ 0.1 μS). A zoom-in the low tunneling conductance region is shown in the inset. These data have been taken in device 2-C from wafer EA0975.

6.2.3 Wires Conductance Characterization

Once the tunneling optimization procedure is over, it is possible to measure the conductance of each quantum wire formed when their respective plunger gate is activated (as long as a suitable bias is applied to both pinch-off gates). The plunger gates have two peculiar characteristics. First, varying the bias applied to the upper plunger gate affects the conductance of the upper wire more strongly than the lower plunger gate affects the conductance of the lower wire. This behavior is somewhat expected since an Al_2O_3 layer electrically shields the voltage applied on the lower plunger gate from the 2DEGs. Second, both gates are capacitively coupled and varying the bias applied on a single gate will affect the conductance of each quantum wire. Therefore, the conductance in both quantum wires is measured by sweeping the lower plunger gate only (LPL) while keeping the upper plunger gate (UPL) at a fixed value. A typical example of such a conductance measurement is shown in figure 6.8.

During the measurement, the conductance of both wires is measured simultaneously using two lock-in amplifiers set at different frequencies (9 Hz and 13 Hz), and it has been verified that this simultaneous measurement does not modify the conductance of the wires. Plateau-like features are clearly observed in the raw data of the lower wire (light green curve) and the upper wire (light blue curve), as expected from Landauer formalism. These plateau-like features are observed at non-integer values of $2e^2/h$, implying that the wires are non-ballistic. Once the two-point conductance of the wires is corrected by subtracting a series resistance from the measuring circuit (1.25 kΩ for the lower wire and 5.00 kΩ for the upper wire, as per the resistance of each individual 2D layer), these plateau-like features are still occurring at non-integer values of $2e^2/h$. However, an even conductance spacing between the plateau-like features for both the lower and the upper wire is observed after the series-resistance substraction ($\Delta G_{lower} = 0.61 \pm 0.02$ and $\Delta G_{upper} = 0.37 \pm 0.03 \times 2e^2/h$ respectively). This even conductance spacing of plateau-like features at values lower than $2e^2/h$ in quasi one-dimensional

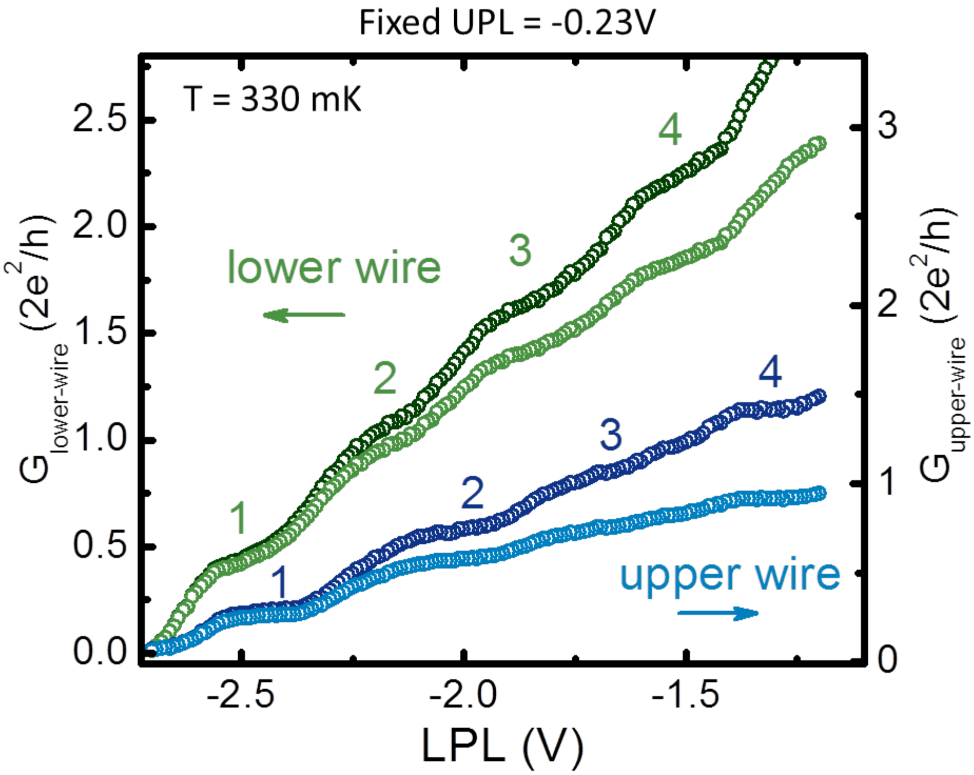

Fig. 6.8: Example of the conductance of the lower (green curves, left axis) and the upper (blue curves, right axis) quantum wires. In addition to the two-terminal conductance data shown in light color shades, the corrected conductance for each quantum wire is presented in darker color shades, where a 1.25 kΩ (5.00 kΩ) series resistance was subtracted from the lower (upper) wire conductance. Plateau-like features are clearly visible for each quantum wire, albeit disorder-broadened. These data have been taken in device 2-C from wafer EA0975.

structures has been previously observed [3], and it was found not to alter the formation of well-defined 1D subband in the wires.

The data in figure 6.8 shows the conductance of each quantum wire when only LPL is varied and UPL is kept fixed. By varying the voltage applied on UPL as well as on LPL, it is possible to obtain a mapping of the 1D subband occupancy for each quantum wire. Such a mapping is shown in figure 6.9 **(a)** and **(b)** where the derivative of the conductance of the upper and lower wire is plotted versus UPL and LPL gate voltages.

The data clearly shows the presence of plateau-like features. Indeed, the derivative of the conductance reaches a near-zero value whenever a plateau-like features is formed, regardless of the specific value of the conductance at this point. These appear as black and blue stripes in the mapping and they can be easily tracked over a large range of gate voltages. This, combined with the even conductance spacing of the plateau-like features, strongly support the existence of well-formed one-dimensional subbands in our wires. This mapping also shows that it is possible to achieve various regimes for the subband occupancy of the wires, ranging from a regime where both wires have very similar 1D subband occupancies to one where their subband occupancies are heavily mismatched. Finally, we note that even when the 1D subband occupancy in the wires is nearly identical, the wires themselves are not entirely identical since their conductance values differ, as can be seen in figure 6.8.

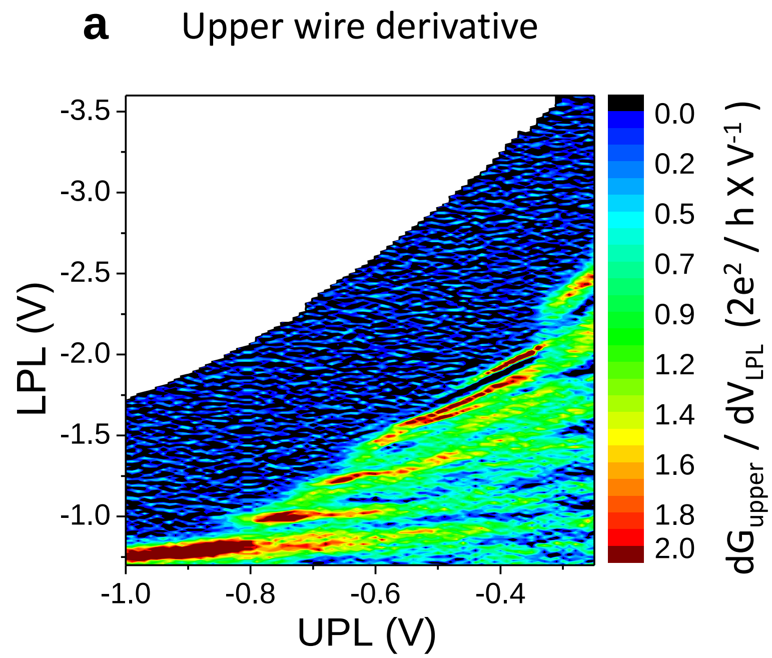

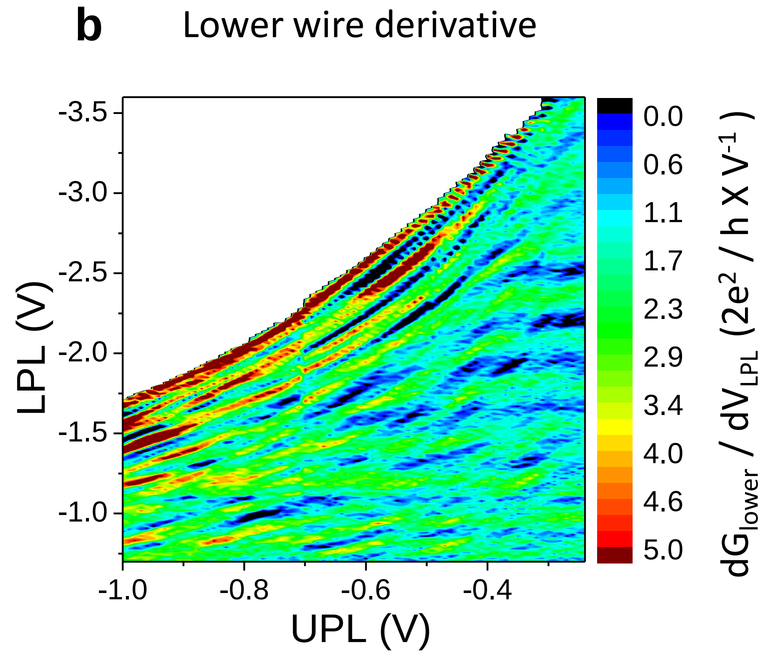

Fig. 6.9: Derivative of the conductance as a function of LPL voltage for **(a)** the upper quantum wire and **(b)** the lower quantum wire. Conductance plateau-like features appear as black and blue stripes in the figure. These data have been taken in device 2-C from wafer EA0975.

6.3 Dependence of the Drag Signal on the 1D Subband Occupancy

Once the bias voltage applied to the pinch-off gates are optimized and the quantum wires are characterized, Coulomb drag measurements can be performed in the device. The first measurement to be performed is a mapping of the signal versus the 1D subband occupancy of each quantum wire. Before presenting these results, we will first present the consistency tests performed to ensure that the signal we were measuring was indeed Coulomb drag.

6.3.1 Consistency Tests for the Coulomb Drag Measurement

We performed five different tests to verify that the signal we were measuring in this experiment was indeed Coulomb drag. These are *i)* negligible tunneling, *ii)* linearity of the drag voltage with drive current, *iii)* frequency independence, *iv)* probe symmetry (the measurement is the same using I_{drive}^{C-D} and I_{drive}^{D-C}, as defined in figure 6.5) and *v)* satisfaction of Onsager relations (using I_{drive}^{C-D}, V_{drag}^{A-B} is equivalent to using I_{drive}^{A-B}, V_{drag}^{C-D}). While all five of these tests are expected to hold within a momentum-transfer description of Coulomb drag, the probe symmetry and the Onsager relations might be broken within a charge-fluctuation description of Coulomb drag [4–6].

i) Negligible tunneling

In order to verify that the tunneling was negligible in our Coulomb drag measurement, we have performed a simulation of the tunneling signal strength using the electronic circuit for the tunneling measurement presented in figure 6.4 **(a)** and compared these results with the Coulomb drag signal we were measuring. This comparison is shown in figure 6.10.

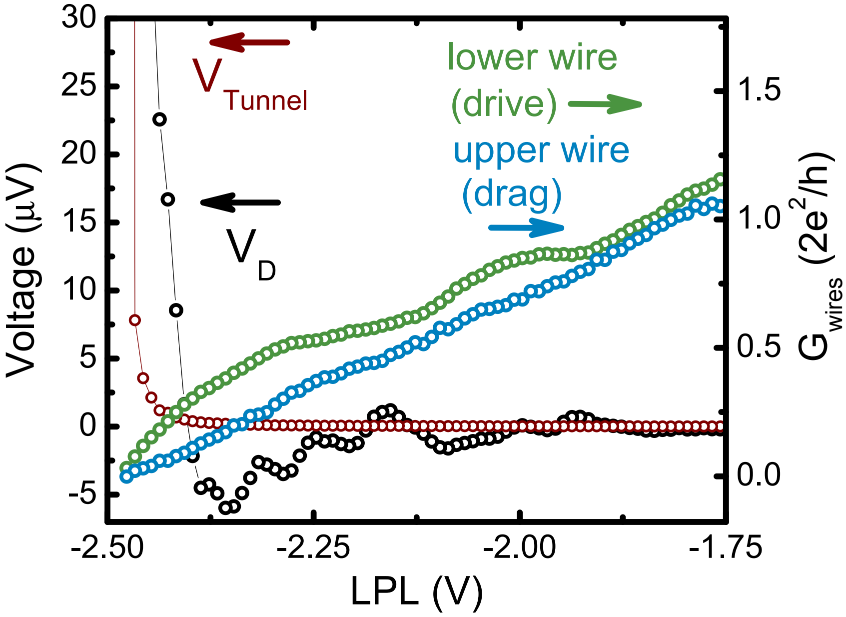

Fig. 6.10: Drag voltage (device 2-C from wafer EA0975) and parasitic tunneling voltage (black and red curves respectively, left-axis) along with the conductance of both the upper and the lower quantum wires (blue and green curves respectively, rigth-axis) as a function of LPL gate voltage for fixed UPL. The parasitic tunneling voltage overtakes the drag voltage at a LPL voltage of -2.47 V.

In this figure, the parasitic tunneling voltage (red curve) is monotonically increasing and is at least one order of magnitude smaller than the non-monotonic drag voltage ($V_{tunnel} < 0.1\ \mu$V) for most of the regime through which the drag signal is measured. It becomes non-negligible (*i.e.* larger than 1 μV) when the conductance of the drag wire is less than $0.07 \times 2e^2/h$ and eventually overcomes the drag voltage when the drag wire is almost completely depleted with a conductance smaller than $0.01 \times 2e^2/h$. Therefore, while any measurement performed with a drag wire conductance lower than $0.07 \times 2e^2/h$ cannot be safely interpreted as Coulomb drag, tunneling does not appear to impact the drag signal for more conducting wires.

ii) Linearity of the drag voltage with drive current

Another property the drag signal should have is that it should scale linearly with drive current. We have verified this property in three different regimes, which will be described in the next section, and the results are shown in figure 6.11

From this figure, it is empirically determined that the drag voltage is linear with drive current provided that $eV_{drive}/K_b \lesssim 3K$ in all three regimes[3]. The onset of the non-linearity at high current is not surprising since joule heating is likely to become significant in the wires and the drag signal is expected to have a strong temperature dependence. For all the Coulomb drag measurements reported from now on, a 4.5 nA (or less) drive current was used, ensuring that the measurements were taken within the linear Coulomb drag regime.

iii) Frequency independence

We also verified that the drag signal was independent of the frequency for frequencies lower than $\sim$ 50 Hz. While the Coulomb drag signal is expected to be frequency independent regardless of the frequency used, the refrigerator in

---

[3] Here, $V_{drive} = I_{drive}R_{drive}$

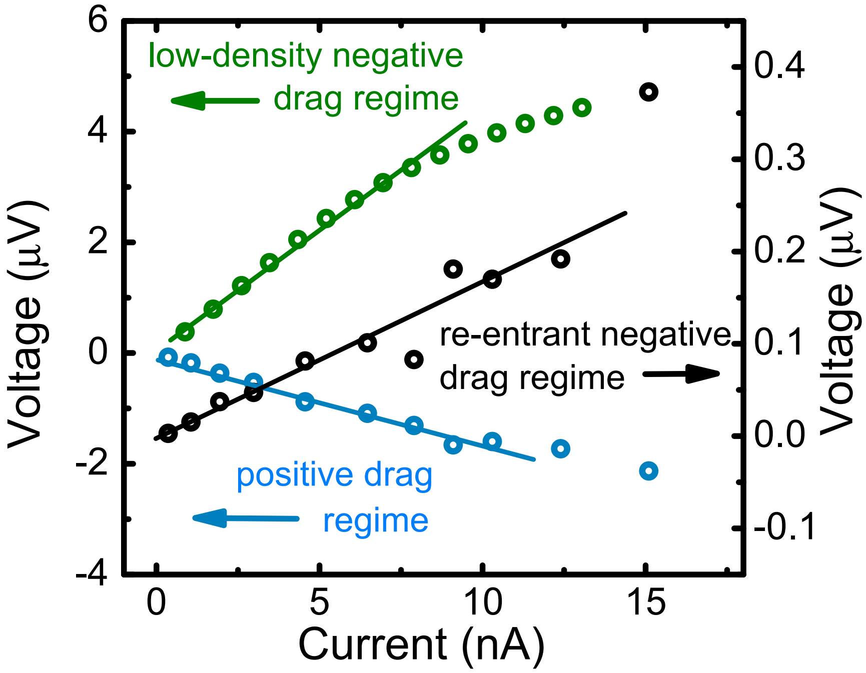

Fig. 6.11: Drag voltage versus drive current in the three regimes observed in the Coulomb drag signal, namely the positive drag regime (blue circles, left axis), the low-density negative drag regime (green circles, left-axis) and the high-density negative drag regime (black circles, right-axis). The solid lines highlight the regime where the drag voltage is linear with the drive current. These data have been taken in device 2-C from wafer EA0975.

which the device is mounted is capacitively coupled to the ground, and using frequencies higher than $\sim$ 50 Hz causes the signal on the lock-in amplifier to split between an in-phase signal and an out-of-phase signal. Therefore, to avoid this measurement artifact, the measurements were performed at low frequencies. As shown in figure 6.12, when the measurement is performed in the low frequency regime, the drag signal is frequency independent, as expected. We also confirmed that no drag signal was generated at higher harmonics of the drive current frequency.

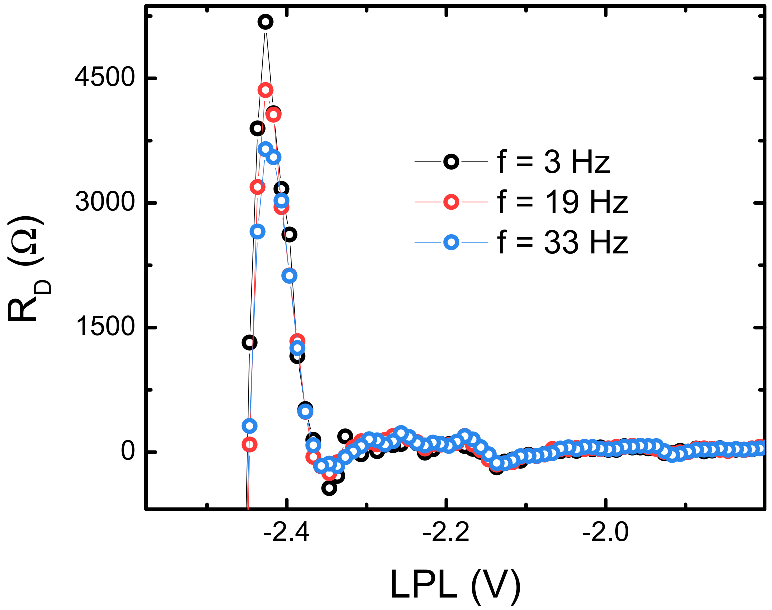

Fig. 6.12: Drag resistance as a function of the LPL voltage for various frequencies. These data have been taken in device 2-C from wafer EA0975.

iv) Probe symmetry

As shown in figure 6.13, we tested the probe symmetry of the drag signal. When the drag resistance is positive, probe symmetry is satisfied and the drag signal in identical (within error) regardless of the current direction. On the other hand, a change in the overall magnitude of the negative resistance is observed when the current direction is inverted. A charge-fluctuation model for Coulomb drag in mesoscopic circuits could partly explain such a phenomenon when an asymmetry exists in the transmission of electrons and holes in the system [4–6], however, it is not clear whether or not such model validates our main findings.

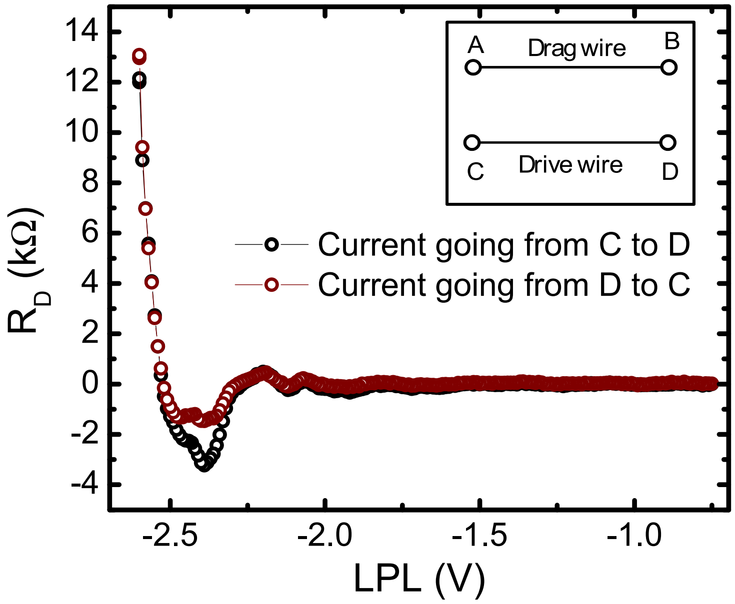

Fig. 6.13: Drag resistance as a function of the LPL voltage with different current directions. The terminals C and D labeling the current direction are shown in the inset. These data have been taken in device 2-C from wafer EA0975.

v) Onsager relation

Finally, the last test that was performed is to verify if Onsager relation was satisfied, or equivalently if the drag signal was identical upon drive and drag layers reversal. As we can see in figure 6.14, the drag signal is not entirely identical upon layer reversal. Nevertheless, the overall qualitative features of the signal, that is the presence of negative drag regions when both quantum wires are conducting, of a large peak in the drag signal as the drag wire first subband is populating and of a negative drag regime when the drag wire is depleting, remain the same upon layer reversal. We note however that if mesoscopic physics (charge fluctuations) plays a role in one-dimensional Coulomb drag, it is possible that the Onsager relations could perhaps be violated [4–6].

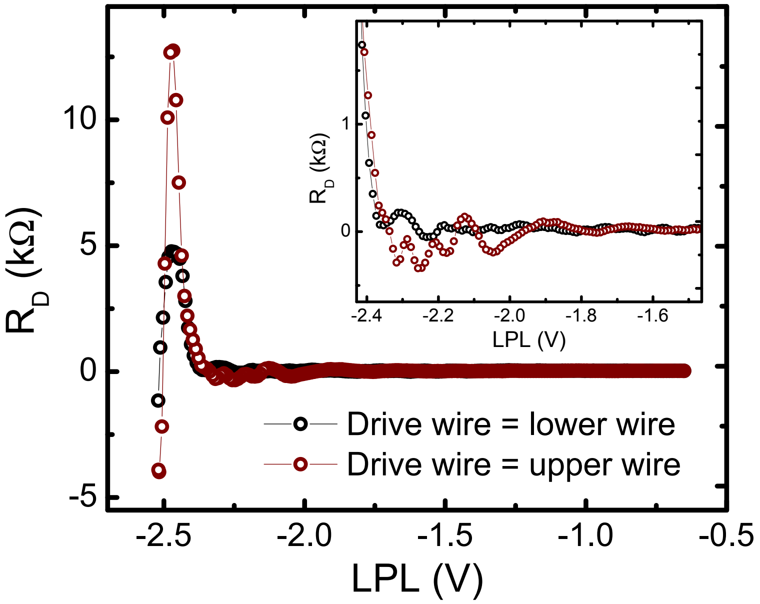

Fig. 6.14: Drag resistance as a function of the LPL voltage with the lower wire being the drive wire (black curve) and the upper wire being the drive wire (red curve). The three different Coulomb drag regimes can be observed in both configurations. These data have been taken in device 2-C from wafer EA0975.

These tests give us confidence that we are indeed measuring Coulomb drag and we can now move on to study the dependence of the drag signal on the wires 1D subband occupancy.

6.3.2 Main Results

A typical Coulomb drag curve is shown in figure 6.15. Here, the drag resistance is shown (black curve, left-axis) as a function of LPL voltage along with the conductance of both the upper and the lower quantum wires (blue and green curves respectively, right-axis) when the 1D subband occupancy in the drag wire (the upper wire in this case) is larger than in the drive wire.

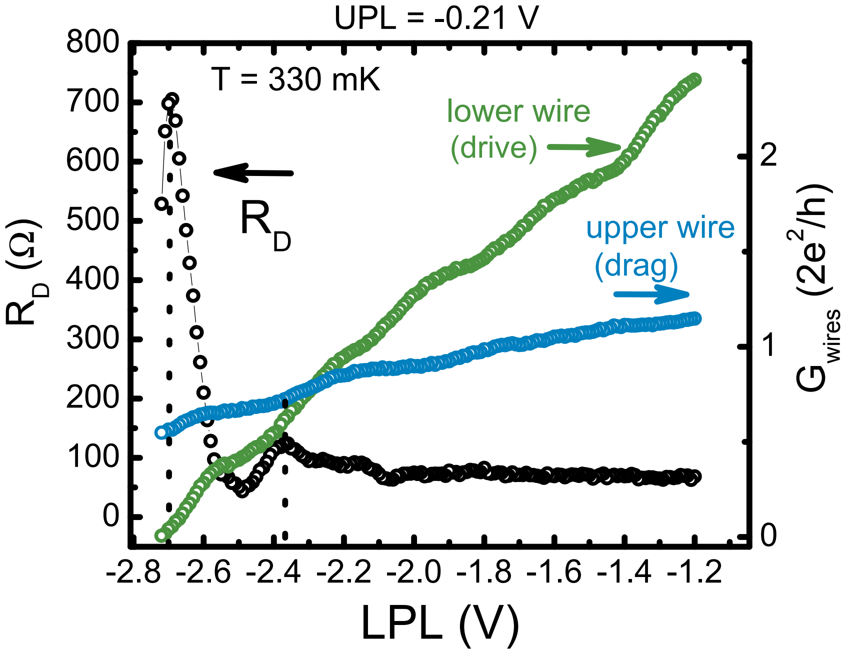

Fig. 6.15: Drag resistance (black curve, left-axis) along with the conductance of both the upper and the lower quantum wires (blue and green curves respectively, right-axis) as a function of LPL gate voltage for a fixed UPL = -0.21 V. Here, the drag wire has a higher 1D subband occupancy than the drive wire. These data have been taken in device 2-C from wafer EA0975.

This data shows a modulation of the positive drag signal with the 1D subband occupancy of the wires in a way that resembles to the data reported by Debray and coworkers [7]. This modulation of the drag signal is however strongly dependent on the 1D subband tuning of the device and significant departures from the data observed by Debray *et al.* are observed when the subband occupancy of the drag wire is similar or lower than the one in the drive wire.

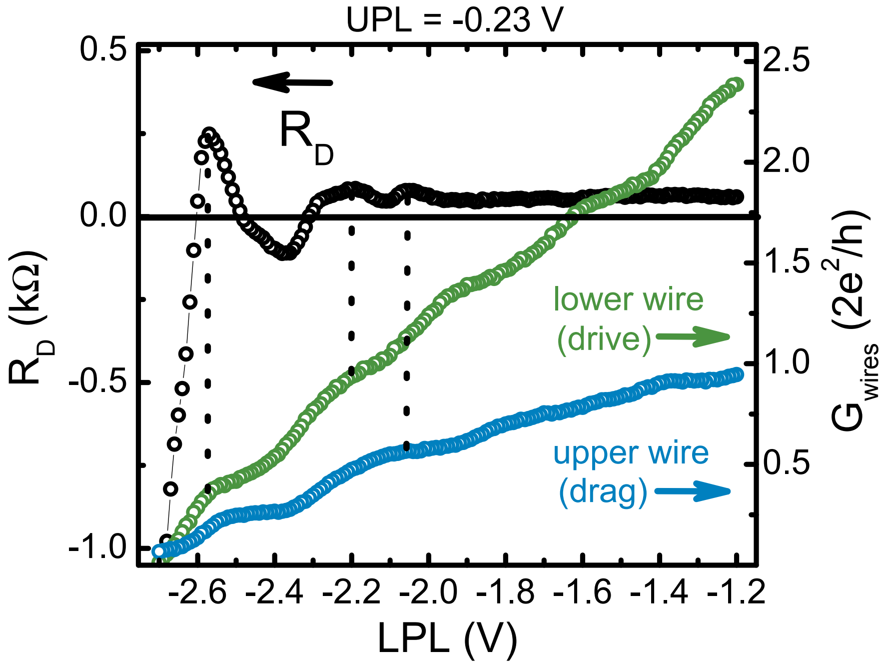

Fig. 6.16: Drag resistance (black curve, left-axis) along with the conductance of both the upper and the lower quantum wires (blue and green curves respectively, right-axis) as a function of LPL gate voltage for a fixed UPL = -0.23 V. Here, the drag and the drive wires have similar 1D subband occupancies. These data have been taken in device 2-C from wafer EA0975.

Figure 6.16 shows the drag signal when the 1D subband occupancy in both wires is similar and three prominent features are observed in the Coulomb drag resistance. These are:

i) The presence of peaks in the positive drag signal, seemingly occurring concomitant with the opening of 1D subbands in either wire, regardless of a density or subband alignment between the wires, as shown in figure 6.15, 6.16 and 6.17. In these three figures, the position of the peaks is highlighted by dotted vertical lines. This observation contrasts with previous experimental Coulomb drag results [7] where such maxima in the drag signal were only observed for matching subband occupancy and density between the quantum wires.

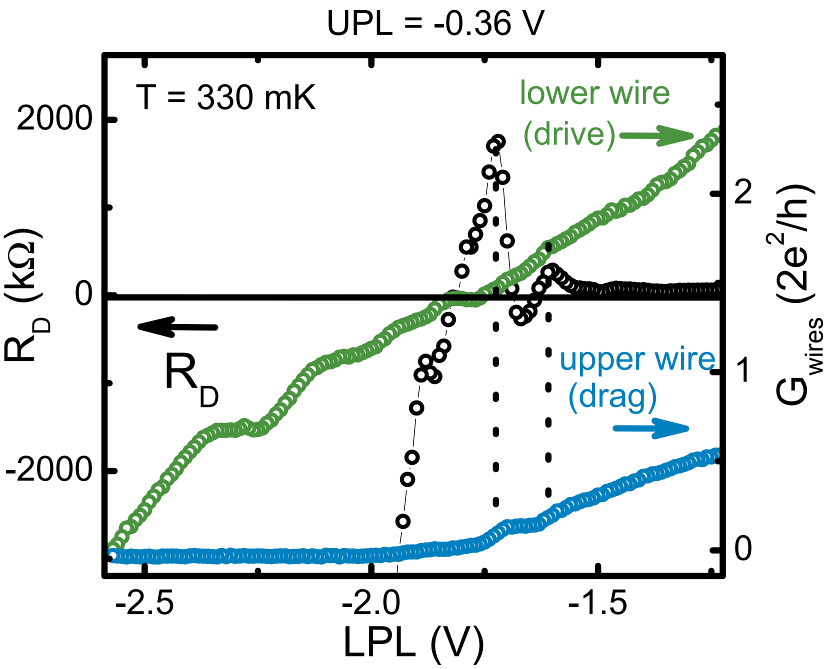

Fig. 6.17: Drag resistance (black curve, left-axis) along with the conductance of both the upper and the lower quantum wires (blue and green curves respectively, right-axis) as a function of LPL gate voltage for a fixed UPL = -0.36 V. Here, the drive wire has a higher 1D subband occupancy than the drag wire. These data have been taken in device 2-C from wafer EA0975.

ii) The presence of a low density negative resistance occurring when the drag wire is near depletion. This negative signal is only observed when the drag wire 1D subband occupancy is smaller than or equal to the one of the drive wire (figure 6.16 and 6.17). This feature is reminiscent of the negative Coulomb drag signal observed by Yamamoto *et al.* that was attributed to the formation of a Wigner crystal in the wires, although in our experiment the negative signal was observed in the absence of a magnetic field.

iii) The presence of a re-entrant negative drag resistance occurring when both the drive and the drag wires are clearly conducting. This negative signal is only observed when the drag wire 1D subband occupancy is smaller than or equal to the one of the drive wire (figure 6.16 and 6.17). Such a high-density negative Coulomb drag signal has never been observed previously.

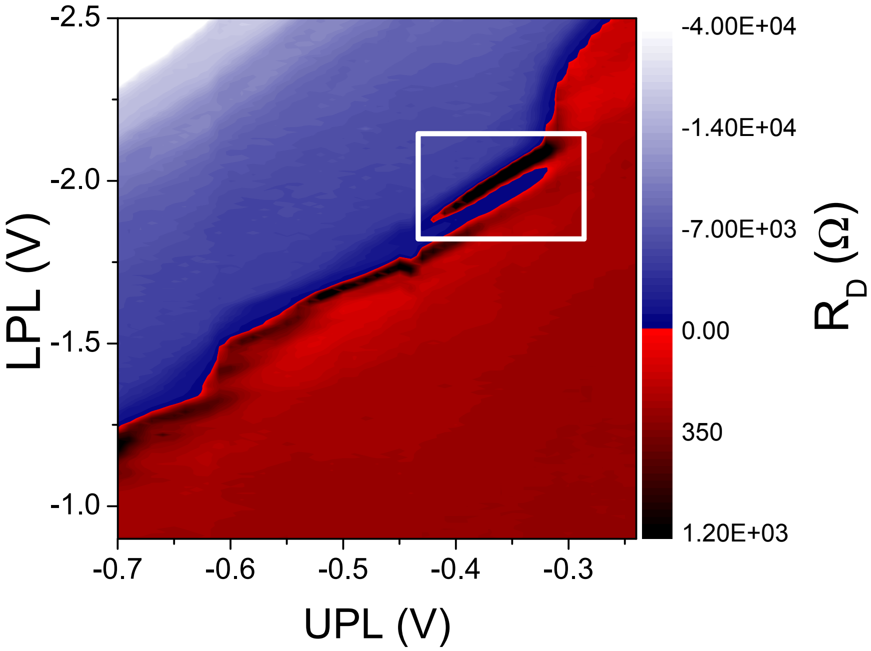

Fig. 6.18: Mapping of the Coulomb drag as a function of LPL and UPL voltages. The region in which a re-entrant high-density negative Coulomb drag signal is observed is highlighted by a white box. These data have been taken in device 2-C from wafer EA0975.

All the drag features discussed above have been observed consistently over several cooldowns of the device and over a wide range of gate voltage. Furthermore, they have been reproduced in more than one device. A mapping of the Coulomb drag signal as a function of both LPL and UPL voltages, taken during a different cooldown than in figures 6.15, 6.16 and 6.17, is presented in figure 6.18. The peaks in the drag signal appear as darker (or black) regions whereas the low-density negative drag regime is shown in blue. The high-density negative Coulomb drag signal is observed in the region highlighted by the white box.

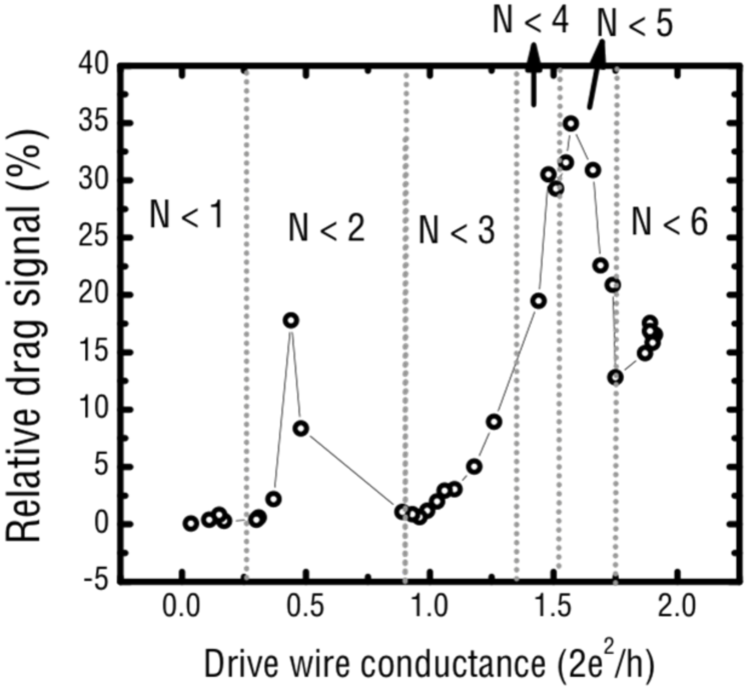

Fig. 6.19: Relative strength of the positive maximum of the drag signal as a function of the drive wire subband occupancy. The drag voltage is compared to the total voltage biased across the drive wire. These data have been taken in device 2-C from wafer EA0975.

A last point worth mentioning is the relative strength the Coulomb drag signal as a function of 1D subband occupancy. Regardless of the subband alignment between the wires, the positive maximum in the drag signal always occurs when $N_{drag} = 1$. However, the relative strength of this maximum is heavily dependent on the 1D subband occupancy of the drive wire, as shown in figure 6.19. Here, the relative strength of the drag voltage (compared to the voltage biased across the drive wire) shows a non-monotonic behavior as a function of 1D subband occupancy. The signal is less than $\sim 2\%$ of the drive signal for almost identical 1D subband occupancies in both wires whereas it can be as large as $\sim 35\%$ of the drive signal when $4 < N_{drive} < 5$. It also shows a relative maxima when $1 < N_{drive} < 2$ at $\sim 17\%$ of the drag signal.

6.3.3 Discussion

We discuss here each of the three main experimental features of the drag signal and compare them with the predictions of the various theoretical models for 1D Coulomb drag presented in chapter 4.

i) Peaks in the drag signal

Regarding the peaks in the drag signal, two main facts have been observed: the presence of relative maxima in the drag signal every time a 1D subband is populating and the non-monotonic dependence of the relative strength of the absolute maximum of the drag signal with the drive wire 1D subband occupancy. Within the momentum-transfer model, whether considering Fermi liquid formalism (equation 4.32), or Luttinger liquid formalism with backscattering [8] or forward scattering [9], the Coulomb drag signal is expected to be maximal for wires with an identical one-dimensional electronic density. Peaks are also predicted to occur for aligned conductance plateau where the momentum is a well-defined quantity.

However, in our experiment, the peaks in the drag signal occur at the first few openings of 1D subbands in either wire, regardless of the alignment of 1D subbands. Therefore, an alignment of conductance plateau inside the wires do not appear to explain the presence of these peaks. Also, the relative strength of the drag signal is non-monotonic and maximal for wires with a large mismatch between their 1D subband occupancy (see figure 6.19). Although we cannot directly measure the 1D electronic density of our wires, we can still estimate this density, using as a basis tunneling-spectroscopy measurements performed in similar structures [1]. From these, it has been shown that the 1D density of the wires when a single 1D subband is occupied is roughly given by $\sqrt{n_{2D}} \simeq n_{1D}$. Going from $N = 1$ to $N = 2$ in the wires also induced an increase in total 1D density the wires[4] by $\sim 70\%$. From the initial 2D density measurements of the wires, we estimate $n_{1D}^{upper} = 3.3 \times 10^7$ m^{-1} and $n_{1D}^{lower} = 3.7 \times 10^7$ m^{-1}. Therefore, if the drag signal was to be maximal for identical 1D densities, we should observe a maximum of the relative strength of the drag signal for $0 < N_{drive} < 1$ when $N_{drag} \simeq 1$ and a decreasing magnitude at lower and higher values of N_{drive}. However, our measurement shows two maxima, with the largest one occurring when $N_{drive} \gg 1$, clearly demonstrating that the drag signal is not maximal when the 1D densities between the wires are identical. This suggests that the momentum-transfer formalism for Coulomb drag may not be complete.

On the other hand, the fluctuation-induced model first brought forth by Levchenko and Kamenev [5] predicts a local enhancement of electron-hole asymmetry at the opening of 1D subbands (in either wire), which should induce a maxima in the drag signal of mesoscopic circuits, regardless of wave-vector alignment between the wires. Our device has a thermal length $L_T = \hbar v_F / k_B T \sim 2.5$ μm and a voltage length $L_V = \hbar v_F / eV \sim 1.5$ μm of the same

---

[4] We define the total density as $n^{total} = n^{N=1} + n^{N=2}$.

order of magnitude as the system size, suggesting that it is indeed in a mesoscopic regime[5]. Therefore, it appears that mesoscopic physics might play a non-negligible role in the onset of the oscillations in the drag signal.

i) Low-density negative signal

While the presence of a low-density negative Coulomb drag signal in apparent agreement with the data from Yamamoto *et. al* [10] is clearly observed in our data, caution must be taken when analyzing Coulomb drag in the low-density regime. Indeed, in this regime, the resistance across the drag wire can become non-negligible compared to the tunneling resistance, and hence the drag signal might be contaminated by quantum tunneling, as previously shown in figure 6.10. Therefore, any measurement performed with a drag wire conductance less than $0.07 \times 2e^2/h$ cannot be safely interpreted as Coulomb drag. While it appears that a portion of the low-density negative drag resistance (at a conductance between 0.08 and $0.13 \times 2e^2/h$ in the drag wire) might in fact be arising from Coulomb drag, there is a possibility that tunneling is still at the origin of this negative signal. For this reason, we cannot safely attribute this signal as originating from Wigner crystallization, as was concluded by Yamamoto *et al.* [10]. This tunneling-contaminated regime will not be explored further in the thesis.

---

[5] Even when one-dimensional systems described by the Luttinger liquid theory are considered, Fermi-liquid parameters, such as the Fermi velocity $v_F = hn_{1D}/4m^*$, are still commonly used to provide order of magnitude or to estimate physical quantities.

i) High-density negative Coulomb drag signal

Within the momentum-transfer formalism for Coulomb drag, the presence of a negative Coulomb drag resistance is only predicted to occur for drag between electron and (effective) holes [8, 9, 11]. It is not out of the question that a hole-like dispersion relation could occur in the wires and induce negative Coulomb drag, similarly to the two-dimensional negative Coulomb drag observed in the presence of Laudau levels [12, 13] and described in chapter 2 of this thesis. However, for one dimensional systems in the absence of magnetic field, there is *a priori* no theoretical or experimental evidence that a hole-like dispersion relation occurs in one-dimensional systems consisting of electrons.

As mentioned earlier, Wigner crystallization has been suggested to be at the origin of the low-density negative Coulomb drag regime [10]. However, this mechanism cannot explain the high-density negative drag observed when $N \geq 1$ in both wires. Indeed, Wigner crystallization should occur at a value of $r_s = (2na_0^*)^{-1} \geq 4$ [14], where a_0^* is the effective Bohr atomic radius. In the high-density negative drag regime, we estimate $r_s \sim 1.5$ and, therefore, Wigner crystallization cannot explain the observation of the high-density negative drag regime.

Looking at the charge-fluctuation model, more specifically at equation 4.49 and 4.50, it is possible for negative Coulomb drag to arise, given that the two wires are non-identical and that the transmission probability across one of the wire is non-monotonic, which can happen in non-symmetric mesoscopic circuits, like our system. Therefore, it appears that a charge-fluctuation model for Coulomb drag in mesoscopic circuits offer pathways of explanation for the presence of a negative Coulomb drag signal, although theoretical calculations for Coulomb drag between intrinsically coupled quantum wires would be required before the scope of the fluctuation-induced Coulomb drag formalism could be attested.

In summary, the oscillations in the drag signal observed with 1D subband occupancy variations, their magnitude and the presence of a high-density negative Coulomb drag signal suggest that the momentum-transfer formalism for Coulomb drag is incomplete. On the other hand, charge-fluctuations may occur in mesoscopic circuits and could play a role in one-dimensional Coulomb drag. Since the vast majority of the Coulomb drag theoretical models make clear predictions on the temperature dependence of the Coulomb drag signal, studying this dependency is key in clarifying the role of momentum-transfer and mesoscopic effects in one-dimensional Coulomb drag. This important study is the subject of the next chapter of this thesis.

References

[1] Bielejec, E., Reno, J. L., Lyo, S. K., and Lilly, M. P. *Solid State Comm.* **147**, 79 (2008).

[2] Raichev, O. E. *Phys. Rev. B* **64**, 035324 (2001).

[3] Auslaender, O. M., Yacoby, A., Picciotto, R., Baldwin, K. W., Pfeiffer, L. N., and West, K. W. *Phys. Rev. Lett.* **84**, 1764 (2000).

[4] Mortensen, N. A., Flensberg, K., and Jauho, A. P. *Phys. Rev. Lett.* **86**, 1841 (2001).

[5] Levchenko, A. and Kamenev, A. *Phys. Rev. Lett.* **101**, 216806 (2008).

[6] Sánchez, R., López, R., Sánchez, D., and Büttiker, M. *Phys. Rev. Lett.* **104**, 076801 (2010).

[7] Debray, P., Zverev, V., Raichev, O., Klesse, R., Vasilopoulos, P., and Newrock, R. S. *J. Phys.: Condens. Matter* **13**, 3389 (2001).

[8] Klesse, R. and Stern, A. *Phys. Rev. B* **62**, 16912 (2000).

[9] Pustilnik, M., Mishchenko, E. G., Glazman, L. I., and Andreev, A. V. *Phys. Rev. Lett.* **91**, 126805 (2003).

[10] Yamamoto, M., Stopa, M., Tokura, Y., Hirayama, Y., and Tarucha, S. *Science* **313**, 204 (2006).

[11] Gurevich, V. L., Pevzner, V. B., and Fenton, E. W. *J. Phys.: Condens. Matter* **10**, 2551 (1998).

[12] Gornyi, I. V., Mirlin, A. D., and von Oppen, F. *Phys. Rev. B* **70**, 245302 (2004).

[13] Bistritzer, R. and Stern, A. *Phys. Rev. Lett.* **96**, 226801 (2006).

[14] Saini, L. K., Tankeshwar, K., and Moudgil, R. K. *Phys. Rev. B* **70**, 075302 (2004).

7

Temperature dependence of 1D-1D Coulomb drag

In this chapter, the temperature dependence of 1D Coulomb drag is studied in detail in an attempt to better understand the mechanisms at play behind its emergence and to better understand electron-electron interactions in one dimension. First, a description of the three devices used to perform the temperature dependence analysis of 1D Coulomb drag along with a description of the dilution refrigerator apparatus are presented. Then, an overview of the overall temperature dependence of the drag signal for different 1D subband occupancies in a single device is shown. Following this, a quantitative study of the temperature dependence of the drag signal is performed in the true one-dimensional regime where both quantum wires have a conductance (slightly) lower or equal to the conductance of the first plateau where a single channel is open in the quantum wires. In this regime, we have observed an upturn flagging a crossover transition between a regime where the drag resistance decreases with decreasing temperature, to a regime where the drag resistance increases with decreasing temperature. This upturn was observed in three different devices at a temperature in the vicinity of $T^* \sim 1.6$ K. This observation and the high temperature behavior of the Coulomb drag signal is in qualitative agreement with the predictions of TLL theory and might validate models including forward scattering corrections.

7.1 Experimental Details

7.1.1 Device Details

Three different devices have been studied in detail regarding the temperature dependence of the Coulomb drag signal. All devices were fabricated on the same heterostructure (EA0975) in parallel, following the fabrication process discussed in chapter 5. They have been designed with the same dimensions (5 μm long and 0.5 μm wide), as defined lithographically. These devices are labeled 2-C, 2-L and 3-R. Devices 2-C and 2-L were fabricated on the same chip whereas device 3-R is physically on a different piece of heterostructure. Devices 2-C and 2-L have a two-dimensional electronic density of 1.1 (1.4) $\times 10^{11}$ cm^{-2} for the upper (lower) 2DEG and device 3-R has a two-dimensional electronic density of 1.0 (1.2) $\times 10^{11}$ cm^{-2} for the upper (lower) 2DEG. While we cannot directly measure the 1D density of the wires, we can estimate it from $n_{1D} \simeq \sqrt{n_{2D}}$. Such an estimate yields a difference of 8% (5%) in the 1D density of the upper (lower) wire between these devices, and so we shall assume that all devices have their electronic density in the same range when performing estimates. Devices 2-C and 3-R have been measured down to a temperature of

$\sim$ 330 mK in the helium-3 refrigerator setup described in chapter 6, whereas device 2-L has been measured down to an electron temperature of $\sim$ 75 mK in a dilution refrigerator. The electron temperature is assumed to be that of the lattice, a reasonable assumption until the drag signal begins to saturate in the vicinity of T $\sim$ 75 mK. This has been verified for various 1D subband occupancies in the wires to ensure that the saturation was indeed caused by a saturation of the electron temperature and *not* by an intrinsic saturation of the drag signal.

7.1.2 Dilution Refrigerator

The dilution refrigerator used to measure device 2-L down to an electron temperature of $\sim$ 75 mK is a Kelvinox 300 Oxford Instruments dilution refrigerator. The system is mounted inside a dewar fitted with a superconducting magnet. The sample is mounted in the center of the magnetic field and can be exposed to a magnetic field strength of up to 14 T. A schematic of this setup is presented in figure 7.1.

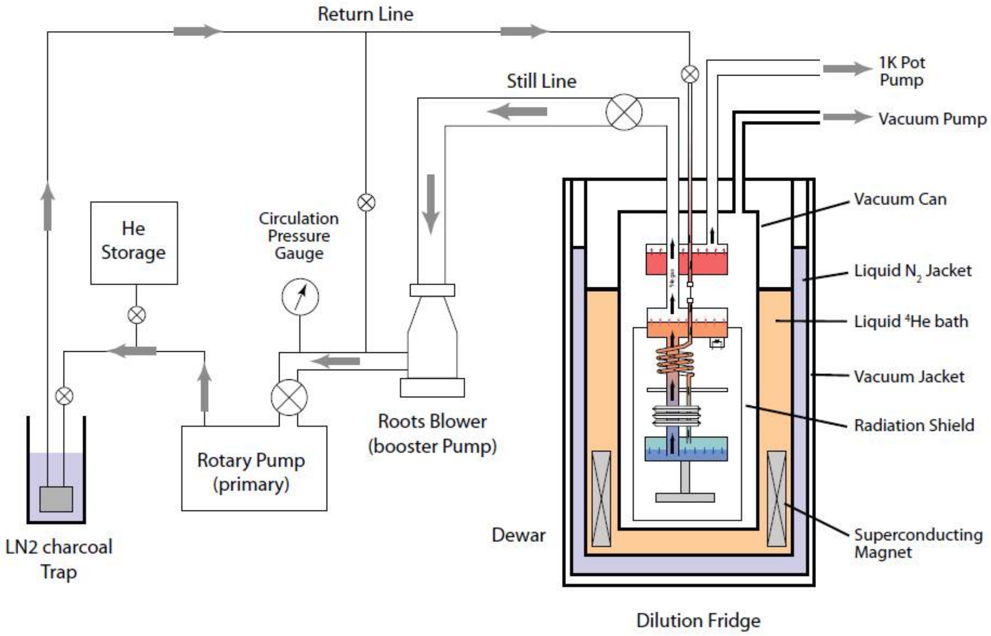

Fig. 7.1: Schematics of the dilution refrigerator system used in this thesis. Figure taken from C. R. Dean [1].

This system was operated in a continuous mode and as such the device could be maintained at the base temperature of the system as long as desired. Without the experimental tail, the system can cool down to 7.05 mK with a power of 12 mW applied to the still heater, yielding a cooling power of 50 μW at 64 mK. However, under experimental conditions, the base temperature of the system was $\sim$ 24 mK (as measured by a RuO thermometer) with a power of 3 mW applied to the still heater. We stress, however, that the base temperature of the system, as measured by the RuO thermometer, is likely to be different from the 1D electron temperature in the device at the lowest temperatures. In our experiment, we can reliably attest that the electrons were cooling down to $\sim$ 75 mK, at which point saturation in the drag signal would occur, owing to an insufficient thermal anchoring and/or filtering of the device. For this reason, we shall only present data from ~ 75 mK and above where electron temperature is not an issue. Finally, in our setup, the sample space is in vacuum and the device itself is cooled by heat exchange with the metallic electrical wires connected to the device, which are thermally anchored to the mixing chamber, the coldest part of the system.

7.2 Temperature Dependence of Coulomb Drag versus 1D subband occupancy

As mentioned in chapter 6, the temperature dependence of the Coulomb drag signal could provide significant insight into the nature of the correlated 1D electronic state of coupled 1D systems. It can also give important insights as to whether drag arises from momentum transfer between Luttinger liquids (with or without forward scattering corrections), from an energy transfer in the form of charge fluctuations or a combination of both.

As a first step towards this goal, the temperature dependence of the Coulomb drag signal was measured for device 2-C. This is the same device for which we have presented the results in chapter 6. The drag signal for various 1D subband occupancies is shown in figure 7.2 down to $T \simeq 330$ mk. From this figure, one can readily notice that the overall qualitative behavior of Coulomb drag is heavily influenced by the 1D subband occupancy of the quantum wires.

Indeed, at very low density (blue curve), the drag signal increases with decreasing temperature until a plateau is reached. On the other hand, the

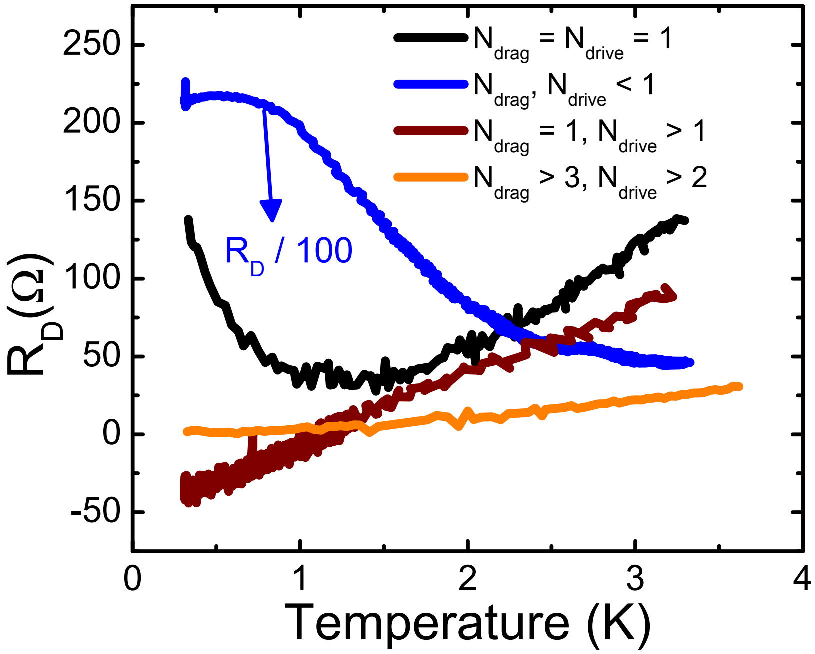

Fig. 7.2: Temperature dependence of the Coulomb drag signal in sample 2-C with $N_{drag} = N_{drive} = 1$ (black curve), with $N_{drag}, N_{drive} < 1$ (blue curve), with $N_{drag} = 1, 1 < N_{drive} < 2$ (red curve). and with $2 < N_{drag} < 3, 1 < N_{drive} < 2$ (orange curve). These data demonstrate the different qualitative behavior of the drag signal for different 1D subband occupancies and have been taken in device 2-C from wafer EA0975.

drag signal behaves monotonically with temperature in the negative Coulomb drag regime (red curve), as well as with a subband occupancy larger than N = 2 (orange curve). Most importantly, an upturn is observed in the temperature dependence of the drag signal (black curve) when both wires have $N_{drag} = N_{drive} = 1$, *i.e.* in the true 1D regime. This large variation in the qualitative behavior of the temperature dependence of 1D Coulomb drag is striking, and not easily explained by theory. Indeed, in the charge fluctuation model [2, 3], a monotonic temperature dependence of Coulomb drag should occur, unless electron-hole asymmetry happens to be greatly temperature dependent, which is unlikely.

In our view, the temperature dependence in the true 1D regime appears to be in qualitative agreement with models considering momentum-transfer between Luttinger liquids and accounting for forward scattering corrections [4] (see figure 4.12 **(e)**), however backscattering alone cannot be completely ruled out [5]. In addition, a non-monotonic temperature dependence could also arise due to finite-length effects [6] or mesoscopic effects [7, 8]. Of paramount importance is the observed upturn, predicted to occur at a temperature T^*. This upturn in the drag signal is signaling an important change in the physics of the system. To our knowledge, there are very few mechanisms that can produce a diverging drag in the $T \to 0$ limit. These include Luttinger liquid models, and condensation of electron-hole pairs, the latter being very unlikely to occur in these devices. While we do not fully understand the drag signal when several subbands are occupied, we note that the negative drag signal weakens with temperature and actually disappears at $T \sim 1.2K$. This observation is consistent with the system leaving the mesoscopic regime as the temperature length $L_T = \hbar v_F / k_B T$ is lowered from ~ 2.5 μm at 0.33 K to ~ 0.7 μm at 1.2 K, and becomes significantly shorter than the system size, suggesting that mesoscopic physics plays a role in the emergence of the negative Coulomb drag signal.

For the remainder of this chapter, our discussion will focus on a deeper analysis of the drag signal in the regime where only a single 1D subband (or channel) is occupied in either quantum wires. We will show that the upturn in the drag signal is reproduced in three distinct devices. The observation of an upturn at $T = T^{*}$ greatly strengthens the case of LL physics occurring in coupled quantum wires.

7.3 Temperature Dependence of Coulomb Drag in the 1D Regime

The gate voltages for which the the wires are in the true 1D regime ($N_{drag} \simeq N_{drive} \simeq 1$) and where the temperature dependence was measured is highlighted by grey shadings in figure 7.3. The Coulomb drag data presented here for devices 2-L and 2-C are fully consistent with the data previously taken in sample 2-C and discussed in the previous chapter. One noteworthy difference between the drag traces data from device 2-L (measured down to ~ 75 mK) and 2-C (measured down to ~ 330 mK) is the additional presence of high-density negative drag regimes occurring whenever a peak in the drag signal is observed, suggesting that the high-density negative Coulomb drag is enhanced at low temperature.

We show in figure 7.4 **(a)** the temperature dependence of the Coulomb drag signal taken in *three* different devices in the one-dimensional regime. In devices 2-C and 2-L, a single 1D subband (or slightly less) is occupied. In device 3-R however, the 1D subband occupancy of the wires was not precisely known at the time of the measurement. This is because this device was the first to be successfully measured, but has unfortunately been irremediably damaged prior

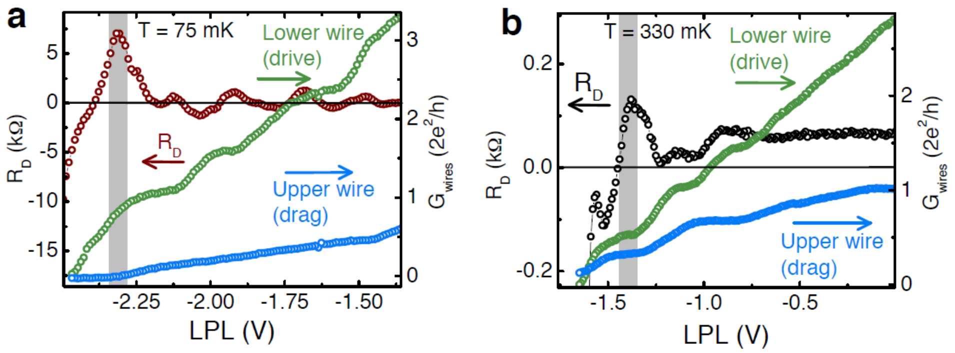

Fig. 7.3: **(a)** Drag resistance (red curve, left-axis) along with the conductance for both the upper and the lower quantum wires (blue and green curves respectively, right-axis) as a function of LPL gate voltage (for fixed UPL) at a temperature of ∼ 75 mK for device 2-L (wafer EA0975). **(b)** Drag resistance (black curve, left-axis) along with the conductance for both the upper and the lower quantum wires (blue and green curves respectively, right-axis) as a function of LPL gate voltage (for fixed UPL) at a temperature of ∼ 330 mK for device 2-C (wafer EA0975). Both traces show the same qualitative features and the true 1D regime, where the 1D subband occupancy in both wires is near one, is highlighted by a gray shading.

a complete mapping of the conductance could be performed. In this case, we can only provide a bound on the 1D subband occupancy of the wires, which we estimate to be $0 < N_{drive} \leq 2$ and $0 \leq N_{drag} \leq 3$. Despite this drawback for this device, we have included its data here since its temperature dependence shows the same qualitative feature as for devices 2-L and 2-C.

7.3.1 Upturn in the Temperature Dependence of the Drag Signal

Perhaps the most remarkable feature of the data is the presence of a crossover transition from a high temperature regime where the drag resistance decreases with decreasing temperature (verified up to $\gtrsim 3.5$ K in devices 2-C

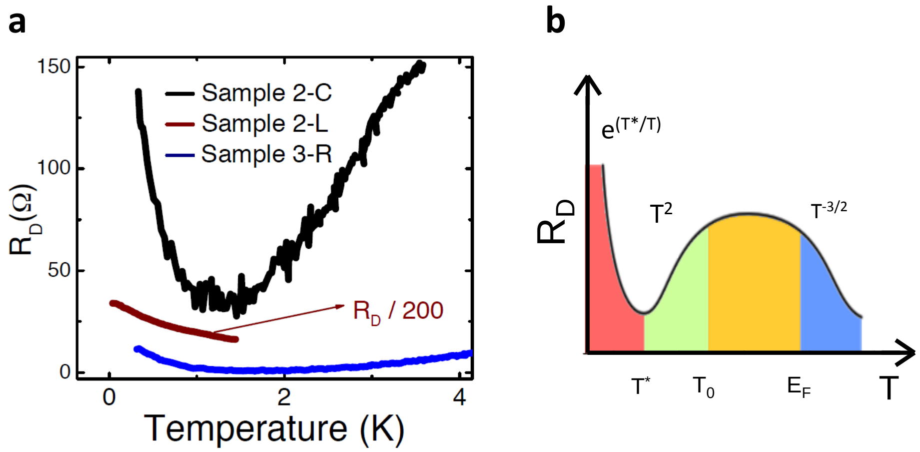

Fig. 7.4: **(a)** Temperature dependence of the Coulomb drag signal in the regime where a single 1D subband (or slightly less) is occupied in each quantum wire for three different devices (from wafer EA0975), namely 2-C (black curve), 2-L (red curve) and 3-R (blue curve). All three devices show an upturn in the temperature dependence of the drag signal in the vicinity of $T^* \sim 1.6$ K. **(b)** Theoretical temperature dependence of the drag resistance within the Luttinger liquid framework considering both forward and backscattering. This model predicts an upturn in the temperature dependence of the drag signal.

and 3-R) to a low temperature regime where the drag resistance diverges with $T \to 0$ (verified down to $\sim$ 75 mK in device 2-L). Despite the fact that the magnitude of the drag resistance is significantly different in all three devices (which could be explained by a different density imbalance), the upturn in the temperature dependence of the drag signal is observed in the vicinity of $T^* \sim 1.6$ K in all three devices, namely at $T^* \sim 1.4 \pm 0.2$ K in device 2-C, $T^* \sim 1.8 \pm 0.2$ K in device 3-R and $T^* \sim 1.7 \pm 0.2$ K in device 2-L.

Within the models discussed in chapter 4, only a model considering momentum-transfer between Luttinger liquids [4, 5] can account for the presence of such an upturn in the Coulomb drag signal at high 1D electronic density. Such an upturn has also been predicted to occur in the spin-incoherent regime for Luttinger liquids where the spin exchange energy $J = E_F e^{-2.9/\sqrt{na_b}}$ is suppressed [9]. However, this regime is expected to occur at low density ($na_B \ll 1$) and for $T^* < J < T < E_F$. In our wires, we estimate $J \sim 150$ mK $< T^*$ and $na_B \sim 0.4$, and it is unlikely that our devices are in the spin-incoherent regime. According to the LL model, the upturn in the temperature dependence of the drag resistance flags a crossover between a high temperature regime ($T > T^*$) where forward scattering is the main contribution to Coulomb drag to a low-temperature regime ($T < T^*$) where backscattering is expected to be dominant. This leads, theoretically, to a crossover transition between a power-law dependence and an exponential dependence on temperature, provided that $1 < k_f d \sim 2.2$ and $L > L^* \sim \hbar v_f / T^* = 0.5$ μm, as is the case in our devices. Here, L^* is a critical length such that for $L > L^*$, an exponential increase in drag resistance is expected as $T \to 0$. For $L < L^*$, one would instead expect a non-diverging drag signal in the $T \to 0$ limit.

Using equation 4.7, our best estimate for the electronic density in the wires, *i.e.* $n_{1D} = \sqrt{n_{2D}}$, and an interwire separation $d = 40$ nm (corresponding to the barrier width plus half of both well widths plus the vertical misalignment), we estimate from the values of T^* the relative interaction parameter for antisymmetric charge displacement to be $K_\rho^- \simeq 0.16 \pm 0.02$ for sample 2-C, $K_\rho^- \simeq 0.08 \pm 0.02$ for sample 3-R and $K_\rho^- \simeq 0.10 \pm 0.02$ for sample 2-L. These relatively low values of K_ρ^- imply that the intra and interwire small-momentum couplings are similar and that electron-electron interactions are significant [9, 10]. Such a result is not unexpected since the wires are in close proximity, and hence intra- and inter- should be of similar strength within the Luttinger liquid model [10].

7.3.2 High Temperature regime

Within the Luttinger-liquid theory with forward scattering corrections, the temperature dependence of the drag signal at high temperature ($T > T^*$) is expected to follow a power-law with a universal exponent of 2 [4], namely $R_D \propto T^\gamma$ where $\gamma = 2$. In order to compare our data with this prediction, a log-log plot of the drag resistance versus temperature is shown in figure 7.5.

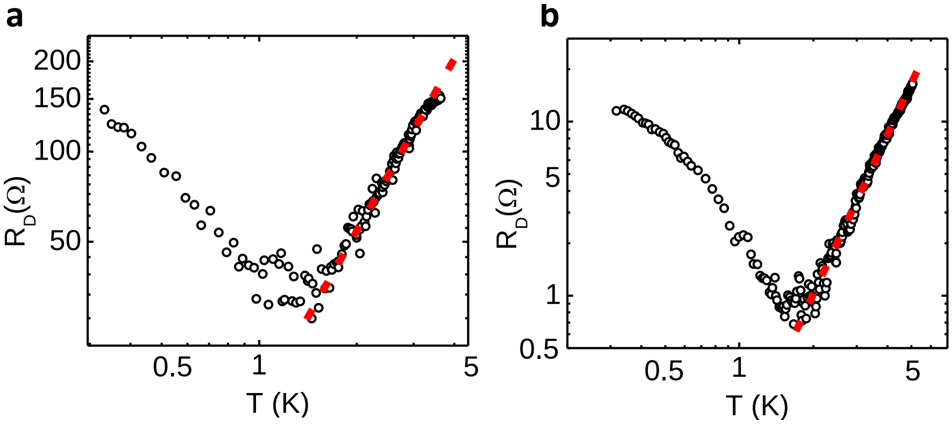

Fig. 7.5: Log-log plot of R_D versus T for **(a)** device 2-C (wafer EA0975) and **(b)** device 3-R (wafer EA0975). A linear fit (red dotted lines) is shown in the high temperature regime.

For both device 2-C and 3-R, we can clearly see that the log-log plot of R_D versus T is linear (on a log scale) in the high temperature regime. This is emphasized by the red dotted lines in this figure, which are yielding power-law exponents of $\gamma = 1.9 \pm 0.1$ and $\gamma = 3.0 \pm 0.1$ for device 2-C and 3-R, respectively.

While the exponent for device 2-C is indeed consistent with expectations from Luttinger liquid theory with forward scattering corrections, it is significantly different in device 3-R, and conspicuously given by a cubic behavior. We note however that the theoretical model used here considers drag between wires with identical 1D densities. This is unlikely to be the case in our devices since the parent electronic densities in both 2D layers differ by ~ 20 % post processing. According to Pustilnik *et al.* [4], even a slight density imbalance of $\sim 2.5\%$ between the wires would have strong effects on the behavior of the drag signal with temperature. As a tentative explanation, we propose that density imbalance between our wires could be responsible for the discrepancy between the power-law exponents extracted from these two distinct devices.

As discussed in chapter 4, the density imbalance is likely to affect the drag behavior for $T < T_1 = k_f \Delta(v)$. In our samples, our estimate for the density balance parameter gives $T_1 \sim 5.4$ K, which is higher than the temperature at which the Coulomb drag measurement is performed. So, we expect this imbalance to affect the analytic form of the Coulomb drag resistance. In this case, the predicted high-temperature power-law behavior of the drag resistance is then likely to be a convolution of a power-law with an exponential decay, $R_D \propto T e^{-T_1/T}$. From our estimated T_1 values, we expect this to remain true as long $T > T_{crossover} \sim 450$ mK. If we were in a regime where $T^* < T_{crossover} < T$, then the drag signal would likely behave as a power law with temperature with an exponent $\gamma = 5$. This exponentially decaying behavior of the drag resistance with decreasing temperature might be observed in our devices, as suggested by the Arrhenius plot of the data presented in figure 7.6.

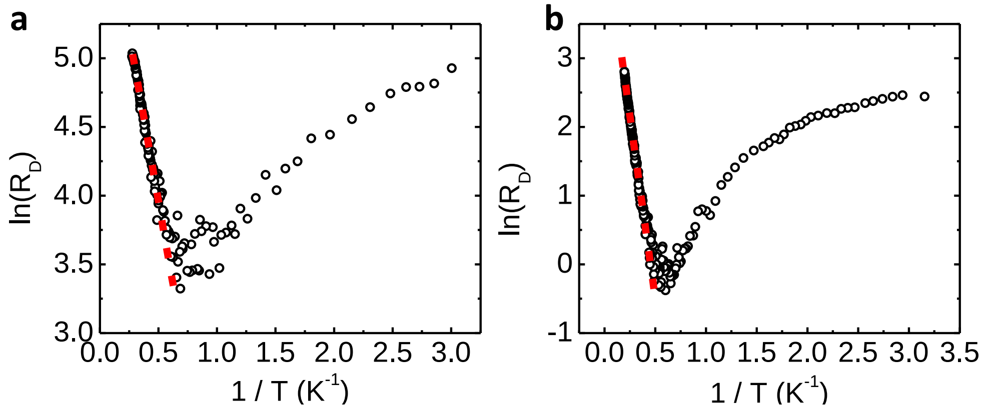

Fig. 7.6: Arrhenius plot of the temperature dependence of the Coulomb drag resistance for **(a)** device 2-C (wafer EA0975) and **(b)** device 3-R (wafer EA0975). A linear fit (red dotted lines) has been performed in the high temperature regime.

This figure suggests that the natural logarithm of the drag resistance behaves linearly with the inverse of the temperature in the high temperature regime, as expected for devices with a significant density imbalance. Extracting the experimental value of T_1 from a linear fit of the Arrhenius plots in this high-temperature regime, we obtain $T_1 = 4.8 \pm 0.4$ K ($T_1 = 10.7 \pm 0.4$ K) for device 2-C (3-R). These extracted T_1 values are comparable with the calculated $T_1 = 5.4$ K value from the estimated density imbalance, confirming that this imbalance significantly affects the temperature dependence of the drag resistance. These imbalance values are also consistent with both wires being in a regime where $N \leq 1$. We note that, for the parameters of our experiment, we estimate $u/\theta \sim 1.2/T$ and therefore, we do not expect finite length effects to play a significant role in the high-temperature regime where $T > T^* \sim 1.6$ K. Despite the good agreement between the experimental fit and Luttinger liquid models with forward scattering corrections, we cannot completely rule out that backscattering alone is at the origin of the exponential decay of the drag resistance for $T > T^*$ [5, 11].

7.3.3 Low Temperature regime

While the data in the high temperature regime ($T > T^*$) appears to be consistent with a Luttinger liquid model including forward scattering corrections, the situation is not as clear in the low temperature regime. In figure 7.5 and figure 7.6, the diverging resistance in the $T \to 0$ limit is observed to be neither linear in a log-log plot nor in an Arrhenius plot. The same is true for device 2-L which has been measured down to $\sim$ 75 mK, as shown in figure 7.7.

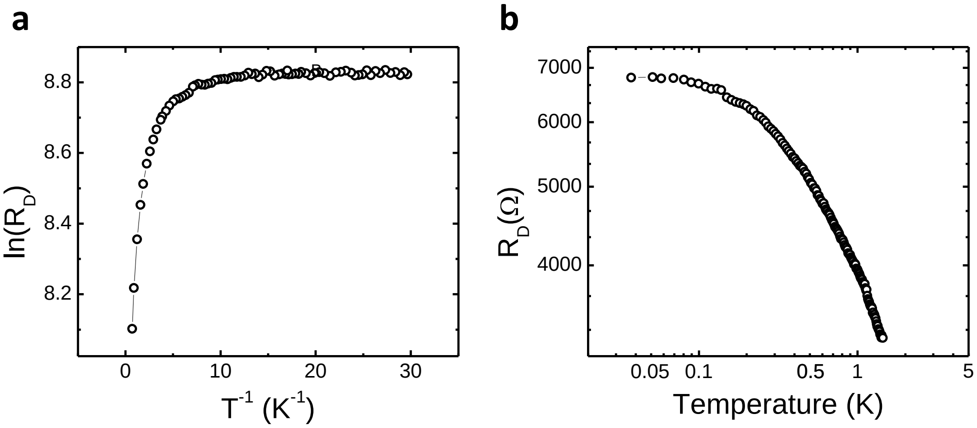

Fig. 7.7: Temperature dependence of the drag resistance for device 2-L (wafer EA0975) in **(a)** Arrhenius form and **(b)** log-log form. In the $T \to 0$ limit, a clear power-law or Arrhenius behavior cannot be succesfully identified.

Within the TLL theoretical models, one would expect for $T > T_{crossover}$ to observe a convolution between two exponential functions and a convolution between an exponential and a power-law for $T < T_{crossover}$. From our data, it is not yet clear whether the drag has these temperature dependencies, although the drag resistance is clearly increasing with decreasing temperature, a strong prediction of theory when backscattering is the dominant contribution to drag (for $T < T^*$) [4, 10]. A possible explanation for this is the transition occurring for $T = T_{crossover} \sim 450$ mK between power-law and exponential corrections to the drag signal for wires with mismatched densities. Indeed, in the vicinity of this crossover temperature, both power-law and exponential decay contributions to the drag signal should be of comparable magnitude, effectively preventing us from extracting a clean analytic form from our data. Finite-length effects, which are predicted to become significant at $T \leq 0.6$ K when $u/\theta > 2$ [6], might also play a role in the low-temperature regime. Measuring the drag signal to even lower temperatures, down to ~ 5 mK, for example, might allow us to extract the exact functional dependence in the $T \to 0$ limit. This will be the object of future work and towards this goal, an experiment is currently underway.

In summary, the temperature dependence of the drag signal in the true 1D regime, *i.e.* when a single 1D subband or less is occupied in both quantum wires, appears to be in semi-quantitative agreement with theoretical models based on momentum-transfer between two Luttinger liquids, when corrections for forward scattering are taken into account. Future work will focus on fabricating coupled 1D systems with more closely matched 1D densities, as well as with lower disorder. It is our hope that the important upturn in the drag resistance, as well as the divergence in the $T \to 0$ limit, will be considered an important advance in the understanding of coupled 1D systems.

References

[1] Dean, C. R. *A Study of the Fractional Quantum Hall Energy Gap at Half Filling.* Ph. D. dissertation, McGill University, (2008).

[2] Levchenko, A. and Kamenev, A. *Phys. Rev. Lett.* **101**, 216806 (2008).

[3] Sánchez, R., López, R., Sánchez, D., and Büttiker, M. *Phys. Rev. Lett.* **104**, 076801 (2010).

[4] Pustilnik, M., Mishchenko, E. G., Glazman, L. I., and Andreev, A. V. *Phys. Rev. Lett.* **91**, 126805 (2003).

[5] Fuchs, T., Klesse, R., and Stern, A. *Phys. Rev. B* **71**, 045321 (2005).

[6] Peguiron, J., Bruder, C., and Trauzettel, B. *Phys. Rev. Lett.* **99**, 086404 (2007).

[7] Narozhny, B. N. and Aleiner, I. L. *Phys. Rev. Lett.* **84**, 5383 (2000).

[8] Mortensen, N. A., Flensberg, K., and Jauho, A. P. *Phys. Rev. Lett.* **86**, 1841 (2001).

[9] Fiete, G. A., Le Hur, K., and Balents, L. *Phys. Rev. B* **73**, 165104 (2006).

[10] Klesse, R. and Stern, A. *Phys. Rev. B* **62**, 16912 (2000).

[11] Dmitriev, A. P., Gornyi, I. V., and Polyakov, D. G. *Phys. Rev. B* **86**, 245402 (2012).

8

Conclusion and Outlook

8.1 Summary and Results

In the first part of the thesis, we presented our report on the fabrication of doped shallow 2DEGs, as well as their electrical characterization. The goal of this study was to determine the dominant scattering mechanisms in these shallow 2DEGs. By carefully optimizing the dopants density and separation from the surface, devices as shallow as 60 nm deep and with a mobility in excess of $\sim 1 \times 10^5$ cm^2/ V $\cdot$ s at a density of $\sim 3 \times 10^{11}$ cm^{-2} were successfully fabricated.

A systematic study of the mobility dependence upon the 2DEG electronic density revealed an intermediate density regime where the mobility showed a power-law dependence with density. Extracting the power-law exponents for devices with a quantum well depth located between 198 nm and 60 nm deep, it was found that the deepest quantum well has an exponent $\alpha = 1$, consistent with scattering arising from (background) unintentional charged impurities. As the quantum wells depth was reduced towards 130 nm, the power-law exponents steadily increased towards $\alpha \simeq 1.5$, which is consistent with the intentional charged dopants being the dominant source of scattering in the devices. Finally, as the devices became ever shallower, α was found to move towards a value of 1.3, consistent with remote charged impurities still being the dominant scattering source, but with an increased screening owing to their closer proximity to the quantum well. These findings have been found to be in quantitative agreement with a theoretical model brought forth by Hwang and Das Sarma [1] .

In the second part of the thesis, we presented our efforts towards the fabrication of vertically-coupled quantum wires, as well as their characterization and the measurement of one-dimensional Coulomb drag. Vertically-coupled and independently contacted quantum wires separated by a barrier only 15 nm wide were successfully fabricated in a double quantum well heterostructure. These wires were found to be misaligned by less than 25 nm in the direction perpendicular to the wires, yielding an effective interwire separation bounded between 33 nm and 41 nm. This system is the most closely packed independently contacted quantum wires system reported in the literature to date. These wires were found to be in the non-ballistic regime and to be non-identical. In addition, regimes where both wires had a similar or a different 1D subband occupancy could be achieved.

Using these wires, Coulomb drag measurements were performed and the 1D subband occupancy dependence of the drag signal was investigated. Towards this goal, the Coulomb drag signal was mapped versus the 1D subband occupancy of both wires and three features were observed in the drag signal.

First, peaks in the drag signal were observed concomitant with the opening of 1D subbands in either wires. Second, a negative Coulomb drag regime was observed at low 1D subband occupancy (or 1D density) in the wires. Due to the possibility that this signal may be contaminated by tunneling when the wires are so resistive, this regime was not further investigated. Finally, a new, never seen before, high density negative Coulomb regime was observed. This negative drag resistance was first observed when the drag wire was at a subband occupancy of $N_{drag} = 1$, but it was later found to also occur following every peak in the drag signal at temperatures below $\sim$ 100 mK. The magnitude of the drag resistance was also found to vary non-monotonically with 1D subband occupancy, reaching a global maximum of $\sim$ 35 % of the sourced drive voltage for $N_{drag} = 1$ and $4 < N_{drive} < 5$.

The temperature dependence of the Coulomb drag signal was also studied in details. Within a single device, the temperature dependence was found to be drastically affected by the 1D subband occupancy of the wires, showing regimes where the Coulomb drag resistance is monotonic with temperature and a regime where an upturn is observed in the temperature dependence of the drag signal. In the high density negative Coulomb drag regime, the negative drag resistance vanishes at a temperature consistent with the system leaving the mesoscopic regime. Focusing on the true one-dimensional regime where a single 1D subband (or slightly less) is occupied in each wire, an upturn in the drag resistance is observed in three devices at a temperature in the vicinity of $T^* \sim 1.6$ K. This remarkable feature of the data is consistent with the predictions from the Luttinger liquid theory including forward scattering corrections arising from the non-linearity of the dispersion relation in 1D. Within this model, the upturn marks a crossover between a low-temperature regime where backscattering is the main contribution to Coulomb drag and a high temperature regime where forward scattering is the dominant contribution to Coulomb drag [2]. In the high temperature regime, the temperature dependence is found to be dominated by an exponential decay, $R_D \propto e^{-T_1/T}$, whose parameter T_1 provides a measure of the density imbalance between the wires. Our estimated T_1 values were found to be consistent with those extracted from the data. In the low temperature regime, the drag resistance was found to increase with decreasing temperature, as predicted by Luttinger liquid theory [2, 3]. However, the exact analytic shape of the low-temperature drag signal could not be determined.

While the temperature dependence of the Coulomb drag signal is in semi-quantitative agreement with a momentum-transfer Luttinger-liquid model with forward scattering corrections, the 1D subband occupancy dependence of the Coulomb drag signal, particularly the observation of a high density negative drag signal, is not fully understood. Therefore, it appears that the theoretical understanding of Coulomb drag remains incomplete. A theoretical model taking into account both the Luttinger liquid and the mesoscopic nature of quantum wires will likely have to be brought forth before a complete theoretical understanding of 1D Coulomb drag is reached.

8.2 Outlook

The phase-space of 1D-1D Coulomb drag study is *enormous*, and many aspects of this phase-space remain uncharted. In the short term, finalizing the characterization of the temperature dependence of one-dimensional Coulomb drag for all 1D subband occupancies is an obvious next step to supplement the experimental data reported in this thesis. Applying a magnetic field, either in a parallel or a perpendicular configuration with respect to the wires, is also an interesting prospect. This is motivated by previous studies in a lateral geometry where it was found that a magnetic field can increase the drag signal [4] and even give rise to the onset of a low-density negative drag regime [5]. In addition, Daniel Loss has conjectured theoretically that a nuclear spin, or helical, ordering [6] could arise in GaAs quantum wires. The resulting magnetism should provide a feedback to a LL. We speculate that the drag signal could be greatly modified in the presence of a magnetic field if this is the case as a strong magnetic field would likely destroy such hypothetical helical order.

While the experiments proposed above can all be performed with the devices used in this thesis, part of the Coulomb drag phase-space is only available if new devices are successfully fabricated. Indeed, it is possible to investigate the influence of the interwire separation if one fabricates vertically-coupled quantum wires in double quantum well heterostructures with a different barrier size. Having a wider barrier between both quantum wires might also allow us to study the low-density negative Coulomb drag regime without having quantum tunneling polluting the Coulomb drag data. Changing the length of the quantum wires, either symmetrically or asymmetrically, and offsetting the horizontal alignment of the wires might also affect the Coulomb drag signal, as previous studies in laterally coupled quantum wires have suggested [5, 7].

Of great interest would be to perform a thermal drag experiment, similar to the one described by Sothmann and co-workers [8]. Indeed, if the temperature dependence of the drag signal is well characterized, it would, in principle, be possible to deduce the temperature of the system from the drag signal itself. Then, using Joule heating to heat up the wires, and a drag measurement to measure the wires temperature, it would be possible to verify if a thermal drag signal is produced by heating a single wire. If confirmed, such an experiment could be key in the development of self-powered nanodevices and might alleviate the problem of heat removal in densely packed electronic circuits. Such a study would also allow us to investigate the violations of Wiedemann-Franz law that have been recently observed in one-dimensional systems [9].

Alternatively, measuring the Coulomb drag signal in an nuclear magnetic resonance setup (or resistively detected nuclear magnetic resonance), might allow one to change the state of the nuclear spins bath in which the quantum wires are located. Such an experiment could be used to verify the theory predicting the onset of a spontaneous helical nuclear spin helix, a novel quantum state of matter, in the Luttinger liquid regime [6].

The study of the one-dimensional Coulomb drag effect in vertically-coupled quantum wires presented in this thesis is not an end, but only a beginning. It is our hope that this platform will be used again experimentally in the future to elucidate the physics of one-dimensional systems.

References

[1] Hwang, E. H. and Das Sarma, S. *Phys. Rev. B* **77**, 235437 (2008).

[2] Pustilnik, M., Mishchenko, E. G., Glazman, L. I., and Andreev, A. V. *Phys. Rev. Lett.* **91**, 126805 (2003).

[3] Klesse, R. and Stern, A. *Phys. Rev. B* **62**, 16912 (2000).

[4] Debray, P., Zverev, V., Raichev, O., Klesse, R., Vasilopoulos, P., and Newrock, R. S. *J. Phys.: Condens. Matter* **13**, 3389 (2001).

[5] Yamamoto, M., Stopa, M., Tokura, Y., Hirayama, Y., and Tarucha, S. *Science* **313**, 204 (2006).

[6] Braunecker, B., Simon, P., and Loss, D. *Phys. Rev. B* **80**, 165119 (2009).

[7] Yamamoto, M., Takagi, H., Stopa, M., and Tarucha, S. *Phys. Rev. B* **85**, 041308(R) (2012).

[8] Sothmann, B., Sánchez, R., Jordan, A. N., and Büttiker, M. *Phys. Rev. B* **85**, 205301 (2012).

[9] Wakeham, N., Bangura, A. F., Xu, X., Mercure, J. F., Greenblatt, M., and Hussey, N. E. *Nat. Commun.* **2**, 396 (2011).

Appendices

A

Additional Fabrication Details

In this appendix, I describe the recipe details and the tool specifications that have been used to fabricate the Hall bars used in the shallow 2DEGs experiment and the vertically-integrated quantum wires used in the 1D Coulomb drag experiment. This appendix is a complement to the fabrication process described in chapter 3 and chapter 5 for the Hall bars and the vertically-integrated quantum wires, respectively.

Photolithography

During the fabrication process, photolithography is used to defined polymers mask on the devices. These masks are used to either chemically etch the device or to deposit metal on it. The photoresist used to defined such *in situ* masks is the AZ 5214-E photoresist. This polymer is spun at 5000 rpm for 30 seconds and then baked at 90°C for 90 seconds. Following this, U.V. light with a 400 nm wavelength is shone at an intensity of 200 mW/m^2 for 6.2 seconds while the device is placed under a physical mask, which protects the polymer from U.V. exposure in the appropriate sections. Following the U.V.

light exposition, the device is developed in a mixture of AK 400 : H_2O in a ratio 1 : 4 for ~ 30 seconds, stripping the polymer that had been exposed to U.V. light. Such a process is called positive photolithography and effectively creates a photoresist mask on the device. After the subsequent etching or the metal deposition is performed, the photoresist remaining on the device is stripped away through an acetone soak.

Phosphoric Etch

The phosphoric etch is performed using a combination of 85% phosphoric acid, hydrogen peroxide and water in a ratio H_3PO_4:H_2O_2:H_2O = 1:4:45. Such a chemical mixture etches through GaAs as well as AlGaAs at a rate of ~ 80 $\AA$ per second.

RTA

The tool used in this thesis to perform the rapid thermal annealing (RTA) is a Jipelec Jetfirst rapid thermal processor (RTP). The annealing is performed under a vacuum smaller than 0.05 mbar and the annealing chamber is purged with Argon. The temperature is measured by a pyrometer and temperature control is achieved through a standard PID loop. Here is a list of the steps occurring in a normal annealing cycle for the 420°C annealing used in this thesis.

- Evacuation the chamber to a pressure lower than 0.05 mbar.
- Purge of the chamber by flowing argon at a rate of 2000 cubic centimeters per minute (2000 sccm) for 30 seconds.
- Reduction of the argon flow to 100 sccm and setting the temperature

setpoint to 200°C.

- Temperature stabilization, typically taking 15 seconds.
- Temperature setpoint is set to 420°C.
- Temperature stabilization, typically taking 20 seconds.
- Anneal at 420° C for 60 seconds.
- Temperature setpoint is set to 20°C and argon flow is increased to 200 sccm.
- System is let to cool for 10 seconds.
- Argon flow in increased to 400 sccm and system is let to cool for 20 seconds.
- Argon flow in increased to 800 sccm and system is let to cool for 40 seconds.
- Argon flow in increased to 2000 sccm and system is let to cool for 60 seconds.
- Gradual venting of the system by shutting off the pumps and letting in an argon flow of 2000 sccm for 60 seconds.

E-Beam Metal Evaporation

The tool used in this thesis to perform the metal evaporation is a CVC metal evaporator, along with an IC/5 Inficon controller. The devices are mounted upside down at the top of the evaporation chamber while the metal cells are located at the bottom. Six cells can simultaneously be inserted inside the evaporator and multiple metal layers can therefore be deposited in a single run. The pressure inside the deposition chamber is lowered down to 9.0×10^{-7} mbar using a combination of roughing pumps and cryo-pumps. Once the pressure has reached this threshold and the suitable metal is in the opening of the chamber, the 9 keV electron beam is turned on and heats the metal cell. The power applied to the cell is controlled through a PID loop so that the appropriate deposition rate of the metal is achieved. The required power varies depending on the exact alignment of the electron beam, the size and type of the metal cell and the age of the filament, and therefore changes in-between metal depositions.

The metal deposition rate is measured *in situ* inside the deposition chamber. The deposition rate selected is 2 $\mathring{A}$ per second for metal layers thinner than 300 $\mathring{A}$ and 5 $\mathring{A}$ per second for layers thicker than 300 $\mathring{A}$. A manual shutter shielding the devices from the evaporated metal stream allows one to control the exact thickness of each metal layer. After the metal deposition is completed, the devices are cooled for 10 minutes before the evaporation chamber is vented and the devices are removed. Following this, the devices are soaked in acetone for at least 4 hours (and often overnight) to remove the photo-resist or PMMA polymer mask so that the metal stacks remain only on the appropriate sections of the device. Prior to the metal evaporation, the device is always cleaned using an oxygen (O_2) plasma (descum). The device is exposed to 50 watts of forward power for 5 minutes using using a PDS PDE-301 LFE tool. Following this descum process, the device is rinsed with a mild base (NH_3OH

: H_2O in a ratio 1 : 20) for 30 seconds.

E-Beam Lithography

The e-beam lithography tool used in this thesis is a LEO 440 SEM coupled with the Nanometer Pattern Generation System (NPGS) program, allowing one to do e-beam lithography with a commercial SEM. A Faraday cup, required to read the beam current, a gold standard to measure the astigmatism and a rapid beam blanker to carefully control the exposure (or dose) are mounted inside the SEM. The system is optimized before each e-beam lithography use and is warmed up for 30 minutes before usage.

Prior performing the lithography on an actual device, a dose test is performed if none had been performed in the previous week. The dose test consists of writing an array of single quantum wires using different exposures. Then, after a metal lift-off, the array is imaged under the SEM to determine which dose yielded the best pattern. All the e-beam lithography writing has been done on a PMMA 495-C4 polymer spun at 5000 rpm for 30 seconds and subsequently baked at 175°C for 15 minutes. Here is the procedure used in a standard e-beam lithography writing.

- Evacuation the chamber to a pressure lower than 1×10^{-6} torr.
- Turning on the electron beam at 40 keV and 2.5 μA, as well as sourcing 1760 mA through the filament and 95 pA through the probe and setting the working distance to 6 mm.
- Letting the filament stabilize for $\sim$ 30 minutes.
- Finding a sharp feature near the Faraday cup and focussing on it, adjust-

ing the distance between the beam and the stage to obtain the clearest image possible.

- Setting the SEM in fast scan mode, adjusting the aperture alignment so that the image does not wobble.
- Changing the gun shift, adjusting the beam shape so that it is circular when looking at it in the SEM deep mode.
- Zooming on the Faraday cup itself, adjusting the gun tilt so that the current going into the Faraday cup is maximal.
- While being still zoomed on the Faraday cup, adjusting the probe current value so that 10 pA are read through the ampmeter attached to the Faraday cup.
- Moving the field of view to the the gold standard, adjusting the stigmation on the SEM so that the gold spheres are as round as possible to the eye.
- Moving the field of view to the device, focussing on a feature far away from the section where the e-beam lithography will take place adjusting the distance between the beam and the device first and then slightly modifying the working distance so that the image is as clear as possible.
- Blanking the electron beam and remotely moving the beam to the approximate location of the writing field.
- Using NPGS, performing a fine alignment step using alignment marks deposited previously.

- Writing the pattern onto the device using NPGS and the optimal dose determined in the dose test.
- Repeating steps 4, 6-12 for every pattern to be written.
- Moving away from the device, turning off the filament and the electron beam.
- Venting the system.

Mechanical Lapping

The tool used in this thesis to carry out the mechanical lapping is a Buehler minimat grinder-polisher model 1600. To use this tool, the device is first mounted in the middle of a metal chuck using crystal bound heated at $\sim 130°\text{C}$. After the device is cooled, the chuck is encompassed inside a metal ring with a set screw that allows one to adjust the height of the metal ring. The height of this ring is adjusted so that the device is located between 575 and 625 μm above the top of the metal ring. This separation is measured using a Mitutoyo micrometer.

The height of this metal ring is of the utmost importance since it gets lapped a lot slower than the GaAs does, and hence ensure that the device surface is roughly leveled (within 30 μm) after the lapping process. A larger slope across the heterostruture surface would cause issues during the following chemical etching and it is thus essential that the heterostructure is lapped until the metal ring is the highest point of the setup. The lapping process occurs by rubbing the device against sandpaper in a semi-random motion to ensure mostly uniform lapping. The settings used on the minimat are a speed of 20 and a force of 1. The lapping is performed in water to collect the GaAs dust that is created during the process.

With those parameters, it takes about 45 minutes to lap $\sim$ 525 μm of material using a grade 240 sandpaper. Following this, the sandpaper is changed to a grade 600 and it takes about 10 minutes to lap the remaining $\sim$ 50 μm of material. Throughout the process, the amount of material lapped is periodically measured using the micrometer. After the lapping is completed, the device is dismounted from the metal chuck by dissolving the crystal bound in acetone.

Dielectric Layer Deposition

Two different dielectrics have been tested to isolate the upper and the lower gates in the vertically-coupled quantum wires structures: silicon-nitride (SiN) and aluminum oxide (Al_2O_3). SiN grown using chemical vapor deposition (CVD) and dry-etched was first tested, but it created severe charge accumulation and drifting inside the devices, rendering them inoperable. Therefore, SiN was ultimately replaced with Al_2O_3 deposited using atomic layer deposition (ALD) and wet-etched, as the charge accumulation and the drifting was minimal with this latter dielectric.

The Al_2O_3 layer is deposited at 200° C using a Picosum R150 tool. Before each ALD deposition, a test run of 100 cycles was performed to ensure that the chamber is clean and to verify the deposition rate of the system (roughly 1 $\AA$ per cycle). The deposition is performed under vacuum and two reactants are introduced in alternation in the deposition chamber. First, trimethylaluminium (TMA) is introduced in the chamber, followed by water (H_2O). These two chemicals react and create a uniform and smooth Al_2O_3 layer on any exposed surface in the deposition chamber. In addition to the device, a bare piece of silicon is also introduced inside the deposition chamber of the ALD tool and this bare silicon is used to measure the thickness of the Al_2O_3 layer deposited on the device.